NANO-SPECTROSCOPY AND NEAR-FIELD IMAGING OF LAYERED MATERIALS

by

ALIREZA FALI

(Under the Direction of Yohannes Abate)

ABSTRACT

Since the isolation of monolayer graphene, numerous other layered materials have been identified. In addition to providing a unique platform to discover exciting new physics, layered materials are promising for applications in flexible optoelectronics. In this thesis, we employ scattering-type scanning near-field optical microscopy (s-SNOM) and nano-Fourier transform infrared (FTIR) spectroscopy, in concert with analytical and numerical calculations, to study light-matter interaction of several layered materials including muscovite mica, phosphorous allotropes (violet and black phosphorus), hexagonal boron nitride (hBN), and transition metal dichalcogenides (MoS_2 & WS_2).

Infrared dielectric properties of muscovite mica, exfoliated on silicon and SiO_2 substrates is studied using near-field nano-FTIR spectroscopy. The spectra of mica show strong thickness and wavelength dependence, with a prominent broad peak centered around $\sim$1080 cm^{-1} assigned to Si−O. We reveal that the infrared dielectric permittivity of mica is anisotropic and experimentally measured nano-FTIR spectra agree well with analytical model calculations.

The chemical degradation of exfoliated violet phosphorus (VP) in comparison to black phosphorus (BP) is studied under ambient conditions using Nano-FTIR and nanoscale imaging. We identify oxidized phosphorus species that result from chemical reaction processes on the

surfaces of these phosphorus allotropes. We have found that VP exhibits a noticeably different and slower degradation process when compared to BP.

Two dimensional (2D) in-plane MoS_2–WS_2 heterostructures exhibiting nanoscale alloyed interfaces are investigated using elastic and inelastic scattering near-field nanoscopy. The 2D alloyed regions exhibit thermal and photodegradation stability providing protection against oxidation. Coupled with surface and interface strain, 2D alloy regions create stable localized potential wells that concentrate excitonic species via a charge carrier funneling effect.

In this thesis we demonstrate a reconfigurable hyperbolic metasurface comprised of a heterostructure of isotopically enriched hexagonal boron nitride (hBN) in direct contact with the phase-change material (PCM) single-crystal vanadium dioxide (VO_2). Metallic and dielectric domains in VO_2 provide spatially localized changes in the local dielectric environment, enabling launching, reflection, and transmission of hyperbolic phonon polaritons (HPhPs) at the PCM domain boundaries, and tuning the wavelength of HPhPs propagating in hBN. This system supports in-plane HPhP refraction, thus providing a prototype for a class of planar refractive optics. This approach offers reconfigurable control of in-plane HPhP propagation. Furthermore, the thesis investigates HPhP characteristics as a function of the substrate dielectric function by employing s-SNOM and nano-FTIR, in concert with analytical and numerical calculations.

INDEX WORDS: Polaritons, Layered materials, Nanophotonics, Boron nitride, Infrared imaging, Hyperbolic materials, Mica, 2D materials, nano-FTIR, Violet phosphorus, Black phosphorus, Degradation, Heterostructures, 2D alloys, Exciton, Nanoimaging, Photodegradation

NANO-SPECTROSCOPY AND NEAR-FIELD IMAGING OF LAYERED MATERIALS

by

ALIREZA FALI

B.S., Malek Ashtar University of Technology, 2009

M.S., University of Guilan, 2012

A Dissertation Submitted to the Graduate Faculty of The University of Georgia in Partial Fulfillment of the Requirements for the Degree

DOCTOR OF PHILOSOPHY

ATHENS, GEORGIA

2022

NANO-SPECTROSCOPY AND NEAR-FIELD IMAGING OF LAYERED MATERIALS

by

ALIREZA FALI

Major Professor:	Yohannes Abate
Committee:	Yiping Zhao
	Tina Salguero

Electronic Version Approved:

Ron Walcott
Vice Provost for Graduate Education and Dean of the Graduate School
The University of Georgia
May 2022

DEDICATION

I dedicate this dissertation research to my wife, Neda, for her support throughout the years. She has believed in me and encouraged me in my Ph.D. program.

I also dedicate this to my parents, who have tolerated my absence for several years to accomplish this Ph.D.

Moreover, I dedicate to my brothers, Amir Mahmood and Hamidreza, who took care of my parents in my absence.

Finally, I would like to dedicate this work to those whose dreams do not turn to reality, not due to the lack of dedication on their part, but merely as a result of their socioeconomic status.

ACKNOWLEDGEMENTS

I am extremely grateful to my major professor Yohannes Abate for the incredible amount of time he has spent mentoring me during all my graduate work. He has taught me so much about being a researcher and enjoying science.

I am also grateful to my committee members: Yiping Zhao, and Tina T Salguero for their continued guidance and help to improve and correct this dissertation.

I want to thank Dr. Sampath Gamage for training me and for the excellent collaborative work we had. I also thank my colleague Neda for several years of productive collaboration.

My dissertation research would not have been possible without their participants. I am grateful that they were willing to share their time and experiences.

Finally, yet importantly, I would like to acknowledge funding agencies, Air Force Office for Scientific Research (AFOSR) and National Science Foundation (NSF), for financially supporting this research project.

TABLE of Contents

LIST OF FIGURES

Figure 4.17 Comparison of numerical and analytical solutions as a function of frequency, for different hBN thicknesses, suspended (top left) and on Si (top right). The thickness-normalized wavevector kd is plotted to suppress the influence of hBN thickness. Blue (red) triangles (circles) are numerical solutions at 20nm (120nm). The analytical solutions (solid lines) diverge from the numerical solutions in thick flakes at low frequencies. (c) Influence of substrate dielectric function upon high-order HPhP modes of hBN at 1510 cm^{-1}, for dielectric (metallic) substrates, with the loss tangent fixed at 0.01 (0.3). c) $k \cdot d$ was plotted versus $Re(\varepsilon_s)$, and gray stars are experimental data in Ref. [101] , while open boxes are numerical solutions for 120 nm thick hBN. (d) FOM of the first three orders of HPhPs in this same thickness flake of hBN as a function of the $Re(\varepsilon_s)$. 69

Figure 4.18 imulations of spatial separation of the HPhP modes and applications of HPhPs through dielectric enviornment control. a) A schematic diagram of the proposed HPhP spatial separator device, with the corresponding b) simulated electric field (E_z) for HPhP modes separated due to refraction resulting from HPhP transmission over a Si-air interface aligned at 45º with respect to the propagation direction. To eliminate complexities in the image due to back reflections, a notional highly-absorbing hBN border with a 20-fold increase in the damping constant was added. The corresponding refraction of the $l = 0$(orange) and $l = 1$ order (green) HPhPs are provided. c) Schematic diagram of a proposed hBN HPhP-based SEIRA or index-sensing resonant device induced due to large index contrast in spatial regions underneath the hBN flake as designated. The corresponding reflection spectra for this resonant structure fabricated from a hBN flake over an empty d) or Si-filled e) resonant chamber (e.g. hole). The calculated resonance spectra are highly sensitive to the presence and thickness of an analyte layer on top of the hBN surface; suspended hBN films have the highest degree of sensitivity.The spectra provided for both cases in d) and e) as a function of analyte layer thickness are labeled. FOM of HPhPs in hBN on (f) dielectric

CHAPTER 1
1. Introduction

Since the first isolation of graphene, layerd materials attracted attention due to their unique physical properties. A wide variety of two dimensional materials been synthesized which have applications in diverse areas of technology such as optoelectronics, biomedicine, and energy storage. Layerd materials are highly anisotropic bondin materials when atoms in two dimensional sheets are strongly bonded but layers are connected by weakly bonded Van der Waals (vdW) force to the adjacent ones. Regarding to the weak bounds between sheets these materials are easity to exfoliate in order to produce one or few layers of them.

As the physical dimensions of the materials decrease to nanometer-scale, understanding the physical properties at the nanoscale is crucial. This importance is because the properties of a material in the nanoscale are different from those of their bulk counterparts. Furthermore, dipole-type polaritonic excitation have been observed in layered materials. Polaritons in layered materials are effective way to convert long wavelengths of light to few hundrends of nanometer lenght waves. Ploaritons opening up opportunities in bio-sensing, optoelectronics and othe mid-infrared applications.

In this thesis, Interaction of nano-focused light via a metalized tip with layered materials have been extensively studied. The interaction of light with sample provides the local dielectric properties of the sample. The nanoscale imaging can also provide the information about dispersion

of polaritons. We have used nanoscale imaging and spectroscopy methods to study these effects by breaking the tyrnanny of the optical diffraction limit.

Imaging of nanoscale features has been a challenge in optical microscopy for a long time. In the 19th century, Abbe introduced a fundamental limit on the maximum resolution of the optical image, which is known as the diffraction limit [1]. The diffraction limit made generations of scientists believe that it is impossible to study the nanoparticles and resolve subwavelength structures [2]. Therefore, breaking the diffraction limit was necessary to reach a high resolution to study the nano particles. Various microscopy methods such as Scanning Electron Microscopy (SEM), Scanning Tunneling Microscopy (STM), and Transmission Electron Microscopy (TEM), have been developed for this reason. However, these methods can not provide optical properties of materials such as absorption and photoluminescence. On the other hand, some conventional optical characterization techniques such as FTIR, Photoluminescence, and Raman Spectroscopy can provide the optical information of the sample. However, the resolution of those conventional spectroscopy methods is diffraction limited.

In the studies presented in this thesis, an external focused laser beam is combined with the Atomic Force Microscope (AFM) based nanoscopy to record the interaction of light with materials at the nanoscale. The scattered light from the interaction of the AFM tip and the laser is directed to detectors. This interaction of light, sample, and tip can simultaneously provide optical properties and the topographic information of the sample. The resolution of this method is independent of the wavelength of the incoming light, and it only depends on the apex size of the probing tip. This AFM-based nano-spectroscopy methods have been applied to study layered materials' optical and

electronic properties as well as investigate dispersion of polaritons in hexagonal Boron Nitride (hBN) on different substrates.

1.1 Introduction to Nano-optics

In classical optical microscopy, the image is formed with the help of lenses and objectives, and usually, an electromagnetic wave in the visible region is applied to create an image. The resolution of the image depends on the optics and the wavelength of the incident light. When the size of a particle becomes smaller than the wavelength of the incident light, the image starts to get blurred. The image of a tiny point source produced by optical microscopy will not be a point. It is a bright central region with a series of concentric rings around it, known as the Airy pattern [3]. This limitation on the spatial resolution is introduced to the imaging system by the diffraction of light.

Abbe derived the equations for the fundamental limitation in optical microscopy in 1873 [1]. The effect that known as Abbes' diffraction limit or diffraction limit states that light with wavelength λ, traveling in a medium with refractive index n and converging to a spot with the half collection angle of θ will have a resolvable distance of

$$d = \frac{\lambda}{2nsin\theta} = \frac{\lambda}{2NA} \tag{1.1}$$

The term $nsin\theta$ is known as numerical aperture NA, which means with the shortest wavelength of the visible light (400nm), the Abbe limit is roughly around $d = \frac{\lambda}{2} = 200\,nm$. This resolvable distance is suitable for some samples like biological cells; however, it is problematic with smaller particles, viruses, or proteins. The shorter wavelength can help achieve better resolution, but it can add limitations such as high energy beams and expensive experimental setup. In general, changing

to a shorter wavelength will add other limitations, and it is not a practical solution specifically for particles smaller than 50 nm. For this reason, various microscopy and nanoscopy methods have been developed during the past years. To break this limitation, different techniques and devices such as lasers and detectors needed to be improved, and efforts are still ongoing for further improvement of the resolution [2].

1.2 Nano-scale material characterization techniques based on Scanning probe Microscopy

Various nano-scale characterization methods such as SEM, Fluorescence microscopy, and Scanning probe microscopy have been developed during the past few decades to overcome the diffraction limit. These methods were developed to explore different sample properties, such as shape, size, and optical properties. Depending on the structure and aim of the study, scientists decide which methods are the best for their material.

Scanning probe microscopy (SPM) is a family of microscopy techniques that form images of nanoscale surfaces and structures using a physical probe moving on the surface. These methods break the diffraction limit using different probe interactions with the sample surface, such as atomic force, quantum tunneling, and near-field.

The Scanning Tunneling Microscope (STM), invented in 1981, was the first member of the SPM family [4]. STM is based on quantum tunneling, that an extremely thin probe is brought very close to the surface of a sample kept in the vacuum. A bias voltage applied between sample and probe allows electrons to tunnel through the vacuum. An image can be formed from the resulting tunneling current as a function of tip position.

The branch of scanning probe microscopy techniques is not limited to STM; it includes a long list such as Atomic Force Microscopy (AFM), Kelvin Probe Force Microscopy (KPFM), and sSNOM. The rest of this chapter focuses on SMP techniques related to the apertureless scattering-type Scanning Near-field Optical Microscopy (sSNOM).

Atomic Force Microscopy

AFM is a nano-characterization method invented more than 30 years ago by IBM scientists [5]. Gerd Bining, who won the Noble Prize in Physics in 1986 for developing the STM, was the first person who developed AFM [5]. AFM breaks the diffraction limit and provides resolution in a few nanometers that only depends on the tip's apex. It produces a topography image of the sample by raster scan. AFM's main parts are a cantilever connected to the probe and a deflection laser reflecting from the cantilever to a photodetector, as shown in figure 1.1. The position of the laser spot that reflects to the photodetector provides a well-correlated measurement of the movement of the probe tip relative to the sample surface, which produces topography information of the surface of the sample. For the highest degree of precision of the probe's movements on the sample, the probe is moved over the sample by a scanner that uses a piezoelectric. AFM works in the contact mode and tapping mode. The tapping mode AFM is preferred for the SNOM method since tapping the tip can provide a demodulated near-field signal to the detector. Demodulation of the signal will be explained in more detail in chapter 2.

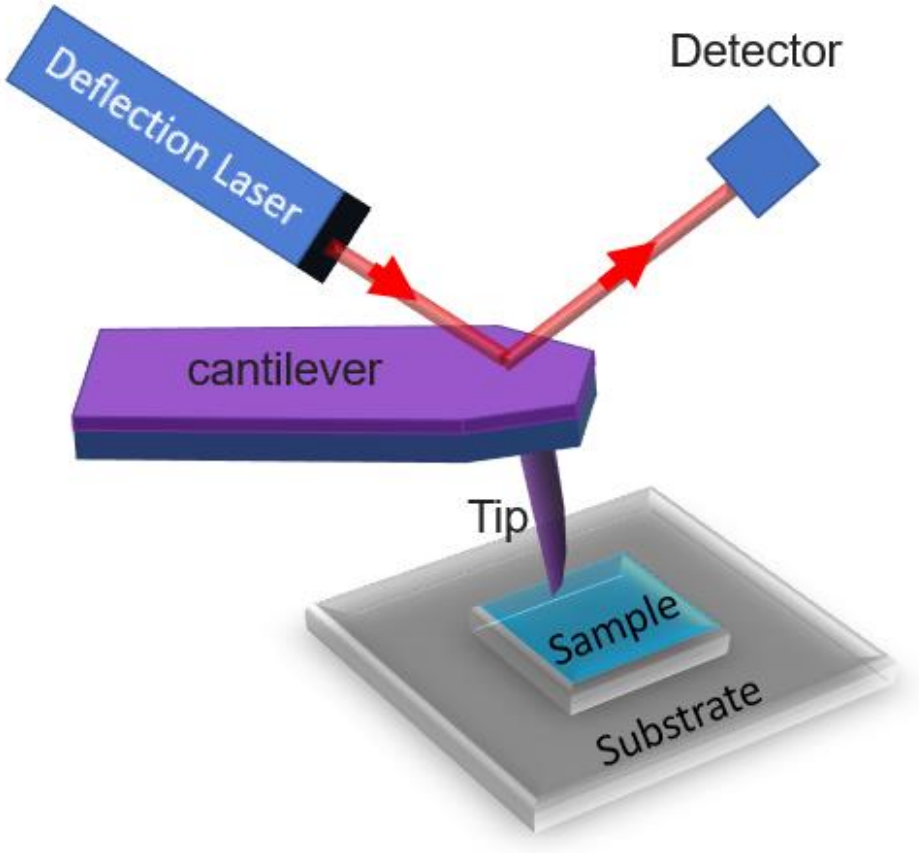

Figure 1.1 Schematic of Atomic Force Microscope

Aperture SNOM

Light can pass through an extremely thin aperture to form an image of the surface on a subwavelength scale. E.H. Synge first proposed the idea to use an aperture to break the diffraction limit in 1928 [6]. At that time, he predicted a resolution of 10 nm for his proposed method. However, it took several years until, in 1972, E.A. Ash experimentally demonstrated a resolution of $\lambda/60$ in a scanning near-field microscopy by use of microwaves radiation[7]. Finally, A. Lewis, in 1984, invented the aperture probing microscope, which was able to a 50 nm spatial resolution by using a 30 nm diameter metal aperture[8]. In aperture SNOM, a probe with a tiny aperture

moves close to the sample's surface that can be used either as the excitation path, detection path, or both. The resolution in this method only depends on the diameter of the aperture. A feedback mechanism similar to AFM can control the probe-sample distance to guarantee to collect the near-field data. The aperture probes usually are made of a metal-coated fiber with a hole at the apex. However, aperture SNOM is limited for longer wavelengths due to the cutoff problem in fibers. According to the cutoff equation in fibers, the core radius directly relates to the fiber's cutoff wavelength [9]. It means cutoff occurs in a thin core of a fiber, which exponentially decreases the transition for longer wavelengths[10]. In order to overcome to these limitations, aperturerless SNOM is one of the most effective ways. It will be introduced in details in chapter 2.

CHAPTER 2
2. Experimental methods

In this chapter, experimental methods that have been used in this thesis will be presented. The experimental setup is based on the tapping mode AFM. The metallic AFM tip is illuminated by a focused laser beam to image layered materials at the nanoscale in different wavelengths. The elastically or inelastically scattered radiation from the tip-sample and laser interaction propagates simultaneously and provides information about the sample's optical properties. The elastically scattered radiation produces the s-SNOM image or Nana-FTIR data of the sample. On the other hand, inelastic radiation can provide Photoluminescence and Raman Shift information from the sample.

2.1 Elastic scattering based characterization; SNOM and Nano-FTIR

AFM is a powerful device enabling the recording of the topography of a surface at the nanoscale. However, it cannot provide the information of the dielectric properties of the surface material. Aperture SNOM is capable of providing this information. However, its resolution is severely limited by the aperture size. To overcome the mentioned limitations, an apertureless techniques was developed in the 1990s based on the AFM enabling to record both topographic and dielectric information of the surface[11-15]. This technique is known as scattering-type Near-field Scanning Microscopy (s-SNOM).

2.1.1 Scattering Type Scanning Near-Field Optical Microscopy (s-SNOM)

Manipulating photons and enhancing light-matter interactions in the nanoscale are two reasons Scattering-Type Scanning Near-Field Optical Microscopy (s-SNOM) raised tremendous

attention. The s-SNOM is an optical nano-characterization method based on the tapping mode AFM. A laser beam is focused on the metallic AFM tip by a parabolic mirror and reflects to the detector, as shown in figure 2.1. Focus is done in the setup by using a parabolic mirror. Due to the presence of the AFM probe, SNOM provides resolution independent from the wavelength of the incident light and only determined by the apex of the tip. The spatial resolution of SNOM is 10 nm [16]. For the near-field experiment, sharp tips with metal coats are used. In all the experimental data reported in this work, Platinium-coated tips were used.

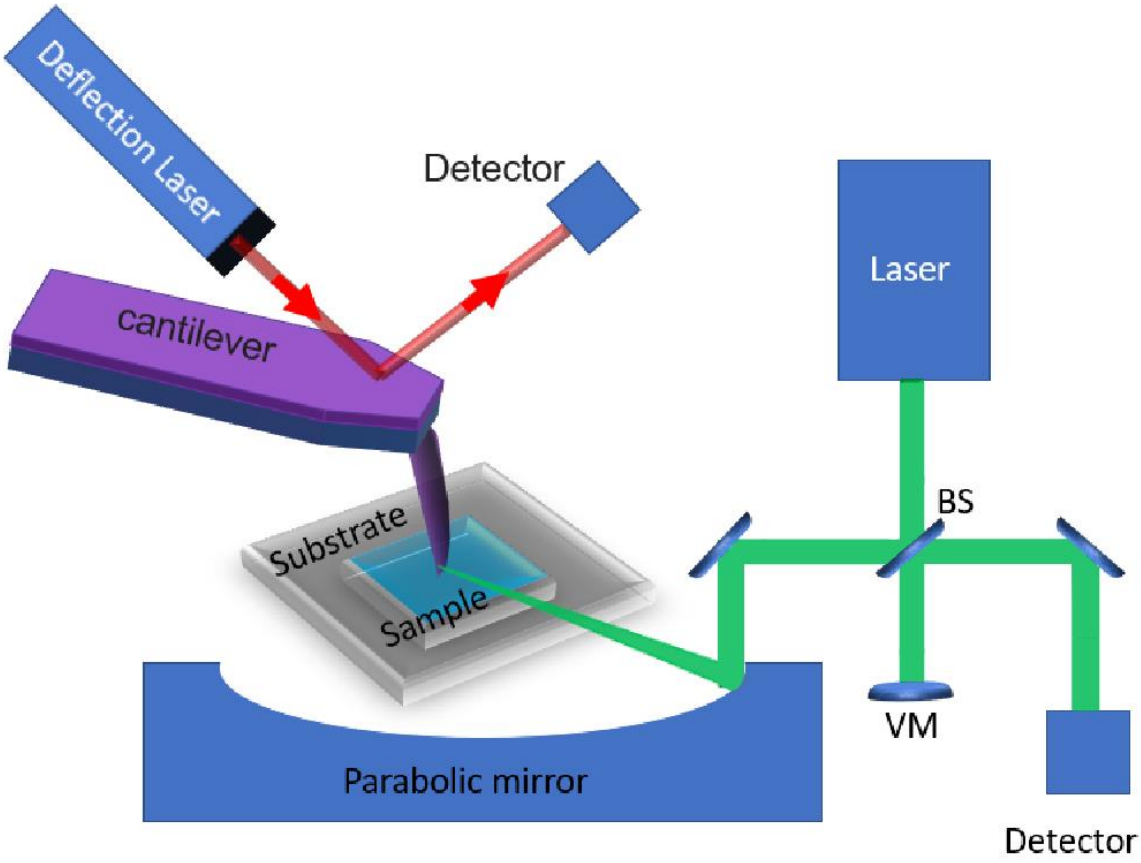

Figure 2.1 Schematic of the s-SNOM experimental setup.

The raster scanning of the sample by the AFM probe provides the topography image as well as optical near-field amplitude and phases simultaneously. The metallic tip works as an

antenna that converts emission to a highly localized and enhances near-field at the tip's apex. [17-21]. Depending to the dielectric properties of the sample, the tip scattered radiation is modified in both amplitude and phase. However, the emitted signal from the interaction between the concentrated beam with the sample at the tip is one portion of the signal captured by the detector. The laser beam can also reflect from the sample or the shank of the tip. These two scattered beams are far-field and diffraction-limited. A tapping-mode AFM is being used to filter out these emissions and only analyze the scattered near-field beam. AFM probe oscillates with a frequency of about $250kHz$. As presented in chapter 3, the near-field scattered signal depends on the distance between tip and sample. The tip oscillates with an amplitude of $50-100\,nm$. The evanescent near-field signal has strong dependence on the distance between the tip and the sample, and by increasing the space, the near-field signal rapidly vanishes. The tapping mechanism can modulate the near-field signal scattered from the sample. Specifically, at the higher harmonics of tip frequency ($n > 2,3,4$), the near-field scattered signal is strong enough to surpass the near-field emission [22, 23]. Another approach to improving optical contrast is using an interferometer [24, 25]. This setup, known as Pseudo-heterodyne, also enables the extraction of phase information from the sample.

2.1.2 Background subtraction and Psedu-heterodyne detection

The emission from the sample and tip interaction is one portion of the radiation going to the detector. There is also background radiation of reflection of laser from the tip and sample:

$$E_{sca} = E_{nf} + E_{bg} \tag{2-1}$$

The near-field signal is highly distance dependence and is strongly non-linear with tip-sample distance. On the other hand, background scattered emission is only depending on the wavelength

of the incident laser. So, the background scattering is good to be considered to change linear with tip oscillations. This linear change is mainly restricted to the oscillation frequency of the tip. By demodulating the detected signal at higher harmonics of tip oscillation, the background emission portion is negligible compared to the near-field contribution [26]. The measured electric signal at the detector is proportional to the intensity of the light at the detector:

$$I_{detector} \propto I_{sca} \propto |E_{sca}|^2 = \left|E_{nf} + E_{bg}\right|^2 = (E_{nf} + E_{bg})(E_{nf} + E_{bg})^* \quad (2\text{-}2)$$

As shown in equation (2-2), there always is a contribution from the background even at higher harmonics [27]. The solution to completely suppress the background is to use a Michelson interferometer, demodulation of reference phase [27]. This detection method is called pseudo-heterodyne detection, and it adds phase detection of the backscattered signal as well.

As shown in the schematic in figure 2.1, half of the laser beam is separated by the beam splitter and sent to a vibrating reference mirror. This emission is combined again with backscattered light and is directed to the detector. The measured electric signal at the detector in equation (2-2) then will be modified as:

$$I_{det} \propto I_{sca} \propto \left|E_{sca} + E_{ref}\right|^2 = (E_{nf} + E_{bg} + E_{ref})(E_{nf} + E_{bg} + E_{ref})^* \quad (2\text{-}3)$$

Where E_{ref} is the electric field of reference beam. The vibrating mirror oscillates at a frequency ($M{\sim}300Hz$) which is much lower than the tip frequency($\Omega{\sim}300kHz$). The sinusoidal vibration of the reference mirror yields a phase modulation of the reference beam. The presence of the interferometer makes sidebands around the tip oscillation frequency Ω and its higher harmonics $n\Omega$ (n is the number of harmonic) at spectral positions $n\Omega \pm \mathrm{mM}$ (m is the number of sideband) [27]. The demodulation process can be described mathematically by Fourier analysis of the

detected signal. The Fourier coefficient of the backscattered signal and background can be written as:

$$\sigma_{nf,n} = S_{nf,n} e^{i\varphi_{nf,n}} \tag{2-4}$$

$$\sigma_{bg,n} = S_{bg,n} e^{i\varphi_{bg,n}} \tag{2-5}$$

In equation (2-4), S_{nf} is the near-field amplitude and φ_{nf} is the near-field phase. Similarly in equation (2-5), S_{bg} and φ_{bg} are the near-field amplitude and phase respectively for the background scattering. The nth Fourier coefficient of the tip-scattered signal can be derived from the first and second sidebands ($U_{n,1}$ and $U_{n,2}$ respectively) and can be obtained from[27]:

$$\sigma_{sca,n} = \sigma_{nf,n} + \sigma_{bg,n} = 2.16k(U_{n,2} + iU_{n,1}) \tag{2-6}$$

$U_{n,1}$ and $U_{n,2}$ are the first and second sideband respectively. Where k is the proportionality constant. Background in equation (2-6) can be effectively suppressed by choosing higher harmonics. Consequently, for higher harmonics, we can neglect background $\sigma_{sca,n} \sim \sigma_{nf,n}$ and obtain near-field amplitude (S_n) and phase(φ_n) [27]:

$$S_n = 2.16k\sqrt{U_{n,1}^2 + U_{n,2}^2} \tag{2-7}$$

$$\varphi_n = \arctan\left(2.16k\frac{U_{n,2}}{U_{n,1}}\right) \tag{2-8}$$

2.1.3 Nano- FTIR

Fourier Transform Infrared (FTIR) spectroscopy is a method that can provide information based on molecules vibration. A sample exposed to IR emission will selectively absorb at specific wavelengths. The absorbed wavelengths are related to the vibrational states of molecules and reveal the composition of materials. The term “Fourier Transform” is because this method needs

a Fourier transform to convert the measured results to the spectrum. However, according to Abey's diffraction limit, this method is insufficient for scanning small particles and viruses[28].

Nano-FTIR is a spectroscopy method to overcome the diffraction limit. This setup is also AFM-based, similar to the SNOM. Like the SNOM, the probe helps break the diffraction limit and extract the dielectric properties at the resolution of the tip. However, the tip is eliminated by a broadband light source. For the experiments reported in this work, the light source covered $5 - 15\ \mu m$ spectral range. There is a moving mirror replaced with the vibrating mirror in figure 2.1. The moving mirror, in combination with higher harmonic demodulation (see section 2.1.2 for harmonic demodulation) can provide the near-field interferogram. The Fourier transformation of the interferogram can provide near-field amplitude and phase of the measured spot of the sample. This method can be used for a wide range of samples characterization, such as layered materials and viruses [29-31].

2.2 Inelastic scattering based characterization; Tip-enhanced photoluminescence (TEPL) and Tip-enhanced Raman Spectroscopy (TERS)

The previous section was focused on the elastically scattered light when the detection has been done at the same frequency of the incident beam. However, depending on the materials, photons can be emitted at frequencies shifted from the original incident beam. This section focuses on enhancing the inelastically scattered photons from the tip and sample interaction.

2.2.1 Raman Spectroscopy

As light interacts with materials, it can be scattered with the same frequency (elastic scattering), also known as Rayleigh scattering, or with a shift in the frequency (inelastically scattering) known as Raman scattering. Raman scattering was first predicted in 1923 by A. Smekal

[34]. It was first experimentally observed by C.V. Raman in 1928 [32]. Because of this demonstration, the inelastic scattering of light from the material is known as the Raman effect.

Raman shifts correspond to molecules' vibrational modes (and sometimes rotational states). According to the Raman shift equation, it has small shifts from the excitation wavelength. However, The wavelength of the excitation laser is significant in the strength of the peak. Raman scattering strength is proportional to the fourth power of excitation frequency. Consequently, a shorter excitation wavelength can give stronger Raman.

Raman effects occur when an incoming photon from a laser source interacts with the molecular vibrational mode of the material. This interaction excites an electron to an intermediate state (virtual state) the electron immediately falls down to the ground state. There are three different scenarios as shown in figure 2.2, that how electron light can be re-emitted. The electron can fall down to the same energy state in which there is no energy change between the incident photon and emitted one, which is called Rayleigh scattering. However, as shown in figure 2.2, electrons also can have lower or higher energy that the excitation photon, which are called Stokes and Anti-Stokes scattering, respectively.

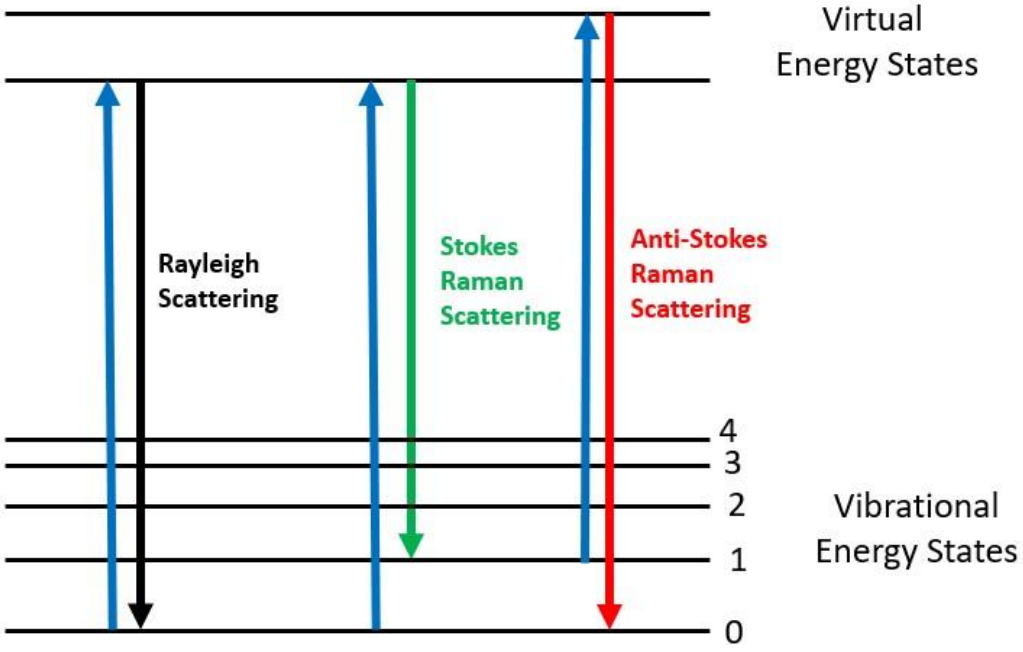

Figure 2.2 Energy level diagram for Rayleigh scattering, Stock Raman scattering, and Anti-Stock Raman scattering.

Both Raman Spectroscopy and FTIR provide information from vibrational states of molecules, but they have fundamental differences. Raman Spectroscopy relies on the polarizability of a molecule, while FTIR relies on the dipole momentum of a molecule. Molecules with functional groups with strong dipoles display strong peaks in the IR. In contrast, functional groups that readily show a change in polarizability display strong peaks in Raman.

2.2.2 Photoluminescence

When electromagnetic radiation hits a semiconductor material, it can interact with it. An electron of the material can absorb the photon's energy to excite and transfer to a higher energy level where the energy difference is equal to or less than the photon energy. The energy difference between Valence Band (VB) and Conducting Band (CB) in semiconductors is known as bandgap. If the incident photon's energy is greater than the bandgap, it can excite the electron from VB to

CB. The excited electron will return to the VB and generate radiation (recombination) called photoluminescence, which includes information about the bandgap of materials. It is a two-step photon absorption-emission process involving electronic states. Figure 2.3 shows the emission of Photoluminescence. The energy of the emitted photon can be expressed in terms of the energy gap between the conduction band energy (E_C) and the valence band energy (E_v).

$$h\nu = E_C - E_V \tag{2-9}$$

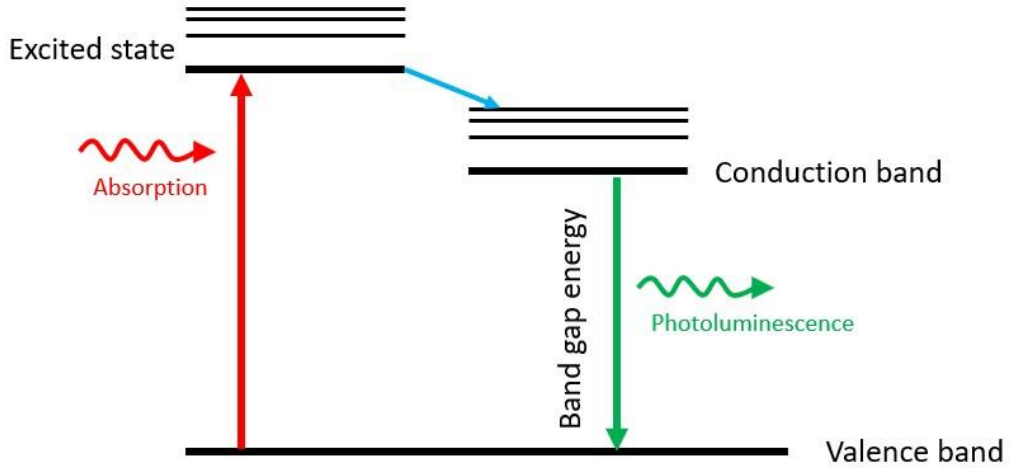

Figure 2.3 Excitation process and emission of Photoluminescence.

2.2.3 Tip Enhanced photoluminescence (TEPL) and Tip-enhanced Raman Spectroscopy (TERS)

Tip Enhanced Photoluminescence (TEPL) and Tip Enhanced Raman Spectroscopy (TERS) are two spectroscopy methods that use a metallic tip to enhance PL and Raman spectroscopy sensitivity. Gold and Silver probes are widely used for TERS experiments. However, reposts showing regular Pt tips have comparable performance [33]. Similar to the SNOM, approaching a metallic probe to the sample's surface can create a strong field near the apex of the tip [34, 35].

This strong field can enhance the PL emission from the sample [34, 36]. Tip enhancement is attributed to three different effects [34]. One is the coupled light to the metallic tip, which is known as Surface Plasmon Resonance (LSR) [36]. The second mechanism that enhances the emission is known as the lightning rod effect, which comes from concentrating the electromagnetic field at the apex of the tip[33, 37]. The third mechanism that can enhance the presence of the tip is near-field coupling between the tip and the metallic sample. Enhancement depends on different factors such as metallicity of sample, shape, and properties of the tip can vary for different samples[38]. It has been estimated to be as high as five orders of magnitude for WSe_2 [39]. Tip enhancement generally depends on the geometry of the tip, materials of the tip, and the dielectric function of the sample. Tip enhancement can be explained by the dipole model [40].

$$\kappa = 1 + \frac{2\alpha[\frac{1}{a^3}+\frac{\beta}{(2d+a)^3}]}{1-[\frac{\alpha\beta}{4(d+a)^3}]} \tag{2-10}$$

Where κ is the effective polarizability, a is the tip radius, and d is the tip-sample distance. α is the dipole polarizability, and β is the coefficient associated with the dipole.

$$\alpha_0 = 4\pi\frac{(\varepsilon_t-1)}{(\varepsilon_t+2)}a^3 \tag{2-11}$$

$$\beta = \frac{\varepsilon_s-1}{\varepsilon_s+1} \tag{2-12}$$

Where ε_t and ε_s are dielectric functions of tip and sample, respectively. More detailed equations for tip enhancement are provided in chapter 3.

The tip-enhancement mechanism in TEPL and TERS is generally similar to SNOM. However, the background subtraction is different which is due to the presence of the spectrometer. In such a case, it is impossible to have a demodulation mechanism to remove background emissions to have spectroscopic contrast, another method has been applied to remove background

emissions which is known as the tip-in-tip-out experiment [41]. In such a case, the near-field enhancement of the tip I_{nf}, can explained as:

$$I_{nf} = I_{tip-in} - I_{tip-out} \tag{2-13}$$

where in this equation I_{tip-in} and $I_{tip-out}$ are PL (or Raman shift) intensity when the tip is in contact to the sample and when tip is retracted from the sample, respectively.

In the experimental setup we used for this work, a semiconductor sample is excited by a green laser (532 nm) [42]. In order to get the best alignment of the laser to the tip, a standard near-field retraction curve is performed by detecting the backscattered near-field when the signal is maximum at small tip-sample distances and decreases rapidly as the tip is pulled away from the sample due to effective signal demodulation. Then the PL pr Raman shift radiation from the sample is collected by the parabolic mirror and sent back to the spectrometer. There is a 532 nm long-pass edge filter to remove the green laser. The schematic of the setup is shown in figure 2.4.

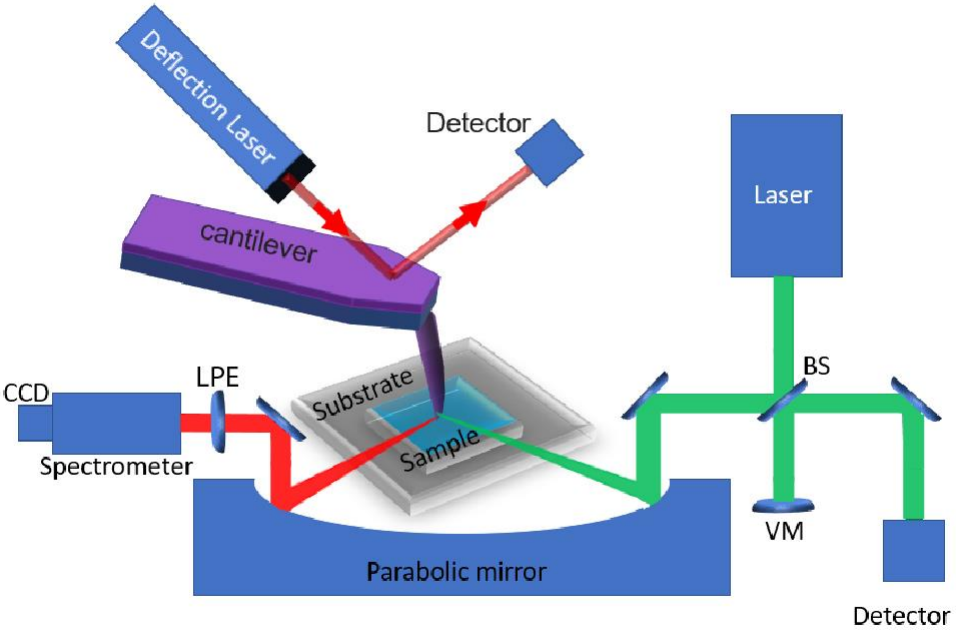

Figure 2.4 Schematics of integrated s-SNOM/TEPL/TERS experimental setup (LPE = Long-pass edge filter, BS = beam splitter, VM = vibrating mirror)

To obtain normalized TEPL spectra, the tip is retracted from the sample flake to record a reference spectrum. Then, a spectrum is taken on the sample surface while the tip is engaged. A normalized spectrum is achieved by subtracting the reference spectra from the spectra taken on the sample. Tip-sample distance dependence of TEPL/TERS signal of the ML heterostructure MoS_2-WS_2 is always checked before any measurement [42].

CHAPTER 3
3. Theoretical methods description

In this chapter theory and calculation of different models been used in this thesis will be explained. The theoretical calculations have been used for different purposes. In the first part, the calculation of the near-field backscattered emissions from tip and sample interactions will be presented. Then, the calculation of Phonon polaritons dispersion will be presented.

3.1 Theoretical basics of s-SNOM

Different theoretical models have been developed to calculate the elastically backscattered emission from tip, light, and sample near-field interaction [17, 28, 29, 43-47]. The difference in the models is mainly the way they approximate the tip and its interaction with the sample. Models try to relate the scattered light to the incident electromagnetic field by considering the dielectric properties of the sample. The scattered light from the sample is a function of the incident electromagnetic field:

$$E_{sca} = \sigma_{nf} E_{inc} \tag{3-1}$$

Which σ_{nf} is the near-field scattered coefficient, which depends on the refractive index of the sample and polarizability of the tip[46].

$$\sigma_{nf} = \alpha_{eff}(1 + r_p)^2 \tag{3-2}$$

Where α_{eff} is the effective polarizability of the tip and approximation to calculate it, depends on the model and r_p is the reflection coefficient.

The Dipole Model is the most well-known model for describing the near-field interaction of tip and sample. In this model, the tip is considered as a dipole interacting with the sample. The near-field backscattered emission depends on the dielectric function of the sample.

3.1.1 Point dipole model

The Point-Dipole-Model (PDM) is a conventional model that calculates the near-field interaction between light and materials by considering the tip as a spherical dipole with the radius of a ($a \ll \lambda$). As shown in figure 3.1.a., this model calculates back scattered light by approximating the tip as a small dipole that induces another dipole inside the material [22].

In this model, the effective polarizability of the tip is approximated as [46]:

$$\alpha_{eff} = \alpha_0[1 - f(H)\beta(\varepsilon)]^{-1} \tag{3-3}$$

As shown in figure 3.1, H is the tip-sample distance. β is the quasi-static reflection coefficient which is a function of the dielectric function of the sample (ε_s):

$$\beta = \frac{\varepsilon_s - 1}{\varepsilon_s + 1} \tag{3-4}$$

Where $\alpha_0$is the polarizability:

$$\alpha_0 = 4\pi \frac{(\varepsilon_t - 1)}{(\varepsilon_t + 2)} {R_t}^3 \tag{3-5}$$

Where ε_t and $R_t$are permittivity of the tip and radius of the tip, respectively. $f(H)$ in equation (3-3) defined as [46]:

$$f(H) = \alpha_0/(16\pi(R_t + H)^3) \tag{3-6}$$

3.1.2 Finite dipole model:

In Finite Dipole Model (FDM) as shown in figure 3.1. b, the tip is approximated as a conductive spheroid with a length of $2L$, which gives a more realistic approximation. In this model,

as shown in figure 3.1.b, the incident polarized laser beam induces two point charges of Q_0 and $-Q_0$ on the metallic tip. Point charge Q_0 will induce another point charge Q_0' on the sample, which depends on the response function of the sample (β). This charge again induces an additional point charge Q_i close to the apex of the tip and a minus charge ($-Q_i$) distributed along the spheroid. This charge again induces another point charge Q_i' on the sample. The near-field interaction can be calculated again by equations (3-1) and (3-2). However, the calculation for the effective polarizability is different.

The effective polarizability of the tip for FDM is different from PDM due to tip approximations:

$$\alpha_{eff} = C\left(1 + \frac{1}{2}\frac{f_0(H)\beta(\varepsilon)}{1-f(H)\beta(\varepsilon)}\right) \tag{3-7}$$

$f_0(H)$ and $f(H)$ are function of the tip material and dimension:

$$f_0(H) = \left(g - \frac{2H+W_0+R_t}{2L}\right)\frac{ln\frac{4L}{4H+2W_0+R_t}}{ln\frac{4L}{R_t}} \tag{3-8}$$

$$f(H) = \left(g - \frac{2H+W_i+R_t}{2L}\right)\frac{ln\frac{4L}{4H+2R_t}}{ln\frac{4L}{R_t}} \tag{3-9}$$

The other three factors in equations (3-7) to (3-9) are defined as:

$$C = L\frac{Q_0}{|E_0|} \tag{3-10}$$

$$W_0 \approx 1.31R_tL/(L+2R_t) \tag{3-11}$$

$$W_i \approx R_t/2 \tag{3-12}$$

Where L is effective length of tip, R_t is tip curvature radius which is 20 nm, C is the height-independent constant with $Q_0 = R_t^2E_0$ which is the total amount of the polarization charge induced in tip in the absence of sample which is described in reference [47] , H is tip and sample distance

The reflection coefficient r_p can be calculated from [44, 48]:

$$r_p(q,\omega) \approx (\varepsilon_* - \varepsilon_0)/(\varepsilon_* + \varepsilon_0) \tag{3-13}$$

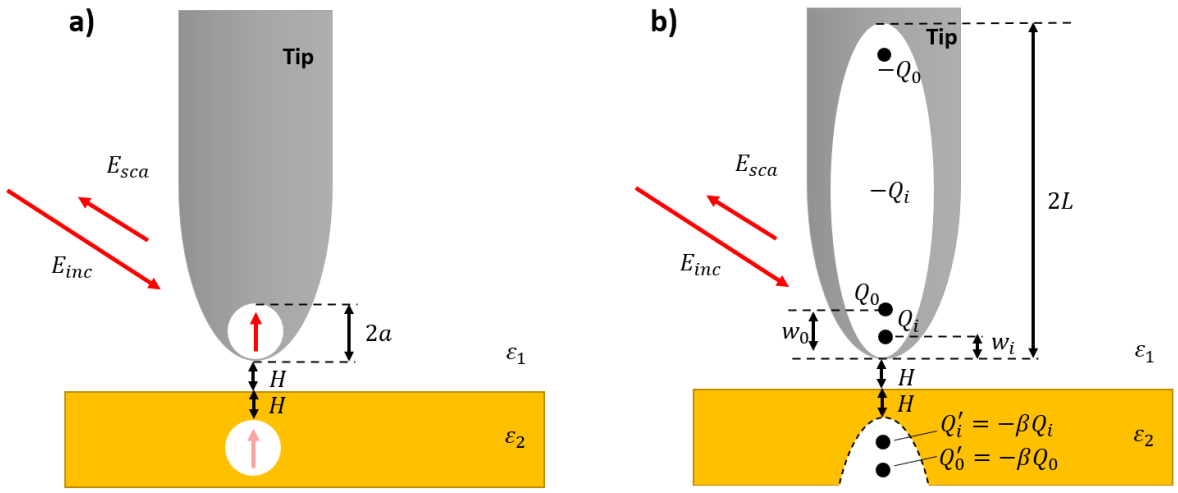

Figure 3.1 Schematic of Point Dipole Model and Finite Dipole Model.

3.1.3 Extended finite dipole model for layered systems (Multilayer Model):

The extended finite dipole model for layered samples is similar to the Finite Dipole Model. The only difference is using multilayer reflection coefficient and quasi-static near-field reflection coefficient for multilayer sample. A schematic for the extended finite dipole model for multilayer sample has shown in figure 3.2.

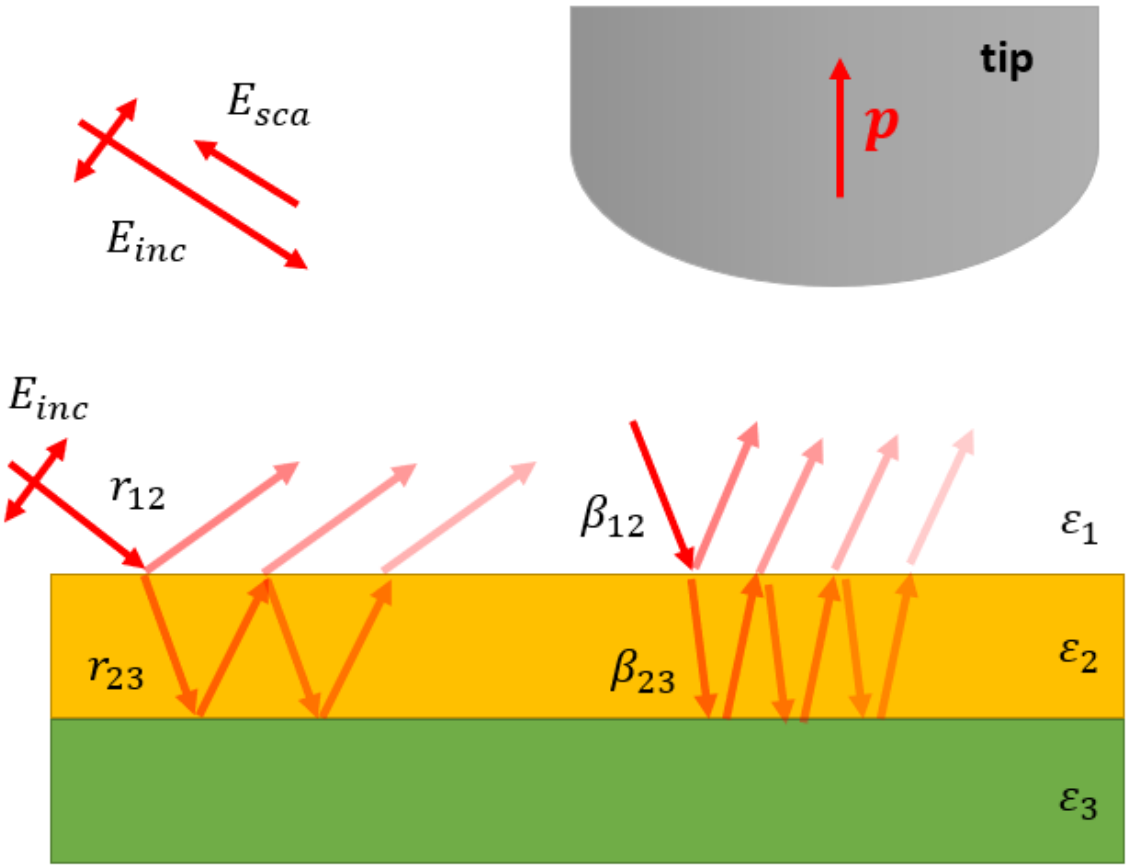

Figure 3.2 Schematic of the far-field illumination of the tip, and of the nearfield interaction/scattering between the tip and the sample.

For 3 layers of sample (air/sample/substratse) [49, 50]

$$\beta_{3L} = \frac{\beta_{12}+\beta_{23}exp\,(-2qd_1)}{1+\beta_{12}\beta_{23}exp\,(-2qd_1)} \tag{3-14}$$

$$\beta_{ij} = \frac{\varepsilon_j-\varepsilon_i}{\varepsilon_j+\varepsilon_i} \tag{3-15}$$

By replacing recursive using equation (3-15) as an expression for β_{12} [49] we derive an equation for four layers:

$$\beta_{4L} = \frac{\beta_{12}+\beta_{3L}exp\,(-2qd_2)}{1+\beta_{12}\beta_{3L}exp\,(-2qd_2)} \tag{3-16}$$

$$\beta_{4L} = \frac{\beta_{12}+\frac{\beta_{23}+\beta_{34}exp\,(-2qd_2)}{1+\beta_{23}\beta_{34}exp\,(-2qd_2)}exp\,(-2qd_1)}{1+\beta_{12}\frac{\beta_{23}+\beta_{34}exp\,(-2qd_2)}{1+\beta_{23}\beta_{34}exp\,(-2qd_2)}exp\,(-2qd_1)} \tag{3-17}$$

$$\beta_{4L} = \frac{\beta_{12}+\beta_{12}\beta_{23}\beta_{34}exp\,(-2qd_2)+\beta_{23}exp\,(-2qd_1)+\beta_{34}exp\,(-2qd_2)exp\,(-2qd_1)}{1+\beta_{23}\beta_{34}exp\,(-2qd_2)+\beta_{12}\beta_{23}exp\,(-2qd_1)+\beta_{12}\beta_{34}exp\,(-2qd_2)exp\,(-2qd_1)} \tag{3-18}$$

$$\beta_{4L} = \frac{\beta_{12}+\beta_{12}\beta_{23}\beta_{34}exp\,(-2qd_2)+\beta_{23}exp\,(-2qd_1)+\beta_{34}exp\,(-2q(d_1+d_2))}{1+\beta_{23}\beta_{34}exp\,(-2qd_2)+\beta_{12}\beta_{23}exp\,(-2qd_1)+\beta_{12}\beta_{34}exp\,(-2q(d_1+d_2))} \quad (3\text{-}19)$$

$$\beta_{4L} = \frac{\beta_{12}+\beta_a exp\,(-2q(d_1+d_2))}{1+\beta_b exp\,(-2q(d_1+d_2))} \quad (3\text{-}20)$$

Where β_a and β_b can be defined as:

$$\beta_a = \beta_{12}\beta_{23}\beta_{34}\,exp(2qd_1) + \beta_{23}exp\,(2qd_2) + \beta_{34} \quad (3\text{-}21)$$

$$\beta_b = \beta_{23}\beta_{34}\,exp(2qd_1) + \beta_{12}\beta_{23}exp\,(2qd_2) + \beta_{12}\beta_{34} \quad (3\text{-}22)$$

For r_p in 3 layer calculation [51]:

$$r = \frac{r_{01}+r_{12}exp\,(2ikd_1)}{1+r_{01}r_{12}exp\,(2ikd_1)} \quad (3\text{-}23)$$

$$r_{ij} = \frac{\varepsilon_j k_{z,i}-\varepsilon_i k_{z,j}}{\varepsilon_j k_{z,i}+\varepsilon_i k_{z,j}} \quad (3\text{-}24)$$

Where $k_{z,i} = \sqrt{\varepsilon_i(\omega/c)^2 - q^2}$. [52]. With the similar method that we used to derive β_{4L}, we can derive the equation for r_p for four layers as:

$$r_p(q,\omega) = \frac{r_{12}+r_a exp\,(2ik_z(d_1+d_2))}{1+r_b exp\,(2ik_z(d_1+d_2))} \quad (3\text{-}25)$$

$$r_a = r_{12}r_{23}r_{34}\,exp(-2ik_z d_1) + r_{23}exp\,(-2ik_z d_2) + r_{34} \quad (3\text{-}26)$$

$$r_b = r_{23}r_{34}\,exp(-2ik_z d_1) + r_{12}r_{23}exp\,(-2ik_z d_2) + r_{12}r_{34} \quad (3\text{-}27)$$

3.2 Polariton propagations

Materials with opposite signs of permittivities in their in-plane and out-of-plane axes (uniaxial materials) are known as hyperbolic media [53]. Hyperbolic materials are different from dielectric medium (all components positive) and metals (all components negative) [54]. These materials attract attention in the field of nanophotonics because these materials can concentrate light on a scale shorter than the wavelength in free space. This advantage of the hyperbolic materials makes them a perfect candidate for superlensing applications [55]. There are two types of hyperboloid; One is two-sheeted (type I) when $\varepsilon_\perp < 0, \varepsilon_\parallel > 0$, and the other one is single-

sheeted (type II) when $\varepsilon_{\parallel} < 0, \varepsilon_{\perp} > 0$, where $\varepsilon_{\parallel}$ and $\varepsilon_{\perp}$are dielectric values for in-plane and out-of-plane respectively [53]. Figure 3.3 a shows the dielectric function of Mica for in-plane and out-of-plane axes. In two regions this material is hyperbolic. In chapter 4, are experimetns were done on type 2 region[29].

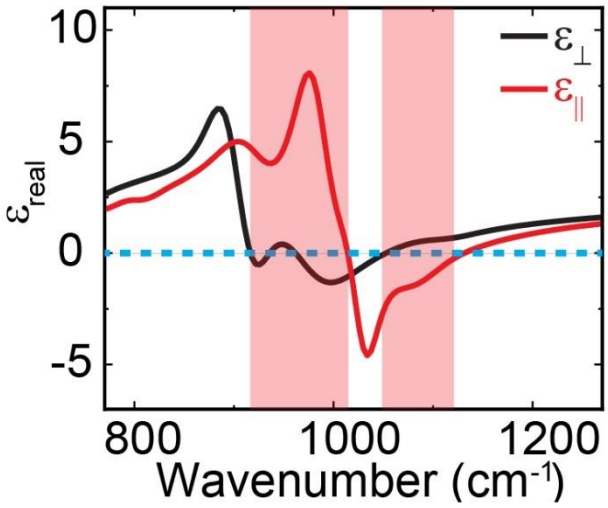

Figure 3.3 Real part of dielectric function of Mica for in-plane (red) and out-of-plane (black) axes.

Electromagnetic waves in materials propagate with wavevector k described by:

$$k_x^2 + k_y^2 + k_z^2 = \frac{\omega^2}{c^2} \tag{3-28}$$

However, for hyperbolic materials, it changes to[56]:

$$\frac{k_x^2+k_y^2}{\varepsilon_{\perp}} + \frac{k_z^2}{\varepsilon_{\parallel}} = \frac{\omega^2}{c^2} \tag{3-29}$$

The equation for the k_z can be written as:

$$k_z = \sqrt{\frac{\omega^2}{c^2}\varepsilon_{\parallel} - \frac{\varepsilon_{\parallel}}{\varepsilon_{\perp}}\left(k_x^2 + k_y^2\right)} \tag{3-30}$$

For large values of $q = \sqrt{\left(k_x^2 + k_y^2\right)}$, equation (3-30) can modify to:

$$k_z = \sqrt{-\frac{\varepsilon_{\parallel}}{\varepsilon_{\perp}}\left(k_x^2 + k_y^2\right)} = \frac{q}{\psi} \tag{3-31}$$

On the other hand, by neglecting the dissipation, the Fabry-Perot quantization condition gives:

$$2k_z d + 2\phi_a + 2\phi_a = 2l\pi \tag{3-32}$$

Where $\phi_a$and ϕ_s are the phases of reflection coefficients for r_a (reflection from air-hBN interface) and r_s (reflection from hBN-substrate interface), respectively [57].

$$\phi_j = tan^{-1}\left(\frac{\varepsilon_j}{\varepsilon_{\parallel}\psi}\right) \tag{3-33}$$

Combining equations (3-31) to (3-33) will give[58]:

$$q = -\frac{\psi}{d}\left[tan^{-1}\left(\frac{\varepsilon_0}{\varepsilon_{\parallel}\psi}\right) + tan^{-1}\left(\frac{\varepsilon_s}{\varepsilon_{\parallel}\psi}\right) + \pi l\right] \tag{3-34}$$

CHAPTER 4

4. Phonon polariton imaging[1,2]

[1] A. Fali, T. G. Folland, S. T. White, J. R. Matson, S. Liu, N. A. Aghamiri, J. H. Edgar, R. F. Haglund Jr., Y. Abate & J. D. Caldwell, accepted by Nature communications Vol. 9 Issue 1 Pages 4371, (2018)*

*Authors contributed equally to this work

[2] Reprinted (adapted) with permission from {A. Fali, S. T. White, T. G. Folland, M. He, N. A. Aghamiri, S. Liu, J. H. Edgar, J. D. Caldwell, R. F. Haglund Jr., Y. Abate, accepted by Nano letters Vol. 19 Issue 11 Pages 7725-7734, (2019)} Copyright {2019} American Chemical Society.

4.1 Reconfigurable infrared hyperbolic metasurfaces using phase change materials

This section is reprinted from{A. Fali, T. G. Folland, S. T. White, J. R. Matson, S. Liu, N. A. Aghamiri, J. H. Edgar, R. F. Haglund Jr., Y. Abate & J. D. Caldwell, accepted by Nature communications Vol. 9 Issue 1 Pages 4371, (2018)}.Reprinted here with permission of publisher

4.1.1 Abstract

Metasurfaces control light propagation at the nanoscale for applications in both free-space and surface-confined geometries. However, dynamically changing the properties of metasurfaces can be a major challenge. Here we demonstrate a reconfigurable hyperbolic metasurface comprised of a heterostructure of isotopically enriched hexagonal boron nitride (hBN) in direct contact with the phase-change material (PCM) single-crystal vanadium dioxide (VO_2). Metallic and dielectric domains in VO_2 provide spatially localized changes in the local dielectric environment, enabling launching, reflection, and transmission of hyperbolic phonon polaritons (HPhPs) at the PCM domain boundaries, and tuning the wavelength of HPhPs propagating in hBN over these domains by a factor of 1.6. We show that this system supports in-plane HPhP refraction, thus providing a prototype for a class of planar refractive optics. This approach offers reconfigurable control of in-plane HPhP propagation and exemplifies a generalizable framework based on combining hyperbolic media and PCMs to design optical functionality.

4.1.2 Introduction:

Optical near- and far- fields can be achieved by scattering light into the resonant modes of nano-structured materials, which collectively form optical metasurfaces[60-62]. Historically, metallic polaritonic elements[63] have been used, which are highly absorbing[64], and typically

exhibit limited tuning due to the geometric dependence of optical resonances. True reconfigurability (complete changing of the optical response) therefore becomes challenging, as it requires arbitrarily changing the shape of individual elements of the structure, the local dielectric environment, or the optical properties of the polaritonic material itself.

In this regard, phase change materials (PCMs) offer an appealing approach to introducing true reconfigurability as they undergo significant changes in optical properties upon exposure to external stimuli[65, 66]. Examples of PCM's are vanadium dioxide (VO_2) [67-70], and germanium antimony telluride (GeSbTe) glasses[65, 71], which undergo a dielectric to metallic phase transition upon heating or pulsed-laser excitation. For VO_2 this is a volatile (non-latching) phase transition, whereas GeSbTe undergoes a non-volatile (latching) transition. By integrating PCMs and polaritonic materials, changes in optical properties induced by such a phase transition can provide the means to control the polariton dispersion by changing the local dielectric environment in which the evanescent polaritonic near-fields propagate, thus they can be exploited to realize reconfigurable metasurfaces[65, 71-75]. However, one of the phases of PCMs is typically metallic and/or exhibits high optical losses. Consequently, in previous studies of surface-confined polaritons, such as surface plasmon (SPPs) or surface phonon polaritons (SPhPs), the propagation was restricted to spatial regions over the PCM where a low-loss dielectric phase was present[65, 71]. This makes concepts such as nanophotonic waveguides, grating couplers and focusing elements extremely difficult to realize in PCM-surface-polariton-based systems, despite the opportunities available.

Here we exploit two key changes in approach that overcome these previous limitations. First, we significantly reduce losses in polariton propagation by using isotopically enriched

hexagonal boron nitride[76, 77] (hBN), a natural hyperbolic[78-80] medium that supports low-loss hyperbolic phonon polaritons (HPhPs). Secondly, by implementing hyperbolic polaritons instead of the surface-confined variety[65, 71-75], the polaritons remain sensitive to local changes in the dielectric function of the ambient environment[81], but the electromagnetic near-fields are strongly confined to the volume of the hyperbolic material[78-80]. This means that HPhPs interact with spatially localized phase transitions of a PCM, yet do not suffer significant optical losses from this interaction, and thus can be supported over both metallic and dielectric phases. Crucially, we show that the difference in the local dielectric environment between the metallic and dielectric domains results in a large change in the HPhP wavelength in the hBN over each domain, which in turn results in the refraction of the mode when transmitting across the PCM phase domain boundaries. This means that the combination of hyperbolic media and PCMs employed here can be used to create refractive optical elements and waveguides[82], as well as components benefitting from full optical functionalities that to this point have been limited to far-field optics. We demonstrate such concepts using electromagnetic modelling, showing that PCM-HPhP heterostructures can be designed as optical resonators[80, 83] and metasurfaces[84, 85], as well as refractive near-field components, such as waveguides and lenses.

This combination of PCMs with hyperbolic media opens a whole new toolset for near-field optical design and structuring. Significantly, for reversible PCM transitions, any of these designs can be fully reconfigured using either thermal or laser-writing based approaches. Finally, by exploiting the increasingly wide range of different PCMs and hyperbolic materials and metamaterials (such as transition metal oxides[86]), these effects can be realized over an extended range of frequencies.

4.1.3 Results

In this chapter, VO2 sample was prepared by Dr. Haglund research lab at Vanderbilt. hBN was grown by Dr. Edgar's research group group at KSU. Simulations was done by Dr. Haglund and Dr. Caldwell research groups at Vanderbilt. The prototype device (Figure 4.1a) consists of a 24-nm thick flake of ^{10}B-enriched hBN (~99% enriched [76, 77]) transferred using low-contamination transfer techniques onto a single crystal of VO_2 grown on quartz. We use scattering-type scanning near-field optical microscopy (s-SNOM) to directly map and visualize the evanescent optical fields on the structure, corresponding to polaritonic waves of compressed wavelength λ_p, propagating primarily within the volume of the hBN slab (see Figurre. 4.1a). In s-SNOM images, HPhPs can be observed in two ways: first, polaritons launched by the tip propagate to, and reflect back from sample boundaries (e.g. a flake edge) creating interference fringes with spacing $\lambda_p/2$, which are scattered back to free-space by the tip and detected[79, 87, 88]. Alternatively, polaritons can be directly launched from sample edges and propagate across the surface to interfere with the incident field at the tip, producing fringes with spacing λ_p[76, 89]. Thus, in s-SNOM maps, a superposition of both so-called 'tip-launched' and 'edge-launched' fringes may be observed and are interpreted by considering the fringe spacing from individual waves ($\lambda_p/2$ vs λ_p) and the direction of polariton propagation.

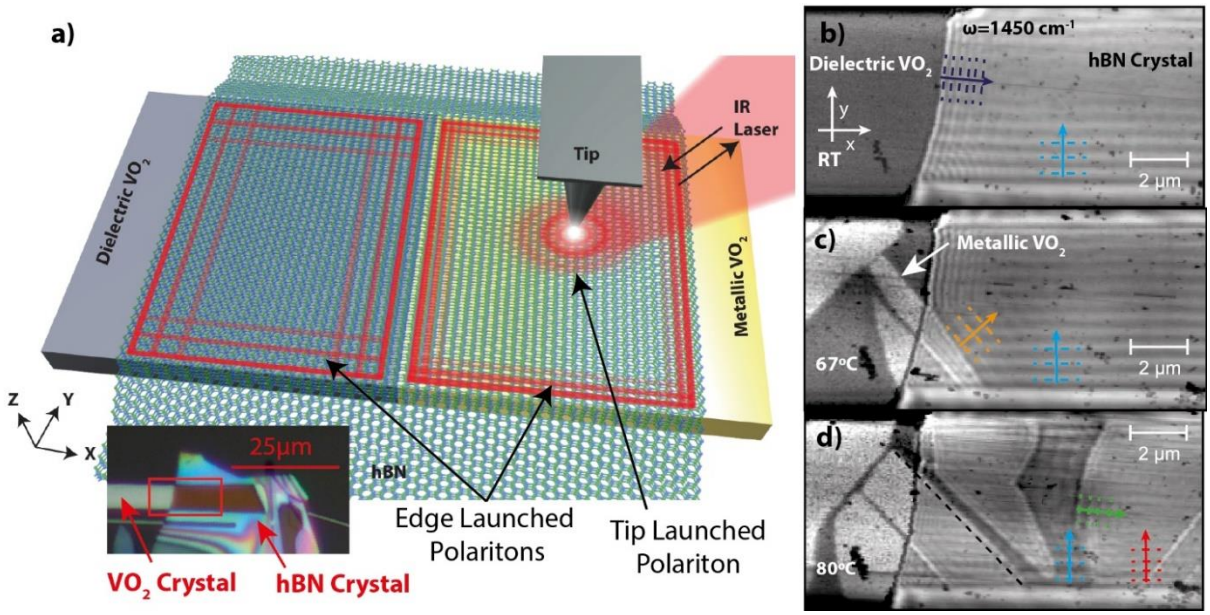

Figure 4.1 Actively reconfigurable hyperbolic metasurface device. (a) shows a device and experimental schematic, in which hBN has been transferred on top of a VO_2 single crystal and polaritons are imaged by the s-SNOM tip (b-d) s-SNOM images of the optical near-field at 1450cm^{-1} (6.9 μm) at various temperatures, showing HPhPs propagating over both metallic and dielectric VO_2 domains. The complex patterns that form are the consequence of multiple interference from the different domains. The arrows show the following: purple highlights tip-launched modes reflected from the hBN edge, while blue designates the HPhP propagating interior to the hBN from the edge of the VO_2 crystal (boundary with air, suspended hBN). The red highlights the same propagation characteristics as the blue arrow, except for HPhPs propagating over the metallic VO_2 domains. Finally, the orange and green arrows designate HPhPs propagating within the hBN from the domain boundaries between the dielectric and metallic domains of the VO_2, with the orange (green) propagating over the dielectric (metallic) domains. In Figure. 4.1d the black dashed line indicates the edge of the VO_2 metallic domain, extrapolated from the domain outside the hBN crystal.

4.1.4 Controlling hyperbolic polaritons using a PCM

The presence of both tip- (wavelength $\lambda_p/2$, purple line in the x-direction) and edge-launched (wavelength λ_p , light blue line in the y-direction) HPhPs can be readily observed in the hBN (Figure 4.1b) slab transferred on top of the VO_2 single crystal. Here, this is visualized via the

near-field amplitude s-SNOM image collected using a 1450cm^{-1} excitation laser at room temperature. The observation of both tip- and edge-launched modes in the *x*-direction, while only edge-launched modes being apparent along the *y*-direction is derived from the properties of the boundaries in the heterostructure sample (namely the edge of the hBN crystal, and the edge of the VO_2 crystal). As in previous experiments[76, 79, 89] the edge of the hBN crystal provides for both high reflection of tip-launched HPhPs as well as a sharp edge for direct launching of edge-launched modes (*x*-direction). In contrast, the small size (440 nm thickness, 6.5 μm width) of the VO_2 crystal provides sufficient momentum to robustly scatter into HPhP modes at the VO_2 crystal edges (bottom/top edges in Figure 4.1b)[76, 89]. However, the interface between VO_2 and air at the crystal edge provide a significantly reduced reflection coefficient, which suppresses tip-launched waves, as observed in prior work[71, 81]. A more detailed discussion of the occurrence of both tip- and/or edge-launched modes in our s-SNOM images is available below and in figure 4.2.

Our sample presents three different interfaces, each of which can have distinctive properties in terms of launching polaritons in the s-SNOM experiment. Observing a tip-launched mode requires a strong reflection from an interface, while observation of an edge-launched mode demands strong scattering off the sample edge. First, we consider the edge of the hBN flake. The polariton cannot propagate past the edge of the flake and therefore nearly 100% is reflected, leading to a strong tip-launched mode. On the other hand, these hBN flakes are thin (24 nm), and therefore interact only weakly with incident waves, suppressing the edge-launched mode. [81] Thus, we only observe the tip-launched mode near the hBN crystal edge.

Second, there is an interface where the hBN extends over the edge of the VO_2 crystal. As the films of hBN are continuous across the VO_2 edge, tip-launched modes can propagate over this

interface and will only be weakly reflected. This has been observed in earlier experiments.[81] On the other hand, the VO_2 crystal itself strongly scatters incident waves to launch polaritons from the VO_2 crystal edges. Therefore, we only see the edge-launched modes at the interfaces between hBN and the VO_2 crystal.

The third type of interface is the domain boundaries between dielectric and metallic VO_2. Due to the relatively small size of the domains in this sample, these show much weaker s-SNOM signals, however, the same arguments as for the edge of the VO_2 crystal hold. Therefore, we mainly see the edge-launched polaritons. This hypothesis is qualitatively supported by electromagnetic simulations of plane waves incident on these three types of boundaries, presented in figure 4.2. The results show that polaritons launched from the VO_2 crystal edge (figure 4.2a) or dielectric-metal domain boundaries (figure 4.2b) are relatively strong, whilst those initiated from the edge of the hBN flake (figure 4.2c) are relatively weak in intensity.

For the experimental efforts exploring the changes in polariton wavelength, refraction and propagation over the two VO_2 domain types, we employed a series of heating and cooling cycles with s-SNOM measurements performed at various temperatures and incident frequencies. The generalized process for these measurements is summarized in figure 4.3, whereby the sample was initial measured using S-SNOM at room temperature, then heated to various temperatures just below, within and then above the phase-change temperature, with s-SNOM measurements performed at specific temperatures within this range. Following these efforts, the sample was cooled, thereby resetting the VO_2 to the dielectric phase, where the process could be repeated with different phase change domain structures. Multiple heating and cooling cycles were performed for the experiments discussed in this work, with no changes in the response of the dielectric

functions of the constituent materials observed, thereby illustrating the reproducibility of this process.

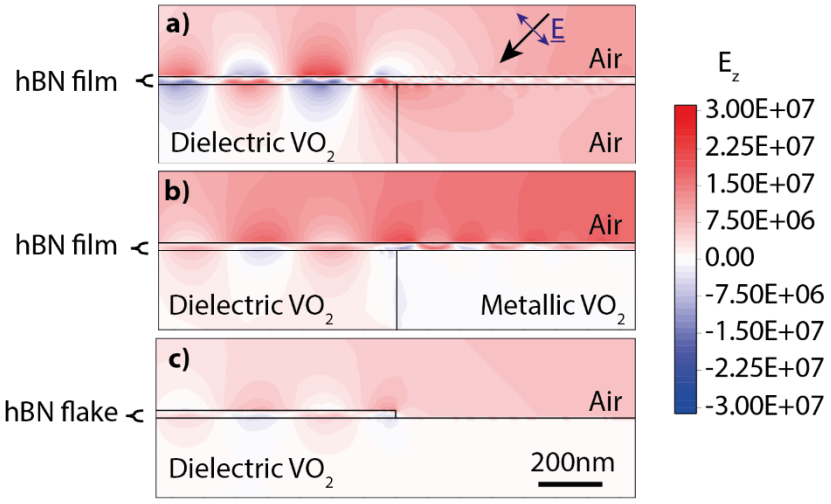

Figure 4.2 Cross sectional plot of electromagnetic fields from hyperbolic polaritons launched at the interface between a) dielectric VO_2 and vacuum, b) dielectric VO_2 and metallic VO_2 and c) at the edge of a hBN flake on VO_2. The peak electromagnetic fields launched above the dielectric domain are $\sim 2.3 \times 10^7 V/m$, $\sim 1.8 \times 10^7 V/m$ and $\sim 1.2 \times 10^7 V/m$, indicating the strongest fields are launched at the edge of the VO_2 flake, however, these simulations clearly show that edge-launched modes are highly suppressed in c).

Propagation of HPhPs is strongly influenced by the local dielectric environment[81, 84], so we investigated the influence of the VO_2 phase transition by measuring the s-SNOM response of the sample as a function of temperature, traversing the full dielectric-to-metal transition between 60-80°C[70]. To do so the sample was heated *in-situ* inside the s-SNOM microscope on a custom-built heating stage. Individual VO_2 domains are directly observed with s-SNOM due to the dielectric contrast between domains, with metallic (dielectric) VO_2 appearing as bright (dark) regions (Figure 4.1d)[67-70]. As the device is heated further (Figure 4.1e), the hBN-supported HPhPs are observed to propagate over both the metallic and dielectric domains of VO_2, for appreciable propagation distances in both regions. This contrasts with an earlier work focused on surface polaritons and PCMs, where the polaritons propagated for only a few cycles over the dielectric phase and were entirely precluded from propagation over the metallic regions[71]. We

attribute this difference to the volume-confinement of the local electromagnetic near-fields of HPhPs supported within the low-loss hBN[80], which prevents the polaritonic fields from being absorbed by the lossy metallic phase of VO_2. After heating to high temperatures, allowing the device to cool to room temperature resets the VO_2 crystal to its dielectric state, after which we can reheat the sample to get a different domain pattern (see figure 4.3). This allows us to reconfigure our device to study the propagation of HPhPs in a range of different geometries and at different frequencies within the same device. The large permittivity difference between metallic and insulating phases of VO_2 therefore presents an excellent platform to manipulate and control polariton propagation within hyperbolic materials.

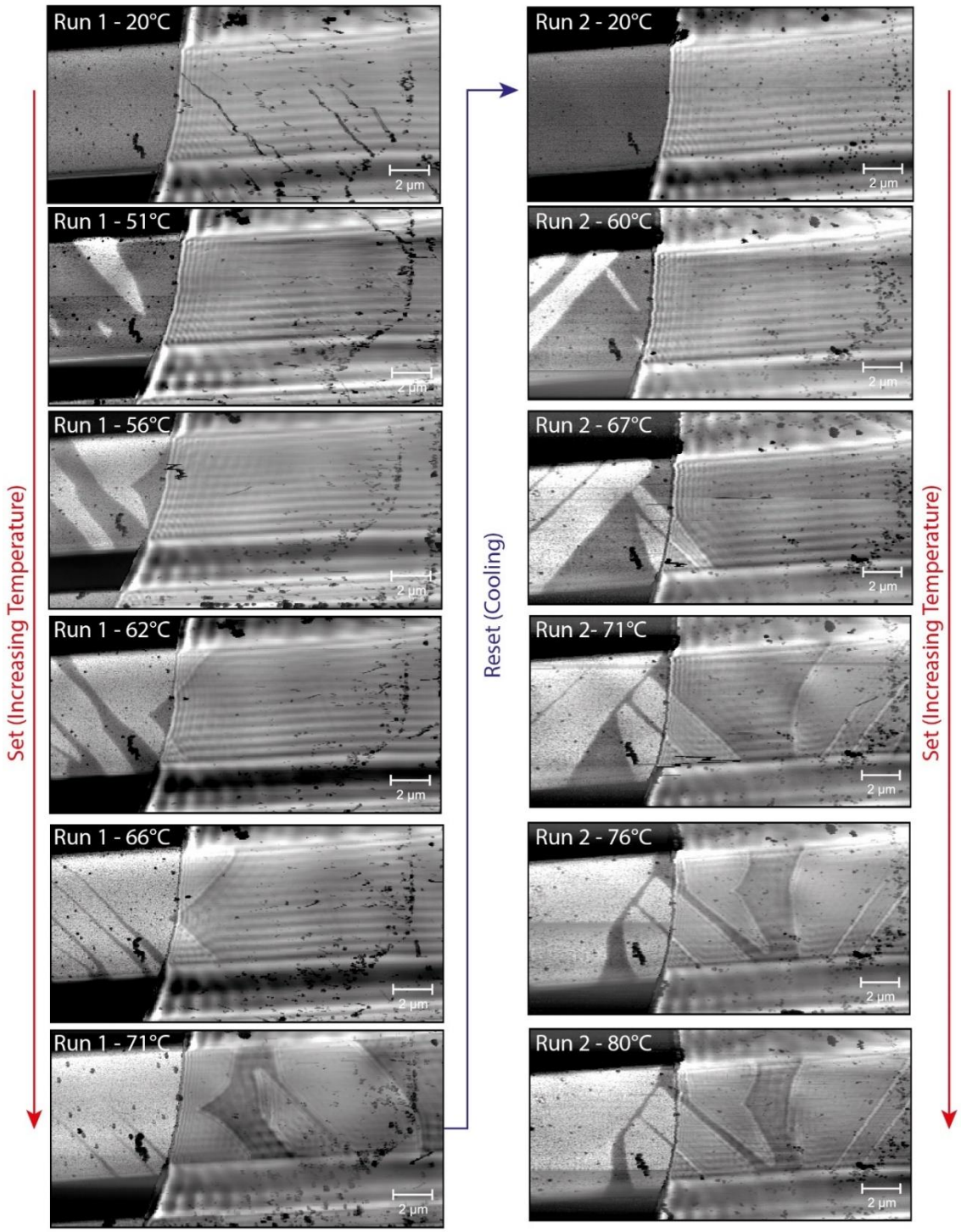

Figure 4.3. Thermally induced phase transition in VO_2 for reconfigurable metasurfaces. Here we show a series of s-SNOM images taken at the same position as the sample temperature is increased, showing the growth of metallic VO_2 domains, which manipulate polariton propagation in hBN. By cooling the device back to room temperature the device is reset to its dielectric state, and, upon reheating, form a different phase domain pattern.

When the s-SNOM maps the evanescent fields of propagating HPhP waves in the presence of multiple interfaces, complex images result from the superposition of waves launched, transmitted across and reflected by each domain boundary, crystal edge and the s-SNOM tip. The simplest polaritons to identify are the modes launched from the edge of the VO_2 crystal, as they form straight fringes aligned parallel with crystal edge. Due to the difference in local dielectric environment, these HPhPs possess different polariton wavelengths λ_p above each domain. Here the HPhP mode launched over the dielectric (metallic) domain is highlighted by the light blue (red) arrow in Figures 4.1 c and d, and demonstrate that the HPhP wavelength is tuned from $\lambda/12.9$ to $\lambda/20.4$ by the PCM at 1450cm^{-1} between these domains, this serving as the first report of the dispersion of HPhPs being tuned by a PCM. Propagation lengths $(1/e)$ are approximately 2.83 μm (5.2 cycles) and 0.8 μm (2.5 cycles) in the dielectric, and metallic phases at this frequency respectively, which is comparable to propagation lengths in naturally abundant hBN (~3.1 and 2.5 μm at the same wavevectors respectively) [79]. Furthermore, in Figure 4.1 c-e, s-SNOM images show that HPhPs are directly launched in the hBN over the boundaries between the dielectric (orange arrows) and metallic (green arrows) domains, despite there being no appreciable change in the topography of the VO_2 crystal (figure 4.4). Whilst past work has shown that PCM domain boundaries can serve to launch polaritons[71], here they are launched and propagated over both phases, with a different wavelength over each, promising the potential for reconfiguring HPhP properties and propagation dynamically. Note that the VO_2 domains appear to change size when underneath the hBN (as seen by following the black dashed line in figure 4.1d). This arises due to hyperlensing by the hBN[90, 91], which acts to magnify light scattered into a hyperbolic medium.

This can give rise to spatial regions on the edge of a domain where the wavelength appears not to change (seen just to the left of the blue arrow in Figure 4.1e).

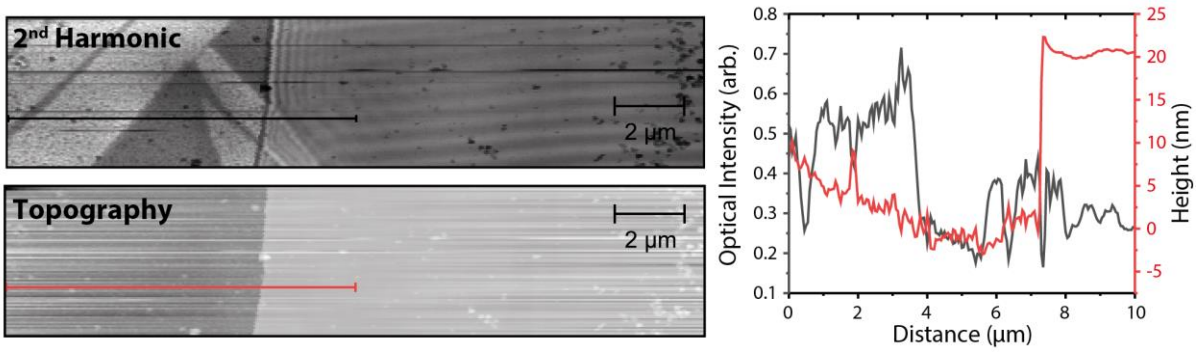

Figure 4.4. Topographic variation upon phase transition. Near-field 2nd Harmonic IR amplitude (left top) and topography (left bottom), with the correlated line profiles provided on the right (red - IR amplitude and black - topography).

4.1.5 Refraction of hyperbolic polaritons

This heterostructure also enables the transmission of polaritons across the aforementioned domain boundaries. To simplify s-SNOM images and subsequent analysis, domain geometries with only a single boundary are needed. As the positions of domain boundaries induced via thermal methods in VO_2 are naturally semi-random, we implemented multiple heating and cooling cycles (the same process as Figure 4.3) to achieve single dielectric-metal interfaces on the VO_2 crystal for study, examples shown in Figsure 4.5a,b (and also Figure 4.6). Such 'reconfiguring' of the metasurface has been repeated more than eight times in our experiments, with no appreciable change in the dielectric properties of either of the two phases of VO_2 or the hBN flake, demonstrating the repeatability of this process.

Of particular interest is the polariton wave front that propagates away from the VO_2 crystal edge in the *y*-direction (purple dashed line with black arrows in figure 4.5): it meets the domain boundary and distorts, propagating in a direction that is not normal either to the domain or crystal

edge. This is a signature of planar polariton refraction as the wave changes direction due to the local change in dielectric environment. Whilst planar polariton refraction has been reported previously for plasmon polaritons[92], this is the first direct observation of refraction for hyperbolic polaritons, and the first to study the refraction as a function of incident (transmitted) polariton angle.

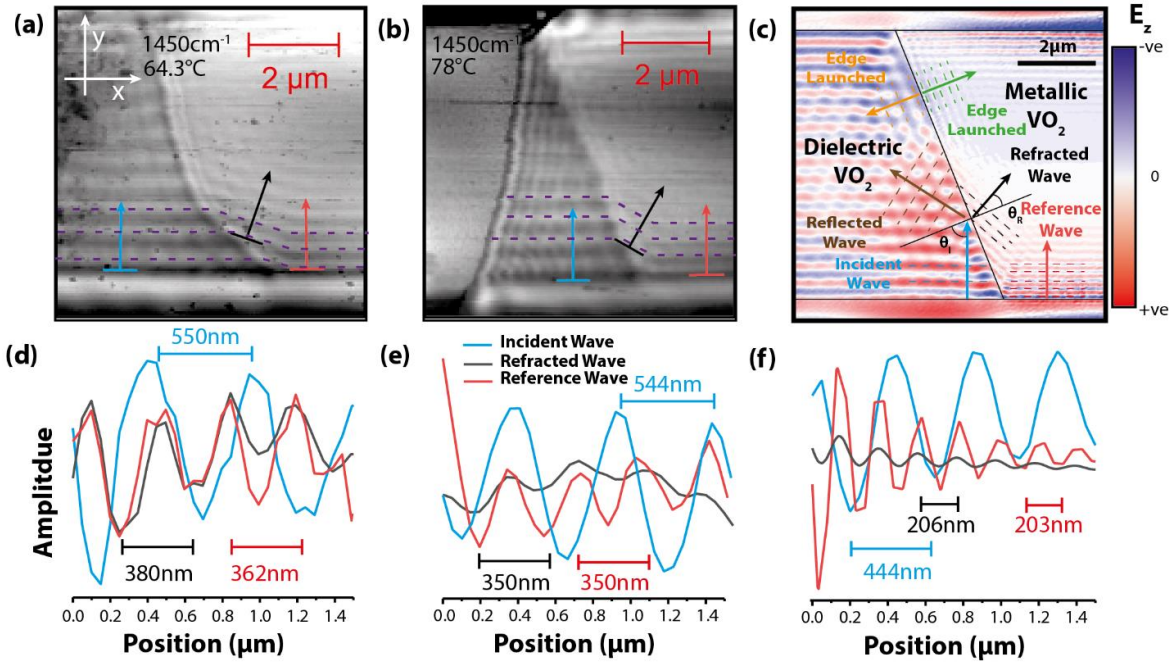

Figure 4.5 Hyperbolic polariton refraction on a hBN-VO_2 heterostructure. (a)-(b) show two s-SNOM maps of the near-field amplitude in the region of the domain boundary showing refraction. Purple dashes show the distorted phase front that propagates over the boundary. (c) shows an electromagnetic-field simulation of the geometry in (b), showing reflected, refracted and edge-launched waves. (d)-(f) show line profiles from (a)-(c) respectively, showing refraction of the wave.

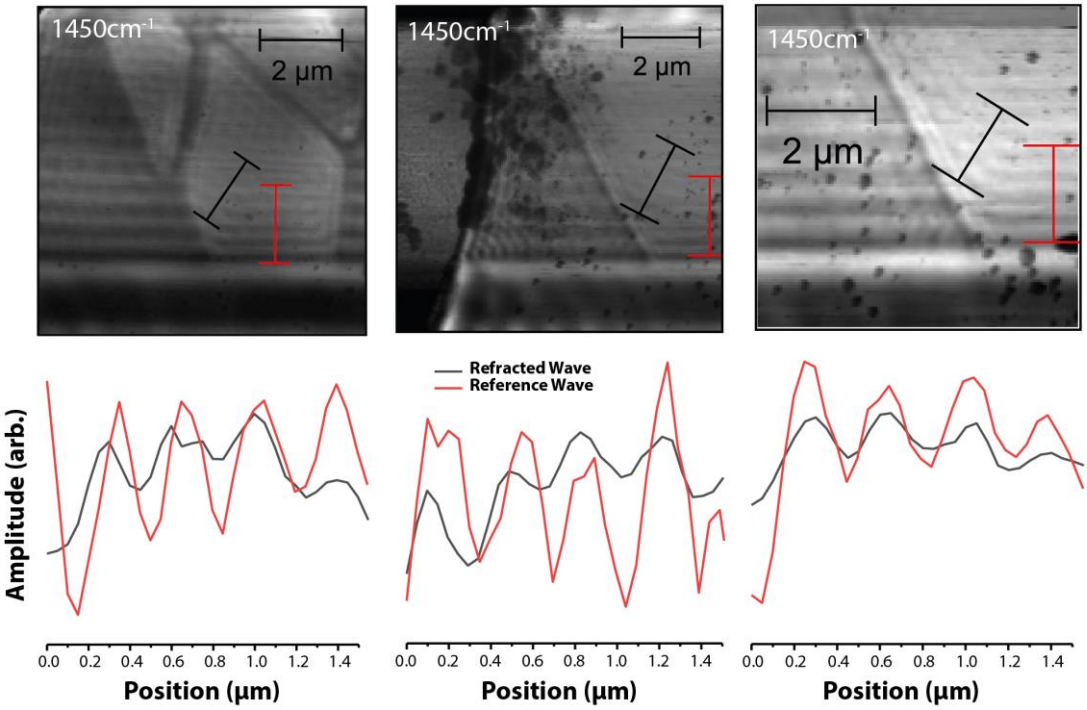

Figure 4.6 Additional images of polariton refraction in S-SNOM experiments. Dark patches on the images are contaminants that built up on the sample due to continuous imaging at high temperatures. The s-SNOM maps were collected at 1450cm^{-1} frequency and 65.5,58 and 55.7°C temperatures.

If a hyperbolic polariton traverses the boundary between different VO_2 domains, the angle of propagation changes to conserve momentum in accordance with Snell's law[93]:

$$\frac{\sin(\theta_I)}{\sin(\theta_R)} = \frac{n_2}{n_1} \tag{4-1}$$

where n_1 and n_2 are the wave-effective indices in the first and second media, and θ_I and θ_R are the corresponding angles of incidence and refraction. To demonstrate that the experimentally measured images are due to refraction, we compare the results in figure. 4.5b to a simplified electromagnetic simulation (Figure 4.5c). In the simulation we excite the structure with plane waves (45° incidence), and at the edges of the VO_2 crystal polaritonic waves are launched that propagate across the surface (mimicking edge-launched polaritons). Note that we do not consider the tip-sample interaction in these simulations. Here HPhPs excited at the edge of the VO_2 crystal

(blue) propagate in the *y*-direction within the dielectric phase. When these HPhPs approach the angled dielectric-metallic domain boundary (black line), some of the wave will be reflected (brown) and some will be transmitted across the boundary (black) and refracted due to the mismatch in wavevectors for the HPhPs supported over the two PCM domains. The simulation also shows waves launched directly from the domain boundary (orange and green) in figures. 4.1c and d. The refracted wave will not propagate normal to either the edge of the crystal or the domain boundary, but will have the same polariton wavelength as the wave launched in the hBN by scattering of incident light off the metallic VO_2 crystal edge. This is indeed what is shown in our experiments by the corresponding line profiles in figures 4.5 d-f. However, the wave reflected by the metal-dielectric domain boundary is not observed here due to interference with the edge-launched mode shown in light blue. Despite this, the good agreement between figure.4.5b and c shows clear evidence of HPhP refraction. We note that whilst in principle these effects should be observable also with a tip-launched waves in s-SNOM images, during our experiments, we were unable to form a VO_2 domain boundary sufficiently close to the flake edge (seen in figure 4.1a) to study this effect.

4.1.6 Quantifying polariton manipulation

To quantify the change in the polariton wavevector and HPhP refraction induced by the VO_2 domains and to quantify the ability to reconfigure the metasurface, we systematically studied the polariton wavelength dependence on incident frequency and refracted angle in different domain geometries. In the first case, we systematically record s-SNOM images in both metallic and dielectric domains as the monochromatic laser source frequency is varied, and subsequently extract the wavelength through Fourier analysis (see figure 4.7) of the s-SNOM maps, as has been

reported previously[76, 79, 87, 88]. The experimentally extracted polariton wavevector (symbols) agrees well with numerical calculations of the HPhP dispersion for thin hBN slabs on a substrate consisting of either the dielectric or metal form of VO_2 (figure 4.8a and b)[76, 79] . In our assignment of the points in figure 4.8a and b, we consider both tip- and edge-launched modes, above both metallic and dielectric VO_2, which can be observed in figure 4.7. The dramatic change in wavevector between domains at the same incident frequency is attributable to the large change in dielectric constant in VO_2 between the two PCM states, which further compresses the polariton wavelength.

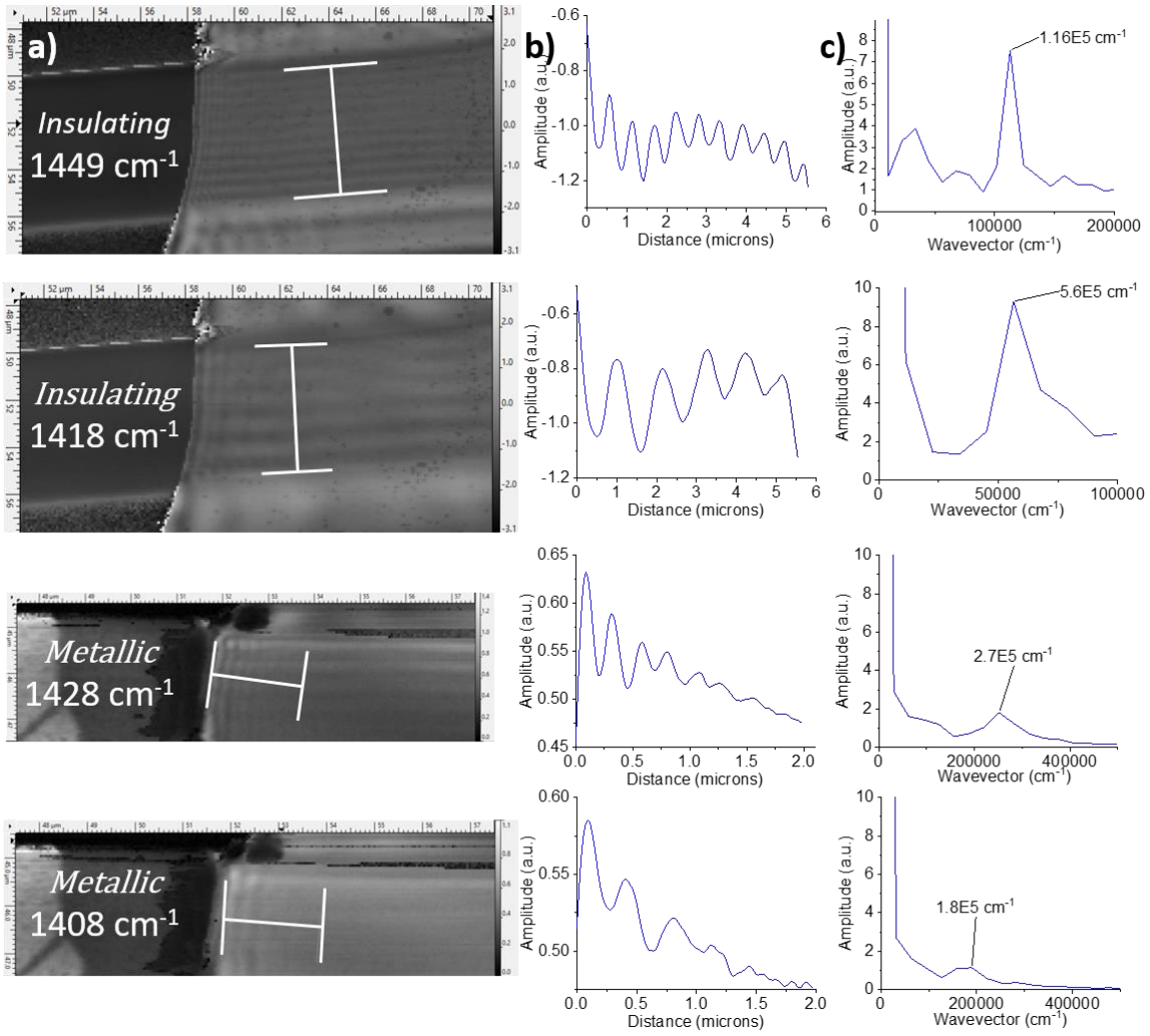

Figure 4.7 Determining the polariton wavelength for given VO_2 phases and laser frequencies. a) The s-SNOM amplitude corresponds to line-scan markers perpendicular to the dominant propagating wave. b) The line-scan profiles, taken where shown in **a**). c**)** The frequency component of each line scan was extracted using fast Fourier transforms (FFTs) with a rectangular window, and normalizing amplitude to the mean-square amplitude (MSA). The peaks show the dominant frequencies in the line scan. Peak positions were converted to wavevector and used to plot the dispersions in figure 4.8.

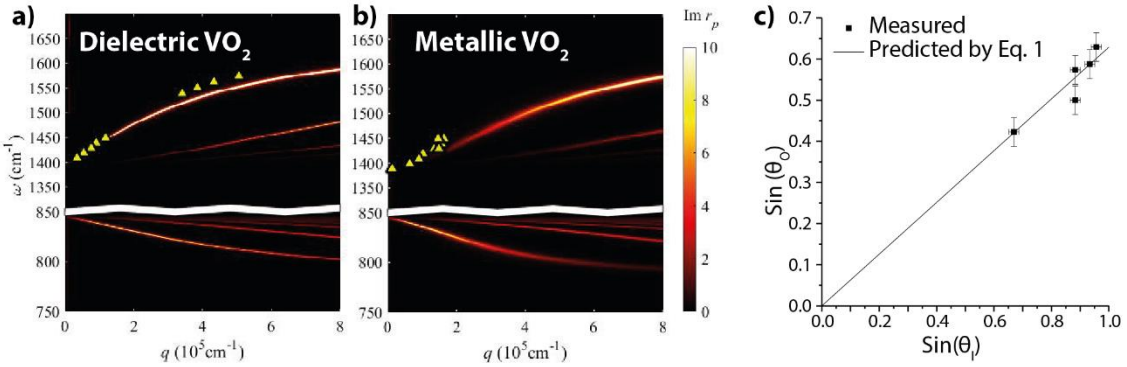

Figure.4.8 Hyperbolic polariton dispersion in VO_2 over both dielectric (a) and metallic (b) domains compared to numerical calculations. The horizontal white line shown in figure (a) and (b) indicates a break in the graph, between upper (1394-1650cm^{-1}) and lower (785-845cm^{-1}) Reststrahlen bands. From the measured dispersion, the angle of refracted waves at 1450cm^{-1}can be computed for a given incident angle and compared against experimentally measured results in (c). There has been no fitting in this result.

From the measured change in polariton wavelength, we calculated the ratio of the indices of refraction, n_1/n_2 to determine the expected angle of refraction for the HPhP waves from equation. (4-1), and compared this to the refracted angle extracted from the s-SNOM images in figure 4.5 and figure 4.6, to test the adherence to Snell's law for HPhPs (figure 4.8c). This result is consistent with numerical simulations at a range of different angles and frequencies (see figure 4.9) confirming that Snell's law holds for HPhPs propagating across domain boundaries. Systematic investigation of polariton propagation and refraction at multiple angles was not possible in prior work[92] and thus, the results presented here demonstrate that the tools and concepts of refractive optics are applicable in near-field optical designs as well. Indeed, the repeatable nature of both the change in polariton wavelength and Snell's law demonstrates that this platform can steer polariton propagation by proper design of the underlying local dielectric environment.

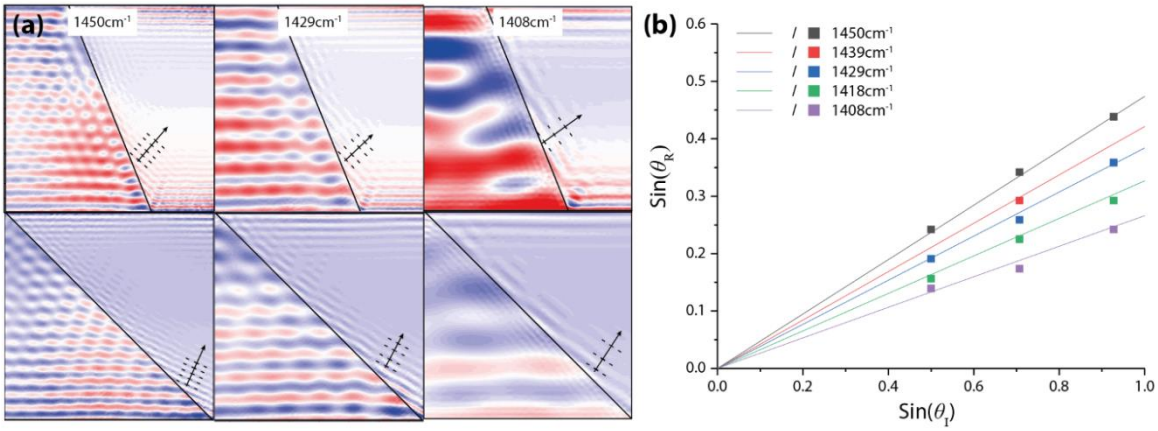

Figure 4.9 a) Electromagnetic simulations of polariton refraction at 68˚ and 45˚ with respect to the surface normal. Each image shows the refracted wave, and was used to create the data points in b). b) Snell's law tested using electromagnetic simulations. The calculations follow Snell's law closely, with discrepancies due to uncertainties in accurately determining refraction angles.

4.1.7 Towards refractive near-field optics

The ability to control HPhPs propagating across phase-domain boundaries opens several possibilities for engineering lithography-free metasurfaces and near-field optics. As an example motivated by prior work[71], we investigate the possibility for creating rewritable nanoresonators using this technique, where a periodic array of metallic square domains is created inside the VO_2 crystal underneath the hBN (inset figure 4.10.a). In figure 4.10.a we show the numerically calculated reflection spectrum from a hBN crystal on top of a dielectric VO_2, VO_2 patterned with metallic and dielectric domains, and hBN on top of patterned VO_2. In the simulated spectra for the hBN on top of patterned VO_2, we observe peaks corresponding to a series of HPhP modes. Whilst these peaks are small (as this geometry has not been optimized for an intense resonant response), these modes can be tuned in frequency by changing the width and periodicity of the metallic domain (see figure 4.1). Thus, in principle, by controlling the size and shape of the metallic domain, one can realize a resonant response that previously was only observed in

nanofabricated structures of hBN [80, 94]. Such resonators could also be achieved experimentally by adding titanium to change the local phase transition properties of VO_2[95].

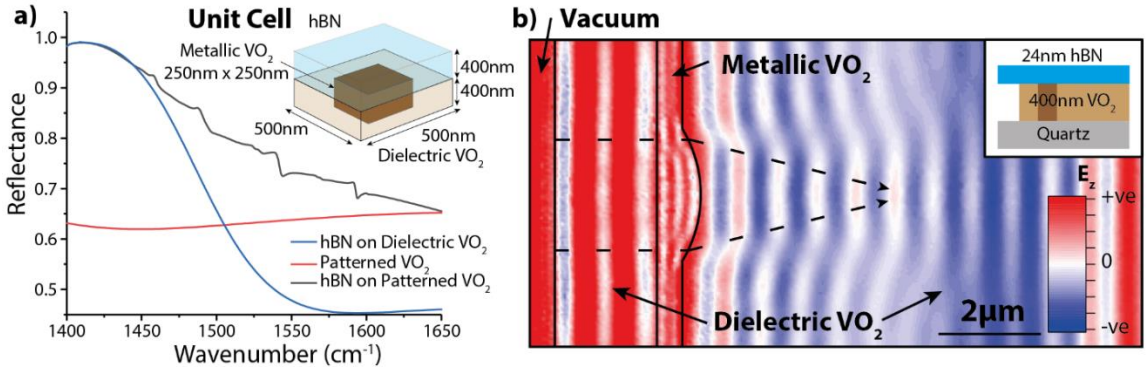

Figure 4.10 Schematic of refractive planar optics and reconfigurable resonators using phase-change materials (a) shows a tunable polariton metasurface of hBN and VO_2, which consists of a continuous film of hBN 400nm thick on top of 400nm of VO_2. By patterning the VO_2 with metallic domains we can excite a rewritable reflection profile, which cannot be generated from either of the materials alone. The pitch is 500nm, with a particle length (L). (B) shows a simulation of a refractive polariton lens, which uses a semi-circular domain of metallic VO_2 to launch polariton waves at 1418cm^{-1}.

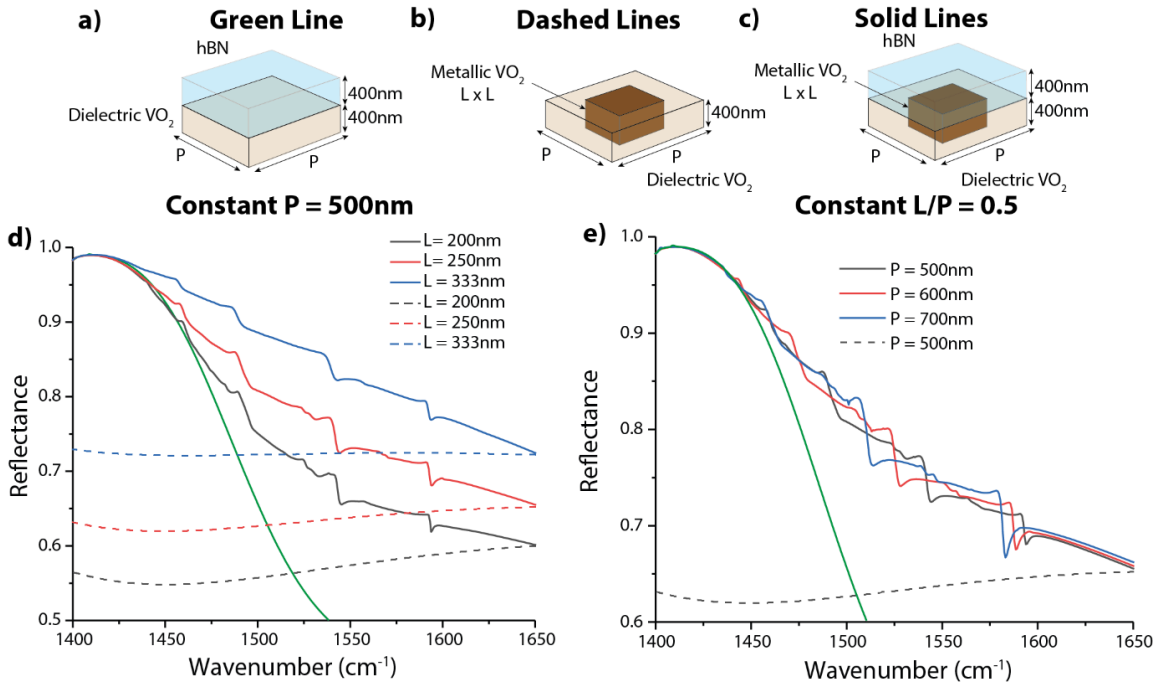

Figure 4.11 Frequency tuning of hyperbolic modes for the metasurface presented in figure 4. a) Shows tuning of the resonant modes for different metallic domain sizes at constant pitch, b) the tuning of the resonant modes for variable domain pitch.

Refraction of HPhPs across boundaries also opens the toolbox for near-field optics to include those of conventional refractive systems, for example in-plane lenses, whereby polaritons are focused to a point via refraction. A simulation of such a lens is shown in figure 4.10.b, where HPhPs are launched at the left crystal edge and propagate inward to a hemispherical metallic domain, after which they are focused to a spot. Here the combination of hyperbolic media and PCMs is critical, because for conventional surface polaritons, the high losses of the PCM metallic state would preclude polariton propagation and thus the polariton refraction required to induce focusing. While experimentally we demonstrate the principle of this reconfigurable nano-optics platform using heterostructures comprising thin slabs of hBN on VO_2 single crystals, this approach can readily be generalized to other materials. To demonstrate this, we have simulated a nanophotonic waveguide using both VO_2 and GeSbTe[71] as the underlying PCMs (See figure

4.12). The non-volatile nature of the phase change in GeSbTe[71], where both states of the PCM are stable at room temperature, offers significant benefits for laser-writing-based approaches aimed at realizing complicated nanophotonic architectures. Whilst the device we present here is a prototype, our system could be scaled by using VO_2 or GeSbTe films grown by sputtering, and boron nitride grown by metal organic chemical vapor deposition[96]. There remains numerous material challenges (such as high quality, large area hBN growth) in realizing such a system, but this provides a route to achieving scalable reconfigurable devices.

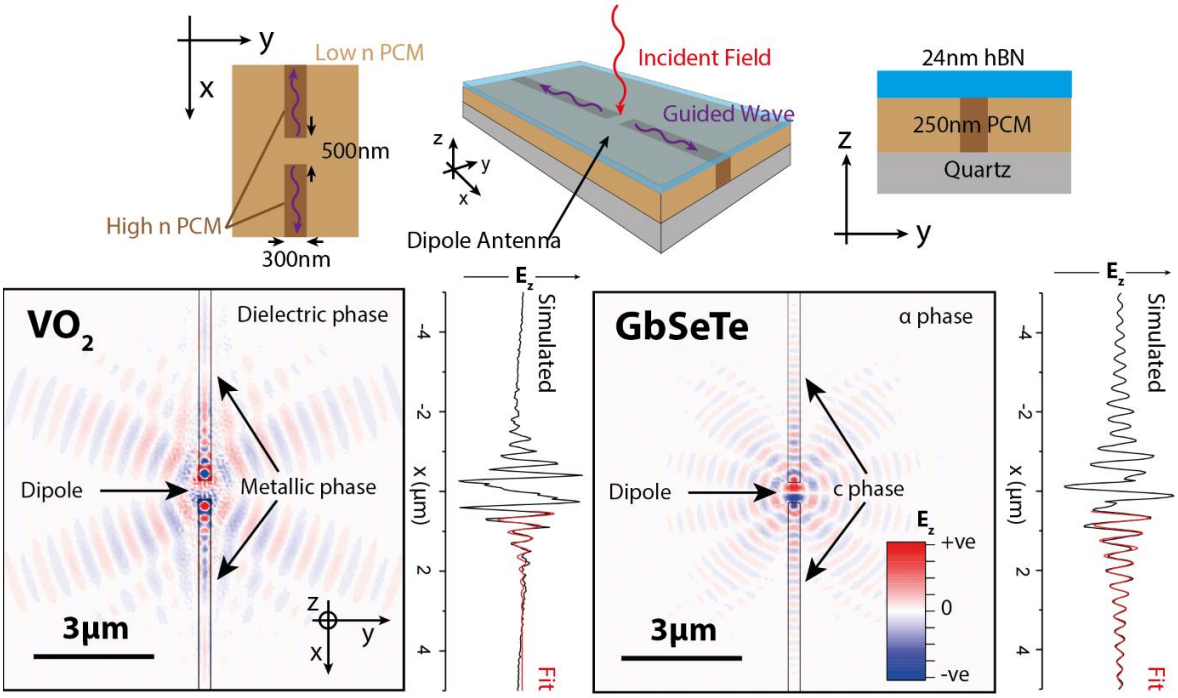

Figure 4.12 Simulation of a near-field waveguide achieved using phase-change materials. Bottom shows E_z electric field profiles taken from the centre of the hBN, with extracted line profiles from the centre of the waveguide. Red lines show fitting of a damped sine wave to the simulated data.

Here we compare the performance of VO_2 and GeSbTe PCMs for applications in creating hyperbolic polariton waveguides. Whilst the phases of VO_2 are discussed in the main text, GeSbTe also possesses both metallic and dielectric phases, which can be cycled by heating and cooling. In contrast to VO_2, the dielectric phase of GeSbTe is amorphous (α-phase), and the metallic phase is

cubic (c-phase). To simulate a hyperbolic waveguide in both materials, a 300 nm metallic/c-phase domain was formed within a dielectric/α-phase of VO_2/GeSbTe (see figure 4.12). This forms a lateral waveguide, where the high refractive index of the polariton within the strip prevents light from escaping. A small gap in the metallic phase (500 nm wide) creates an antenna that couples far-field waves into both the laterally confined waveguide mode and a radially propagating mode. For the VO_2 structure the radial wave propagates a significant distance over the dielectric domain, due to low losses inherent to the dielectric medium. However, in metallic VO_2 the guided wave is suppressed after just a few oscillations, with a $1/e$ propagation length of $\gamma = 0.57$ μm extracted by fitting a decaying sine wave. In contrast, for GeSbTe the waveguide mode appears to propagate a longer distance than the radial mode, with a decay length of $\gamma = 1.57$μm. This shows that the phenomena reported in this paper should be observable in GeSbTe films, and that this PCM might be better suited to some waveguide applications, In principle, by optimizing the waveguide width, hBN and PCM thickness it may be possible to optimize this structure to achieve long range ($>\lambda$) propagation of the polariton mode.

4.1.8 Discussion

In conclusion, we have for the first time experimentally demonstrated that the dispersion of HPhPs can be controlled using the permittivity changes inherent in the different phases of PCMs. This enables the direct launching, reflection, transmission and refraction of HPhP waves at the domain boundaries between the different phases of the PCM, due to the large change in HPhP wavelength (here a factor x1.6) that occurs for modes propagating in the hBN over each of these domains. Thermally cycling of the hBN-VO_2 heterostructure creates a range of PCM domain boundary geometries, enabling the demonstration of various near-field phenomena. By inducing

well-defined domain structures, it will be possible to design reconfigurable HPhP resonators and refractive optics in a planar format at deeply subdiffractional dimensions. Beyond the implications for integrated nanophotonics, reconfigurable HPhP resonators could be used to match resonant frequencies to local molecular vibrational modes for the realization of dynamic surface-enhanced infrared absorption (SEIRA) [97] spectroscopy. Whilst in our case we have experimentally demonstrated these concepts using hBN on VO_2, using different combinations of PCMs (such as GeSbTe) and different hyperbolic materials (such as transition metal oxides [86]), could see expanded applications over a wide frequency range. Ultimately, we anticipate that the combination of low-loss, hyperbolic materials and latchable PCMs could see applications in lithography-free design and fabrication of optical and optoelectronic devices.

4.1.9 Methods

4.1.9.1 Device fabrication

Vanadium dioxide (VO_2) single crystals were grown by physical vapor transport in a quartz tube furnace at 810°C under 1.7 Torr Ar gas at a flow rate of 25 s.c.c.m. Vanadium pentoxide (V_2O_5) powder (~0.3g, Sigma Aldrich 221899) was placed in a quartz boat ($10 \times 1 \times 1\ cm$) upstream of the desired substrates and heated for 1 hour Evaporated V_2O_5 was reduced to VO_2 in this process and deposited on quartz (0001) substrates. Representative crystals from each sample were investigated using Raman spectroscopy to identify the VO_2 phase and optical microscopy to verify the thermal phase transition. Smaller, loose crystals located on the substrate surface were removed by adhesion to a heated (60°C) layer of PMMA firmly brought into contact with the sample and subsequently retracted.

The isotopically enriched hBN crystals were grown from high-purity elemental ^{10}B (99.22 at%) powder by using the metal-flux method. A Ni-Cr-B powder mixture at respective 48 wt%, 48 wt%, and 4 wt% was loaded into an alumina crucible and placed in a single-zone furnace. The furnace was evacuated and then filled with N_2 and forming gas (5% hydrogen in balance argon) to a constant pressure of 850 Torr. During the reaction process, the N_2 and forming gases continuously flowed through the system with rates of 125 s.c.c.m. and 25 s.c.c.m., respectively. All the nitrogen in the hBN crystal originated from the flowing N_2 gas. The forming gas was used to minimize oxygen and carbon impurities in the hBN crystal. After a dwell time of 24 hours at 1550°C, the hBN crystals were precipitated onto the metal surface by cooling at a rate of 1°C/h to 1500°C, and then the system was quickly quenched to room temperature. Bulk crystals were exfoliated from the metal surface using thermal release tape. Crystals were subsequently mechanically exfoliated onto a PMMA/PMGI polymer bilayer on silicon. Flakes were then transferred from the polymer substrate onto VO_2 single crystals using a semi-dry technique, and the polymer membrane was removed using acetone and isopropyl alcohol.

4.1.9.2 Numerical simulations

Numerical simulations were conducted in CST Studio Suite 2017 using the frequency domain solver with plane waves incident at 45° and Floquet boundary conditions. In these simulations, polariton modes were only launched by scattering from edges in the simulation, and field profiles were extracted using frequency monitors. All results used thicknesses consistent with that measured in topographic maps of the samples. Dielectric functions were taken from Ref. [76] for isotopically enriched hBN, from Ref. [98] for VO_2 and from [99] for GeSbTe.

4.1.9.3 s-SNOM measurements

Near-field nano-imaging experiments were carried out in a commercial (www.neaspec.com) scattering-type, scanning near-field optical microscope (s-SNOM) based around a tapping-mode atomic-force microscope (AFM). A metal-coated Si-tip of apex radius R ≈ 20 nm that oscillates at a frequency of $\Omega \approx 280$ kHz and tapping amplitude of about 100 nm is illuminated by monochromatic quantum cascade laser (QCL) laser beam at a wavelength λ=6.9 μm and at an angle 45^o to the sample surface. Scattered light launches hBN HPhPs in the device, and the tip then re-scatters light (described more completely in the main text) for detection in the far-field. Background signals are efficiently suppressed by demodulating the detector signal at the second harmonic of the tip oscillation frequency and employing pseudo-heterodyne interferometric detection.

4.2 Refractive index-based control of hyperbolic phonon-polariton propagation

4.2.1 Introduction

Hyperbolic phonon polaritons (HPhPs) are generated when infrared photons couple to polar optic phonons in anisotropic media, confining long-wavelength light to nanoscale volumes. However, to realize the full potential of HPhPs for infrared optics, it is crucial to understand propagation and loss mechanisms on substrates suitable for applications from waveguiding to infrared sensing. We employ scattering-type scanning near-field optical microscopy (s-SNOM) and nano-Fourier transform infrared (FTIR) spectroscopy, in concert with analytical and numerical calculations, to elucidate HPhP characteristics as a function of the complex substrate dielectric function. We consider propagation on suspended, dielectric and metallic substrates to demonstrate that the thickness-normalized wavevector can be reduced by a factor of 25 simply by changing the substrate from dielectric to metallic behavior. Moreover, by incorporating the imaginary contribution to the dielectric function in lossy materials, the wavevector can be dynamically controlled by small local variations in loss or carrier density. Counterintuitively, higher-order HPhP modes are shown to exhibit the same change in the polariton wavevector as the fundamental mode, despite the drastic differences in the evanescent ranges of these polaritons. However, because polariton refraction is dictated by the fractional change in the wavevector, this still results in significant differences in polariton refraction and reduced sensitivity to substrate-induced losses

for the higher-order HPhPs. Such effects may therefore be used to spatially separate hyperbolic modes of different orders and for index-based sensing schemes. Our results advance our understanding of fundamental hyperbolic polariton excitations and their potential for on-chip photonics and planar metasurface optics.

To this end, we have explored the effects of substrates with varying refractive indices on HPhPs in isotopically enriched hBN, on suspended, metallic, dielectric and phase-change substrates. Employing the analytical model first proposed by Dai et al., [57] we show that the complex substrate dielectric function has non-trivial consequences for hyperbolic polariton propagation. The model specifically predicts that in the limit of small real substrate permittivity that the wavelength of the lowest-*k* hyperbolic polariton can be modified by up to a factor of 25, simply by transitioning from a metallic to a dielectric substrate. The trends of all hyperbolic polariton wavelengths as a function of the real part of the substrate permittivity are inverted, with metallic (dielectric) substrates exhibiting shrinking (expanding) polariton wavelength with increasing substrate permittivity. Counterintuitively, despite the increasing confinement of the polariton fields to the volume of the hyperbolic medium, the influence of such changes in the substrate permittivity upon the wavelength of the higher-order hyperbolic modes is equivalent to that of the fundamental polariton. Our experiments and calculations also highlight that the imaginary part of the substrate permittivity plays a critical role in dictating hyperbolic polariton propagation. While we report these results using hBN, the findings discussed can be generalized to the broader class of hyperbolic media. Based on our findings, we highlight their technological implications, illustrating that this offers the potential for spatially separating the fundamental from

the higher order HPhP modes within planar geometries and offers promise for advanced index-based sensing modalities by controlling the substrate dielectric function at a local level.

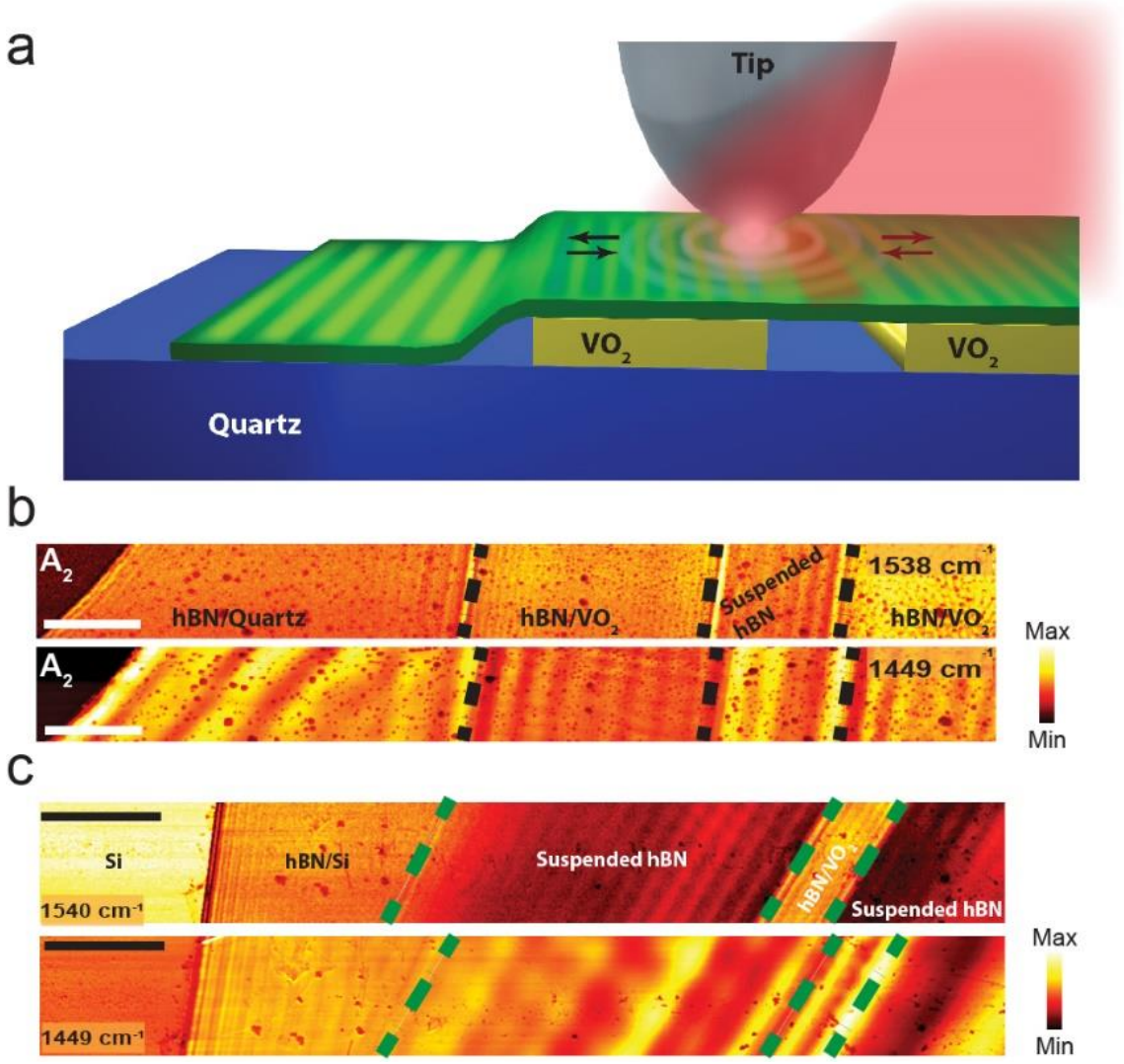

Figure 4.13 Measuring hyperbolic polaritons in different dielectric environments. (a) A schematic of the experimental setup, featuring the tip-launched HPhPs on an exfoliated hBN flake (thickness 65 nm) supported by quartz, single-crystal VO_2 and suspended in air in the region between two VO_2 crystals. The experimental s-SNOM maps of the optical amplitude at (b) 1540 cm^{-1} (6.5 μm) and 1449 cm^{-1} (6.9 μm) incident frequencies illustrate the propagation of the HPhPs in the hBN flake over these different substrates. The changing periodicity of the optical contrast in each region indicates a modified HPhP wavelength. (c) HPhP amplitude near field images taken at 1540 cm^{-1} and 1449 cm^{-1}, substrate-dependent modulation of the polariton wavelength in an hBN flake draped over a Si substrate and VO_2 crystal.. Scale bar is 5 μm.

4.2.2 Results

To quantify the role of the substrate complex refractive index on the hyperbolic polariton wavevector, we prepared several hBN flakes (see Methods) of similar thicknesses on silicon, quartz, VO_2 (insulating and metallic) and silver. We then probed the HPhPs in the hBN using a scattering-type scanning near-field optical microscope (s-SNOM) coupled to a line-tunable quantum cascade laser or a broadband IR source (Methods). When laser light is scattered from the AFM tip, HPhPs are launched by the evanescent fields induced at the tip apex, which is located in near-field proximity to the hBN surface (figure 4.13.a). These HPhPs propagate radially outward from the tip, confined within the volume of the hBN flake. Upon reaching a boundary, such as a sharp flake edge or a local domain with significant index contrast, the HPhP is reflected. This reflected polariton wave interferes with the outgoing mode to generate a pattern that can be directly probed by the s-SNOM tip, which for "tip-launched" polaritons this results in an interference pattern with a periodicity that is half of that of the incident polariton wavelength. Other HPhPs can be directly launched by IR light scattered by the flake edge, which is out-coupled to the detector via the s-SNOM tip. These "edge-launched" modes exhibit a different interference pattern with the periodicity of the incident polariton wavelength.[57, 59, 100, 101] Thus, by probing polariton wavelength and propagation length as a function of incident frequency and the complex dielectric constant of the substrate, it is possible to extract quantitatively the substrate-modified HPhP dispersion.

The HPhPs propagating within the hBN flake can be observed in the spatial profiles of s-SNOM amplitude (figure 4.13.b) collected at w=1538 and w=1449 cm^{-1}. The exfoliated 65 nm thick hBN flake is supported on quartz and draped over two VO_2 single crystals, resulting in three

regions where the hBN is suspended in air (figure 4.13.a). The near-field amplitude maps collected at both incident laser frequencies show that the separation between interference fringes, and thus the wavelength of the principal HPhP mode, is strongly modified by the refractive index of the medium over which the mode is propagating, consistent with recent reports.[81, 102-106] The polariton wavelength was similarly substrate dependent in a second hBN flake supported between a Si substrate and VO_2 crystal (figure 4.13.c).

Another exfoliated hBN flake draped over a VO_2 single crystal, here on top of a Si substrate, is presented in figure 4.13.c. Again, we observe HPhPs of different wavelengths in hBN in three different environments: on Si substrate, suspended above the substrate, and on VO_2. As discussed in the main text, the dielectric properties of the surrounding environment modulate the HPhP propagation in hBN.

To capture the dispersion of the propagating HPhPs on different substrates, we collected s-SNOM amplitude images, similar to those in figure 4.13b and c, at several incident laser frequencies. From these images we extracted line-scans parallel to the propagation direction, and then utilized a fast Fourier transform (FFT) to extract the HPhP wavelength (λ_{HPhP}), then plotting the dependence of this wavelength on laser excitation frequency (w) for each substrate (dispersion relation). We extracted the magnitude of the in-plane wavevector k, using $k=2p/\lambda_{HPhP}$. The experimental substrate-dependent dispersion relations were then determined by plotting k as a function of w (circles in figure 4.14), for HPhP modes within hBN (a) suspended in air between the two VO_2 crystals, (b) on quartz, (c) on insulating VO_2 and (d) on metallic VO_2.

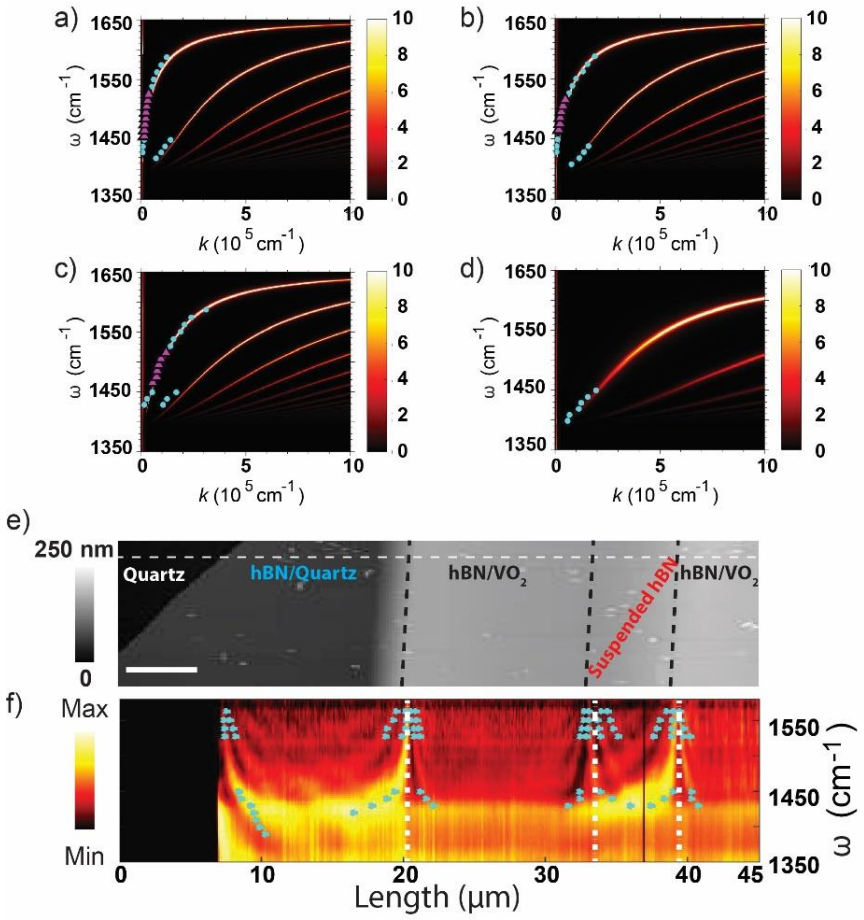

Figure 4.14 Measurements of the dispersion relations of HPhPs in 65 nm thick hBN on different substrates. The polariton wavelengths (ω, wavevectors) for each incident frequency were extracted using fast Fourier transforms of linescans extracted from the s-SNOM amplitude plots for the HPhP modes collected over the various substrates. The dispersion in these values for HPhPs propagating within hBN over a) air (suspended), b) quartz, c) insulating VO_2 and d) metallic VO_2. Circles indicate data points from s-SNOM and triangles are similar results derived from nano-FTIR spectral linescans (results from f) and are superimposed upon analytical calculations of the HPhP dispersion. The z-scale is the imaginary part of the p-polarized reflection coefficient, $Im(r_p)$ (e) Topographic maps of the sample illustrate the lack of surface features. (f) Corresponding nano-FTIR spectral linescans illustrate the HPhP properties at every

position along the broken white line in e). Solid points in f) are experimental data points extracted from monochromatic polariton images (as in figures 4.13b and c).

To supplement these results and provide experimental data in the spectral gap between 1450 to 1480 cm^{-1}, we acquired a nano-FTIR linescan that yields the relationship between the momentum *k* and the excitation frequency w at every pixel. The nano-FTIR data were acquired by collecting a broadband spectrum along the white dashed line shown in figure 4.14. e and displaying the resulting spectra in a 2D plot where the x-axis (length) is pixel location and the y-axis is the frequency (w) covering the polariton spectral range, as shown in figure 4.14.f. The line-scan covers all of the substrate environments, including suspended hBN, as well as regions where the hBN was in direct contact with quartz and VO_2, providing a *k vs* w spatial map over the various substrates in a single scan. This enabled us to extract data points outside of the range of our available monochromatic laser sources (in purple triangles in figure 4.14.a-c). [57] The experimental data are in excellent agreement with the analytical dispersion relations, as shown by the solid lines for all substrates. These calculations were performed using the analytical model reported in Ref.[57]. In the limit where the HPhP wavelength is much shorter than the wavelength within the underlying substrate, this analytic expression can be derived from the Fabry-Perot resonance condition:

$$kd = [Re(k) + iIm(k)]d = -\psi\left[tan^{-1}\left(\frac{\varepsilon_0}{\varepsilon_t\psi}\right) + tan^{-1}\left(\frac{\varepsilon_s}{\varepsilon_t\psi}\right) + \pi l\right], \psi = -i\sqrt{\frac{\varepsilon_z}{\varepsilon_t}} \qquad (4\text{-}2)$$

where d is the hBN thickness, $\varepsilon_0, \varepsilon_s, \varepsilon_t$ and ε_z are the complex dielectric functions of air, the substrate, and hBN for both in- and out-of-plane directions, respectively, and l is the mode order of the HPhP. For dielectric substrates, l=0,1, 2… however, on metallic substrates the mode $l = 0$ is not supported, due to the influence of the image charge generated in the substrate.[102] Throughout, we compare the $l = 0$ mode HPhPs on dielectric substrates to the $l = 1$ mode HPhPs

on metallic substrates, because these represent the lowest-k modes supported on the respective substrates. The three terms in Eq. 1 represent the phase shift accumulated from reflection of the HPhPs from the top and bottom of the flake, and during propagation within the layer, respectively.[57, 107] In this approximate equation, the polariton wavelength is normalized to the hBN thickness, facilitating direct comparison of the HPhP dispersion in hBN flakes of varying thickness on different substrates. This is especially important for the work presented here, as identifying flakes with the exact same thickness suitable for transfer to the various substrates studied would be a considerable difficulty. In addition to the substrates already discussed, similar measurements were made on silver and silicon. The HPhP images and dispersion plots of hBN on these substrates are provided in the figure 4.15.

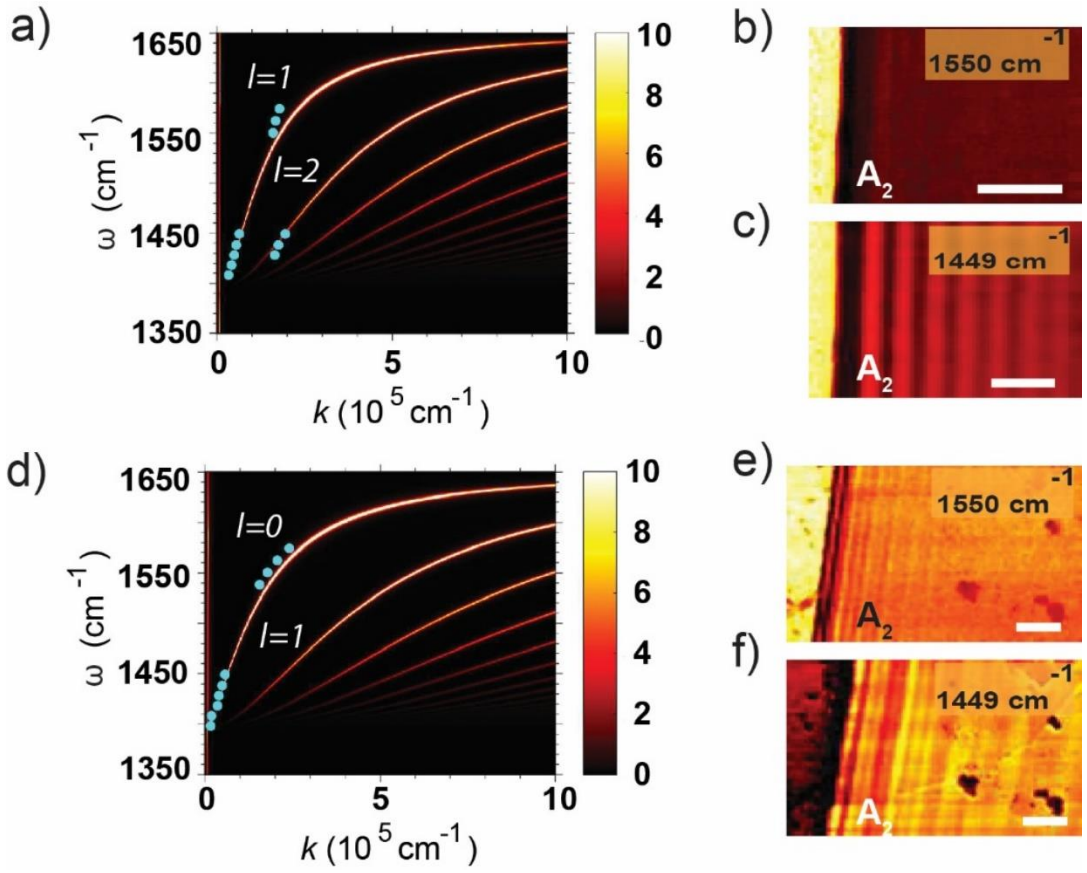

Figure 4.15. Dispersion relation of HPhP of hBN: (a) a 85 nm thick hBN flake on silver (b) and (c) HPhP amplitude near field images taken at 1550 cm^{-1} and 1449 cm^{-1}. (d) a 65 nm thick hBN flake on silicon (e) and (f) HPhP amplitude near field images taken at 1550 cm^{-1} and 1449 cm^{-1}. Experimental data points (extracted from monochromatic) are shown superimposed on analytical calculation. Scale bar is 1 μm

The dispersion relations plotted in figure 4.14 and figure 4.15 show that the wavelength of the propagating HPhPs can be altered by the choice of substrate and incident frequency, as explored in prior work.[81, 102-106] However, in this study the range of substrate dielectric properties is broader, enabling a systematic examination of the variation of the HPhP wavelength with substrate dielectric function, referenced to the intrinsic properties of suspended hBN. To compare our experimental results and theory, we plot the polariton wavevector as a function of the absolute value of the real part of the dielectric function of the substrate $[|Re(\varepsilon_s)|]$ at a single

frequency (similar plots at other incident frequencies are provided in the figure 4.16) to draw general conclusions about the dependence of HPhP modes on substrate dielectric function.

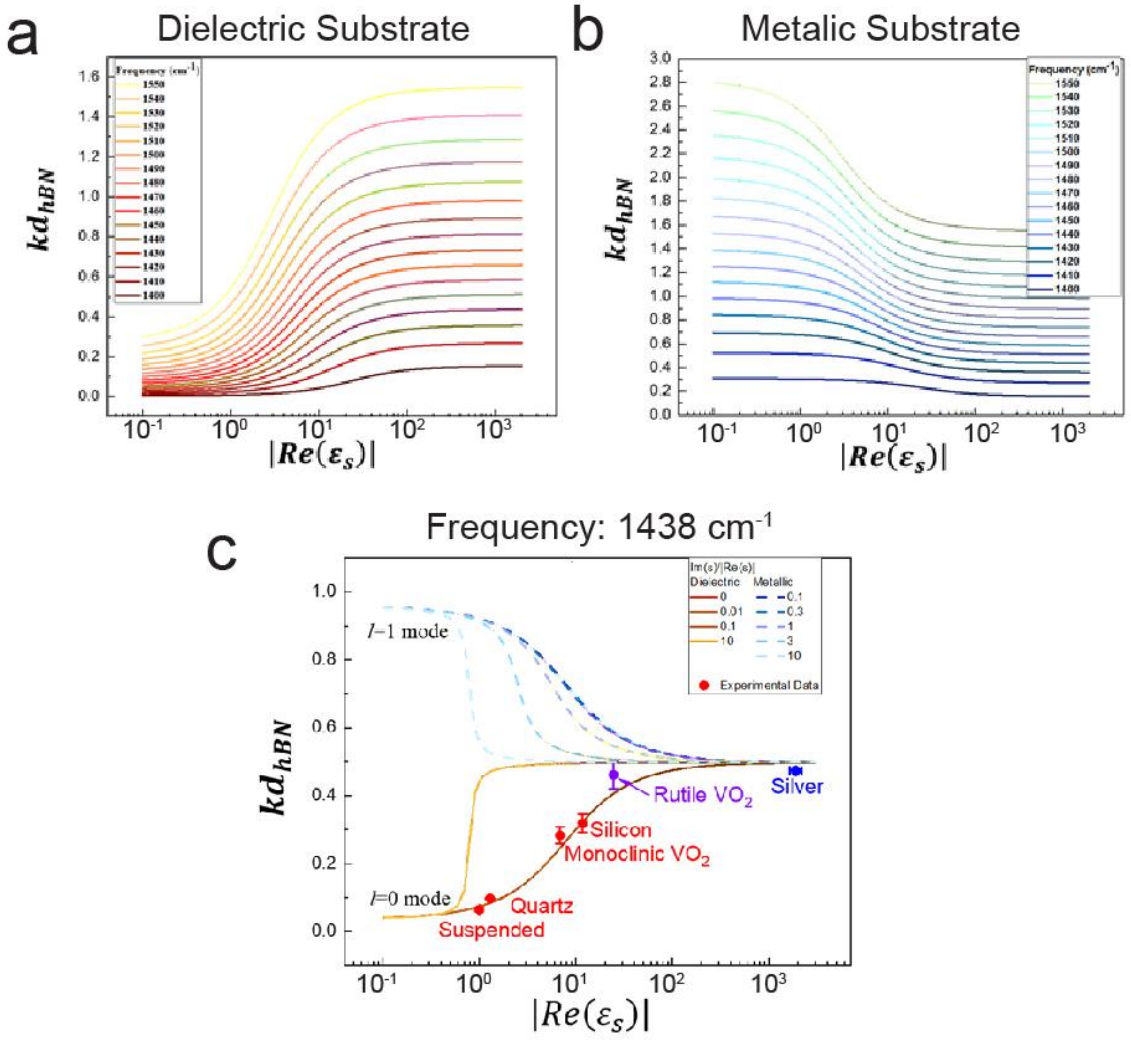

Figure 4.16. The relationship between kd and $Re(\varepsilon_s)$at different frequencies for (a) dielectric substrates ($l = 0$, and (b) metallic substrates ($l = 1$). (c)The thickness normalized wavevector (kd_{hBN}) dependence upon the real permittivity of the substrate dielectric function at 1438 cm^{-1}. This dependence is plotted for $l = 0$mode for dielectric (red shaded lines) and $l = 1$ mode for metallic (blue shaded lines) substrates with the shade indicative of the loss tangent (see legend). The red, blue and purple circles are derived from the experimental data presented in this work.

To make consistent comparisons between theoretical and experimental results on hBN flakes of varying thicknesses between the different substrates, we make two simplifications. First, we consider the dimensionless HPhP wavevector *kd*, calculated by multiplying the HPhP

momentum by the flake thickness, to normalize the dispersion relationship, as in equation (4-2). The thickness dependence of hyperbolic polariton dispersion is a consequence of the Fabry-Perot behavior of hyperbolic modes in thin slabs.[57, 107] Second, we make assumptions about the relative magnitudes of the real and imaginary parts of the substrate dielectric function to account for absorption. Lossless IR dielectrics such as silicon have $Im(\varepsilon_s) = 0$; however for metals and polar materials, the real and imaginary parts of the dielectric function are coupled by the Kramers-Kronig relations. For many metals, in the spectral regions we probe, the imaginary part of the dielectric function satisfies $0.1 \leq Im(\varepsilon_s)/|Re(\varepsilon_s)| \leq 0.3$, [108] whereas for polar dielectrics $0.01 \leq Im(\varepsilon_s)/|Re(\varepsilon_s)| \leq 0.1$.[109] In certain classes of poor metals, as well as non-crystalline materials, $Im(\varepsilon_s) \gg |Re(\varepsilon_s)|$, [110] with $Im(\varepsilon_s)/|Re(\varepsilon_s)|$~10 being typical. Thus $Im(\varepsilon_s)/|Re(\varepsilon_s)|$ (the loss tangent) is a good measure of substrate loss properties.

The analytical (equation (4-2) with *l*=0 for dielectric and *l*=1 for metallic substrates) and experimental results for the normalized wavevector as a function of $|Re(\varepsilon_s)|$ are plotted in figure 4.18. The absolute magnitude of the real part is chosen to ensure metallic and dielectric species can be compared on the same scale. A range of analytical curves representing different $Im(\varepsilon_s)/|Re(\varepsilon_s)|$ ratios, for both positive (dielectric) and negative (metallic) $Re(\varepsilon_s)$ at 1438 cm^{-1} are provided. Experimental data are represented as solid points, with error bars derived from the range of dielectric functions for each substrate for the x-axis [108, 111-114] and from measurement uncertainty in the hBN flake thickness and wavevector for the y-axis. We compare theory and experiment by considering dielectrics $[Re(\varepsilon_s) > 1, Im(\varepsilon_s) \ll Re(\varepsilon_s)]$, metals $[Re(\varepsilon_s) < 0, Im(\varepsilon_s) < Re(\varepsilon_s)]$ and highly absorbing materials $[Im(\varepsilon_s) > Re(\varepsilon_s)]$ separately. If there is little dispersion in the substrate dielectric function, the trends measured at the specific frequency

reported in figure 4.16.c will be generic to other frequencies. More pronounced effects can occur in the presence of absorption bands, where strong spectral dispersion occurs and could be treated by applying this analysis at other frequencies, as in figure 4.16.a and b.

First, we consider dielectric substrates. Analytical results (solid lines) indicate that the HPhP wavevector increases monotonically as a function of substrate permittivity $Re(\varepsilon_s)$, with only minimal influence from substrate-induced absorption loss. Red points indicate experimental data for HPhP modes within hBN on dielectric substrates in this experiment (suspended, quartz, silicon and monoclinic VO_2), which offer good quantitative agreement with the analytical model. This demonstrates that hyperbolic polaritons will exhibit a larger polariton wavevector (smaller wavelength) on higher permittivity dielectric substrates and is nominally insensitive to substrate loss within the range of typical loss tangents for such materials, $Im(\varepsilon_s)/|Re(\varepsilon_s)| < 0.1$. We also emphasize that as $Re(\varepsilon_s)$ tends towards infinity, the value of *kd* tends to a frequency-dependent constant (ψ), which can be interpreted using equation (4-2). The only term that includes the substrate dielectric function is $tan^{-1}\left(\frac{\varepsilon_s}{\varepsilon_t \psi}\right)$, which defines the influence of the phase accumulated upon reflection of the hyperbolic wave from the substrate surface. As the dielectric function becomes larger, the phase of the reflected polariton tends towards π/2. We attribute the increase in phase shift to the reduced penetration depth in substrate, with a large real part of the dielectric function, which appears analogous to the Goos-Hänschen shift.[115] The longest absolute HPhP propagation length, compared to all the substrates considered in this study, is over the suspended region between the two VO_2 crystals, as confirmed by analytical calculations, and measured in prior work[104], while the shortest is observed over metallic substrates[105].

The propagation characteristics of the HPhP modes on metallic substrates are less intuitive. Analytical predictions for metallic substrates are shown as dashed lines in figure 4.16.c. For negative permittivity substrates, the tan^{-1} term in equation (4-2) becomes negative, resulting in a negative shift in the reflected phase. To provide a direct comparison between dielectric and metallic substrates, we set the minimum l=1. As the substrate becomes more metallic (i.e.. $Re(\varepsilon_s)$ becomes more negative) the magnitude of the HPhP wavevector is reduced. In the limit of large absolute values of the dielectric permittivity, the wavevectors of HPhPs in hBN over both metallic and dielectric substrates converge. For metals, this occurs when the plasma frequency is significantly larger than that of the HPhP mode, and thus the complex dielectric constant of the substrate comprises a large negative real permittivity and correspondingly large imaginary part. From the analytical calculations shown in figure 4.16.c, it would appear at first glance that the dispersion is more sensitive to losses for metallic substrates; however, this is due simply to the higher loss tangents associated with metals. This is consistent with our calculations for dielectrics, as no light can enter any material in which $Re(\varepsilon_s) \ll 0$, and hence experiences a $\pi/2$ phase shift upon reflection. In this study, we compared the analytical model to a single noble metal (silver), with the experimentally extracted wavevector quantitatively matching with our calculations at multiple incident frequencies.

Finally, we consider a highly absorbing material, represented by rutile (metallic) VO_2. The dielectric function of rutile VO_2 has not been measured extensively in this frequency range for single crystals, however, a recent paper has addressed this deficiency for certain types of deposited films. [110] Reference [116] indicates, however, that VO_2 is properly classified as a 'bad metal' as it fails to satisfy the Wiedemann-Franz law; therefore, we take it to be an overdamped material

with $Im(\varepsilon_s) > |Re(\varepsilon_s)|$. If we assume a large loss tangent, $\frac{Im(\varepsilon_s)}{|Re(\varepsilon_s)|} \sim 10$, we find that regardless of whether rutile VO_2 is considered a bad metal or a lossy dielectric, there is minimal influence upon the normalized wavevector. To highlight the ambiguity in this case, we plot the wavevector of HPhPs supported in hBN on rutile VO_2 as a purple circle.

The good quantitative agreement between experiment and the analytical model clearly indicates the broad applicability of this approach for HPhPs, demonstrating that it is indeed capable of reproducing the influence of the substrate, regardless of loss or magnitude or sign of the permittivity in a generalized fashion for all hyperbolic media. However, it is important to note that the analytical model of equation (4-2) is only appropriate in the large *k* limit; that is when $k \gg k_s$. Outside of this regime numerical methods more accurately describe dispersion. However, the general trends for both the analytical and numerical models are nearly identical regardless of regime, with the numerical results being required for conditions where *k* and $2\pi n_s/\lambda_0$ are of the same order, as shown in the figure 4-17 a and b. Thus, conclusions drawn from the analytical model are representative of the mode behavior in hBN even for thicker flakes.

To investigate the effect of the substrate refractive index on higher-order modes, we again plot the analytical dispersion relation in figure 4.17 c and d, including now the *l*=1(2) and *l*=2(3)modes at 1510 cm^{-1} and a loss tangent of 0.01 (0.3) for dielectric (metallic) substrates. These higher-order branches correspond to shorter-wavelength polariton modes that are supported within the hyperbolic medium at the same incident frequency [101, 117] (figure 4.14). As with the principal HPhP mode, these high-order polaritons are also affected by the substrate dielectric function; however, due to the reduced range of the evanescent field associated with the shorter polariton wavelengths, one would expect this effect to be significantly reduced. However, the

change in wavevector $\Delta k = k(\varepsilon_{s1}) - k(\varepsilon_{s2})$, from a low ε_s substrate with wavevector $k(\varepsilon_{s1})$ to a high ε_s substrate with wavevector $k(\varepsilon_{s2})$ is actually the same for all hyperbolic modes. Naively, this suggests that the substrate will have the identical influence on all higher-order modes in the hyperbolic material, with no significant change in the properties of different modes other than the degree of volume confinement.

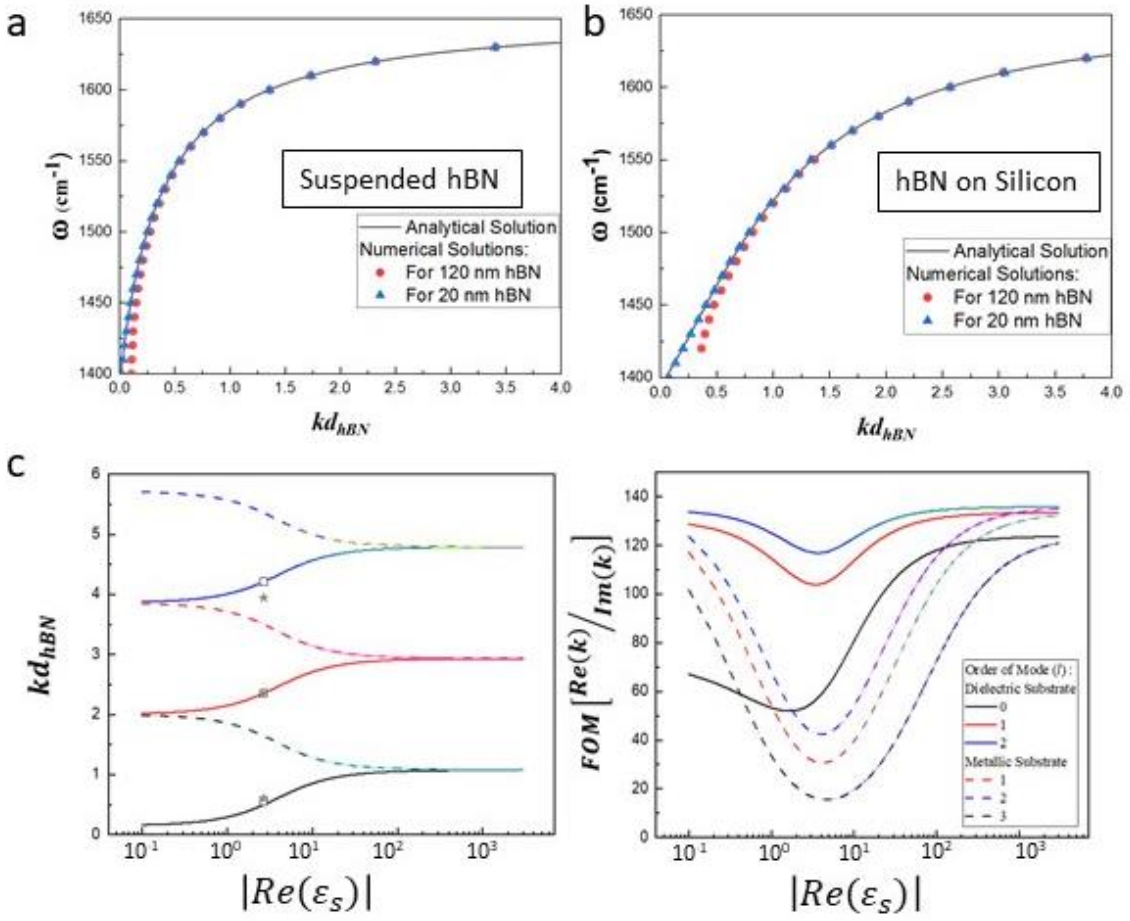

Figure 4.17 Comparison of numerical and analytical solutions as a function of frequency, for different hBN thicknesses, suspended (top left) and on Si (top right). The thickness-normalized wavevector kd is plotted to suppress the influence of hBN thickness. Blue (red) triangles (circles) are numerical solutions at 20nm (120nm). The analytical solutions (solid lines) diverge from the numerical solutions in thick flakes at low frequencies. (c) Influence of substrate dielectric function upon high-order HPhP modes of hBN at 1510 cm^{-1}, for dielectric (metallic) substrates, with the loss tangent fixed at 0.01 (0.3). c) $k \cdot d$ was plotted versus $|Re(\varepsilon_s)|$, and gray stars are experimental data in Ref. [101] , while open boxes are numerical solutions for 120 nm thick hBN. (d) FOM of the first three orders of HPhPs in this same thickness flake of hBN as a function of the $|Re(\varepsilon_s)|$.

However, the *fractional* change in wavevector $\frac{k(\varepsilon_s)}{k(\varepsilon_{s\prime})} = 1 + \frac{\Delta k}{k(\varepsilon_s)}$ is often a more useful metric in comparing HPhP propagation, where $\varepsilon_{s\prime}$ refers to a second substrate to which the first is compared. This is because phenomena such as refraction are entirely dependent on the fractional change in wavector, as indicated by Snell's law. For higher-order modes, with larger initial values of *k*, this fractional change becomes smaller, approaching unity—i.e. the higher-order modes are less sensitive to the substrate dielectric function. For example, between air and silicon (at 1510 cm^{-1}) the wavelength changes by factors of 7.4 and 3.1 for the first- ($l = 0$) and second- ($l = 1$) order modes, respectively. This has significant implications for the behavior of HPhP propagation across substrate boundaries; for example, lower-order modes are more strongly refracted at such boundaries, an effect that could be exploited to separate the different higher-order modes as demonstrated below (figure 4.18). While the experimental methods deployed here precluded observation of higher-order modes due to the thinness of the hBN flakes - chosen to ensure the validity of the analytical model – we have added data from Ref. [101] as well as numerical solutions from the model in Ref. [57] to validate these conclusions figure 4.17c). The experimental data agree well with predicted mode positions, with slight deviations for the $l = 2$ mode attributed to the challenges associated with launching high wavevector modes and the concomitant error in extracting the polariton wavelength given the correspondingly short propagation lengths.

To compare propagation properties of HPhP modes on different substrates we use a figure of merit (FOM) [101] related to the real and imaginary parts of the wavevector:

$$FOM = \frac{Re(k)}{Im(k)} \tag{4-3}$$

This FOM offers a better descriptor of the behavior than the propagation length as it to accounts for the stronger confinement of the polaritonic fields typical of correspondingly shorter propagation lengths. Furthermore, while long propagation lengths can be realized for weakly confined polaritons, it is only within the limit of strong modal confinement that the intrinsic benefits of sub-diffractional wavelengths associated with polaritons can be exploited. Specifically, $Im(k)$ determines the propagation length $L_p = \frac{1}{2 \cdot Im(k)}$,[104] and *Re(k)* defines the polariton wavelength $\lambda = \frac{2\pi}{Re(k)}$, and thus the FOM can be expressed as:

$$FOM = \frac{2\pi}{\lambda} \times 2L_p = 4\pi Q \tag{4-4}$$

where λ is polariton wavelength, L_p is propagation length, and Q is the quality factor that defines the number of cycles that the polariton wave oscillates before the amplitude decreases to 1/*e* of its initial value. The relationship between this FOM and the substrate dielectric function is plotted in figure 4.17d, using the loss tangents from figure 4.17c.

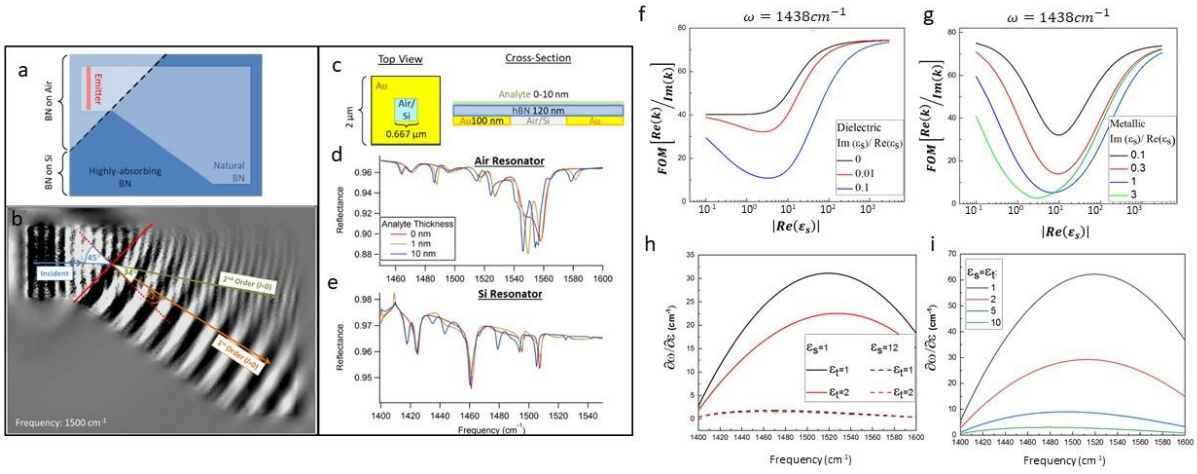

Figure 4.18 imulations of spatial separation of the HPhP modes and applications of HPhPs through dielectric enviornment control. a) A schematic diagram of the proposed HPhP spatial separator device, with the corresponding b) simulated electric field (E_z) for HPhP modes separated due to refraction resulting from HPhP transmission over a Si-air interface aligned at 45° with respect to the propagation direction. To eliminate complexities in the image due to back reflections, a notional highly-absorbing hBN border with a 20-fold increase in the damping constant was

added. The corresponding refraction of the $l = 0$(orange) and $l = 1$ order (green) HPhPs are provided. c) Schematic diagram of a proposed hBN HPhP-based SEIRA or index-sensing resonant device induced due to large index contrast in spatial regions underneath the hBN flake as designated. The corresponding reflection spectra for this resonant structure fabricated from a hBN flake over an empty d) or Si-filled e) resonant chamber (e.g. hole). The calculated resonance spectra are highly sensitive to the presence and thickness of an analyte layer on top of the hBN surface; suspended hBN films have the highest degree of sensitivity.The spectra provided for both cases in d) and e) as a function of analyte layer thickness are labeled. FOM of HPhPs in hBN on (f) dielectric ($Re(\varepsilon_s) > 0$) and (g) metallic ($Re(\varepsilon_s) < 0$) substrates with different loss tangents at 1438 cm^{-1}, based on the analytical solution. Mode is $l = 0$ for dielectric substrate and $l = 1$ for metallic substrate. The rate of change of ω with respect to $Re(\varepsilon_t)$ is plotted over incident frequency for (h) suspended or Si-supported hBN covered with analyte or (i) hBN surrounded by analyte

From the general trends, the FOM clearly decreases rapidly with increasing substrate dielectric constant, reaching a minimum at approximately $|\varepsilon_s| = 3$, and then increasing again. This effect is especially pronounced for the principal ($l = 0$) mode on dielectric substrates, as high-index substrates yield stronger confinement and longer propagation lengths. This contrasts with, and goes well beyond, prior results,[104] which showed only that FOM increased for suspended hBN compared to hBN on silicon. For metallic substrates, the effect is similar; however, the FOM is approximately symmetric about the minimum with respect to the dielectric response. Interestingly, this implies that when the substrate permittivity is close to the epsilon-near-zero (ENZ) condition rather than a metallic or dielectric value, the FOM for lossy substrates might actually be higher than that for a low-loss dielectric substrate.

For both dielectric and metallic substrates, the FOM of the higher-order modes is always improved with reference to the principal ($l = 0$ for dielectric, $l = 1$ for metallic) mode, though the trends with substrate permittivity are generally similar. Overall, the results of figure 4.17 c and d, indicate that the choice of substrate is a complicated issue for hyperbolic polaritons. While low-index substrates produce long-wavelength propagating modes, very high index substrates actually produce the highest FOMs for such polaritons. In the figure 4.18 we discuss the effect of the substrate loss tangent on the principal and higher-order modes.

Figure 4.18 f and g, illustrate the dependence of FOM on the substrate loss tangent, considering the same values of the loss tangent as in Figure 4.14. For loss-free dielectric substrates [$\mathrm{Im}(\varepsilon_s) = 0, Re(\varepsilon_s) > 0$], the FOM increases monotonically with $Re(\varepsilon_s)$. For lossy dielectrics, on the other hand, the FOM decreases to a minimum and then increases, asymptotically approaching a limiting value at high $Re(\varepsilon_s)$. For metallic substrates [$Re(\varepsilon_s) < 0$], the trend is similar to that for lossy dielectrics, except that in metallic substrates the low-$Re(\varepsilon_s)$ limiting value of FOM is higher than in dielectrics. As a result, for epsilon-near-zero (ENZ) materials, the FOM of hBN is higher on metallic substrates (despite their greater loss), due to the larger k (see Figure 4.17 c).

These results have significant implications for device designs based on HPhPs, in particular for both polariton refraction in planar metasurface-based optics[59, 118, 119] and hBN-based sensors. [120, 121] Previously we showed that HPhPs refract when propagating across a boundary between metallic and dielectric regions of a phase-change material. [59] The fact that each successively higher-order mode exhibits a smaller change in wavelength due to the changing dielectric environment promises the potential for spatial sorting of hyperbolic polaritons featuring different modal orders. To illustrate the potential for using the local dielectric function to control HPhP propagation, we consider a hypothetical device capable of spatially separating different mode orders by refraction at dielectric boundaries (figure 4.18a and b). The simulations are configured with a 120 nm thick hBN flake that is partly suspended and partly supported on a Si substrate. The HPhPs are launched from an array of dipole emitters above the suspended hBN, with the HPhPs propagating within the hBN towards the air-Si interface at a 45° angle of incidence. To suppress HPhP reflections from the simulated boundaries, we surrounded the region of interest by a border of highly lossy (20x increased damping) hBN. The *z*-component of the electric field

at a position 10 nm above the hBN surface is provided to demonstrate the varied refraction of $l = 0$ and higher-order modes leading to spatial separation (figure 4.18b). The HPhPs launched from the emitter array are refracted at the air-Si interface due to the wavevector mismatch across the boundary, but since the $l = 0$ mode is significantly more sensitive to the surrounding dielectric environment, it is more strongly refracted (transmitted angle 13, orange arrow) and is thus spatially separated from the $l = 1$ mode (transmitted angle 34°, green arrow). Therefore, using such approaches, high wavevector, higher-order HPhPs featuring increased spatial information could be spatially separated from the longer wavelength principal modes in a planar film.

To discuss the implications for index-based sensing,[122] where the change in frequency of polaritonic resonance indicates a change in the local dielectric environment, we consider the analytical model for both surface phonon polaritons (SPhPs) and HPhPs. At mid-IR frequencies, strongly confined HPhPs enabled the environmental sensitivity necessary to realize hBN enabled surface-enhanced infrared absorption (SEIRA)[121, 123] spectroscopy and suggested a basis for planar metaoptics structures [59] that have since been reduced to practice. [119] These new results also have implications for deploying hBN in thin-film sensing applications. Thin film sensing operates in two main regimes: index-based sensing (which relies on the change in local dielectric environment to change the mode frequency), or surface enhanced infrared absorption (SEIRA, which exploits local field enhancements). Our results are most obviously relevant in the field of the former, as they consider the properties of a substrate without significant spectral dispersion. As shown in figure 4.16 c, the presence of a nearby analyte significantly affects the properties of suspended hBN – resulting in a measurable shift in resonance frequencies. Thus, it is critical that

hBN be suspended or on a low-permittivity substrate to function as an effective index sensor (see figure 4.18 h and i).

To demonstrate how such a device could be realized, a device consisting of 120 nm thick hBN atop a 100 nm thick gold structure surrounding a resonant cavity filled with air or Si is simulated in figure 4.18c. Since HPhPs in hBN are sensitive to the surrounding dielectric environment, the resonant mode of this structure will be sensitive to the presence of an analyte on top of the hBN layer. Simulated reflectance spectra for an array of such resonators under far-field radiation incident at 45°, *p*-polarized light are provided in figure 4.18d and e, with the structure covered by a hypothetical analyte layer of $Re(\varepsilon)$=2.25 of variable thickness. For both air- and Si-filled resonators, sharp dips appear corresponding to resonant absorption in the cavity defined by the gold. These resonant frequencies are sensitive to as little as 1 nm of analyte placed on the hBN, demonstrating the high degree of sensitivity akin to efforts with SPhPs in SiC.[124] However, using suspended hBN significantly increases the magnitude of the observed shifts to well over 10cm^{-1}.

While these simulations suggest that hBN can act as a surface sensor, it is instructive to benchmark against other index-based sensing schemes. SPhP material operating with the same TO, LO and damping frequencies. Surprisingly, we find that for thick films of the analyte material ($>\lambda_{HPhP}$), the SPhP mode is much more effective as an index sensor. However, taking into account the strong confinement of HPhPs in hBN, we find that hyperbolic modes are indeed much more effective for sensing thin films, especially close to the LO phonon (where HPhP modes are extremely confined). This is reflected in the results of figure 4.18d, where the peak shifts are largest close to the LO phonon energy.

4.2.3 Conclusion

We have investigated the interaction of HPhP with substrates encompassing a wide range of complex refractive indices. While substrates with small real parts of the dielectric function support long-wavelength propagating modes, large permittivity substrates result in polaritons exhibiting the highest propagating FOMs. Furthermore, our results demonstrate that longer wavelength principal hyperbolic modes can be used as extremely sensitive subwavelength sensors. While all modes show an equal change in wavevector (Δk), the corresponding fractional change in wavevector $k(\varepsilon_{s1})/k(\varepsilon_{s2})$ for higher-order modes implies that they are less influenced by the local dielectric environment than the principal. Most significantly, the substrate permittivity can induce spatial mode separation of these higher-order modes. This effect could be used as a tool to optimize planar refractive optics and reconfigurable metasurfaces. Our results therefore provide a deeper understanding of HPhP interactions with the surrounding environment, a necessary step for implementing practical applications in on-chip molecular sensing and nanophotonics

4.2.4 Methods

4.2.4.1 Sample preparation.

For the purposes of these experiments, we employed isotopically pure hBN flakes (>99% $h^{10}BN$) to minimize the intrinsic polariton losses.[125] These were grown as described in reference,[126] then subsequently exfoliated and transferred onto the appropriate substrate. Single crystals of VO_2 were grown on quartz from vanadium pentoxide powder (V_2O_5) by physical vapor transport.[127] Due to the presence of multiple VO_2 crystals on the substrate we were able to suspend the hBN between adjacent VO_2 crystals. This resulted in flakes which were supported by VO_2 and quartz or

alternatively suspended between VO_2 crystals (as shown in figure 4.13). Silver films were deposited on Si substrates, while SiO_2 and Si substrates were obtained commercially.

4.2.4.2 s-SNOM.

In s-SNOM a platinum-coated probe tip is used both to map the topography and to probe the optical near fields. Monochromatic infrared near field imaging at selected laser excitation frequencies is performed via a combination of phase interferometric detection and demodulation of the detector signal at the second harmonic (2Ω) of the tip oscillation frequency.[23] The nano-FTIR data were acquired using a combination of s-SNOM and a broad-band infrared light source (neaspec.com).

.

CHAPTER 5

5. Spectroscopy and near-field microscopy of layered materials [3,4,5]

[3] Reprinted (adapted) with permission from {Alireza Fali, Sampath Gamage, Marquez Howard, Thomas. G. Folland, Nadeemullah A. Mahadik,Tom Tiwald, Kirill Bolotin, Joshua D. Caldwell, and Yohannes Abate, Accepted by ACS Photonics, Vol. 8 Issue 1 Pages 175-181 (2020)} Copyright {2020} American Chemical Society.

Reprinted here with permission of publisher

[4] Alireza Fali, Michael Snure, and Yohannes Abate, Accepted by Applied Physics Letter, Vol. 118, Issue 16, Pages 163105, (2021)

Reprinted here with permission of publisher

[5] Reprinted (adapted) with permission from {Alireza Fali, Tianyi Zhang, Jason Patrick Terry, Ethan Kahn, Kazunori Fujisawa, Bernd Kabius, Sandhaya Koirala, Yassamin Ghafouri, Da Zhou, Wenshen Song, Li Yang, Mauricio Terrones, and Yohannes Abate, Accepted by ACS Nano Vol. 15 Issue 2 Pages 2447-2457, (2021)} Copyright {2021} American Chemical Society.

Reprinted here with permission of publisher

5.1 Nanoscale spectroscopy of dielectric properties of Mica

This section is reprinted from{ Alireza Fali, Sampath Gamage, Marquez Howard, Thomas. G. Folland, Nadeemullah A. Mahadik,Tom Tiwald, Kirill Bolotin, Joshua D. Caldwell, and Yohannes Abate, Accepted by ACS Photonics, Vol. 8 Issue 1 Pages 175-181 (2020) Copyright {2020} American Chemical Society.}.Reprinted here with permission of publisher

5.1.1 Abstract

Infrared dielectric properties of muscovite mica, one of the first van der Waals crystals, exfoliated on silicon and SiO_2 substrates is studied using near-field nano-FTIR spectroscopy. The spectra of mica show strong thickness and wavelength dependence down to monolayer-scale with a prominent broad peak centered around ~1080 cm^{-1} assigned to stretching vibrations of Si-O. We reveal that the infrared dielectric permittivity of mica is anisotropic, i.e. has opposite signs along the in-plane and out-of-plane axis implying a Type I hyperbolic behavior in the range 920-1010 cm^{-1} and Type II hyperbolic behavior in the range 1050-1130 cm^{-1}. Experimentally measured nano-FTIR spectra agree well with analytical model calculations based on extended finite dipole model for layered systems of the tip-sample interaction when the out-of-plane dielectric values (instead of the in-plane dielectric values) were used in the calculations.

5.1.2 Introduction

Since the isolation of monolayer graphene, [128] numerous other layered materials have been identified. [129] These include, transition metal dichalcogenides (TMDs) with the general formula of MX_2, where M is a transition metal atom (e.g. M = Mo, W, Ta, etc.) and X is chalcogen (e.g. X = Se, S, Te) forming layers above and below M, hexagonal boron nitride and black phosphorous. In addition to providing a unique platform to discover exciting new physics, layered materials are

promising for applications in flexible optoelectronics. [130] While the list of metallic and semiconducting 2D crystals is growing by the day, the list of insulating 2D crystals is still limited. Muscovite mica, with the chemical formula $KAl_2(Al,Si_3)O_{10}(OH)_2$, is among the earliest known van der Waals (vdWs) materials that can be exfoliated in high-quality to large sizes (>1 cm^2) with atomic flatness. [131, 132] It can be prepared as a monolayer through the exfoliation of natural muscovite.[133, 134] The surface unit cell of bulk muscovite mica along the (001) crystal plane harbors two K+ ions, when exfoliated (along the (001) crystal face), only half the amount K+ ions per unit cell remain to preserve surface charge neutrality. The K+ ions are tightly locked in the interlayers resulting in stronger interlayer force in muscovite mica compared to the weak van der Waals forces between layers in most other 2D materials. On the other hand, the surface K+ ions exposed during exfoliation of muscovite mica allow unique opportunities for novel surface chemistry due to their ability to exchange with different cationic species and/or ease of functionalization. [135, 136] Because the surface is atomically flat, muscovite mica is an excellent substrate for materials used in optoelectronics such as vdWs flakes[134], self-assembled monolayers [137-140], light emitting devices [141, 142], and is used as a template to produce the active layer in organic solar cells.[143] However much of optical properties of monolayer to few layer mica remain unexplored.

In this work using a combination of mid-infrared scattering type scanning near-field microscopy (s-SNOM) and nano-FTIR, we perform near-field spectroscopy and imaging of 2D crystal muscovite mica down to the monolayer limit. Ellipsometry measurements enabled the extraction of the dielectric function in this spectral range, highlighting that the infrared dielectric permittivity of mica along the ordinary and extraordinary directions have opposite signs in the

920-1130 cm^{-1} range, thus, implying regions of both Type I and II hyperbolic behavior. The thickness- and wavelength-dependent IR spectra of muscovite mica exfoliated on either Si or SiO_2 substrates enabled sensitive detection the spectra of mica down to monolayer level taking advantage of the SiO_2 phonon polariton enhanced resonant excitation. The in-plane and out-of-plane dielectric values of mica extracted from ellipsometry measurements were used to perform model calculations. Good agreement of theoretical calculations with experimentally measured nano-FTIR spectra were achieved when the out-of-plane dielectric values from ellipsometry measurements were used. With reduced loss, mica could provide a robust hyperbolic material for large-scale nanophotonics applications.

5.1.3 Results sand discussion

The Mica sample was prepared by Dr. Bolotin's research lab at Freie Universität Berlin. Commercially available mica sample was used for this study. We performed X-ray diffraction (XRD) measurements on the sample using a Rigaku Smartlab x-ray diffractometer equipped with a 9kW Cu anode and collimating mirror producing Cu Kα quasi-parallel x-rays. Sample was mounted and aligned on an automated vertical goniometer, and diffraction spectra was collected using a 1d high sensitivity Si strip detector. XRD peak analysis and least squares refinement was performed to obtain lattice constants, phase orientation, and average grain sizes. The mica sample was found to crystallize in the hexagonal, Muscovite 3T phase with space group: P3112. The sample is highly c-plane oriented with 7 orders of (00,*l*) reflections observed in the XRD spectra. The spectra also show that the sample has high crystalline quality within the textured grains. The refined lattice parameters obtained were, a=5.1948±0.0045 Å, and c=29.9735±0.0001 Å. These XRD spectra and a table containing list of the observed peaks, along with the indices, the computed

peaks of the least squares refined structure and differences as well as further XRD analysis can be found in figure 5.1 a and table 5.1.

The XRD pattern of the muscovite mica sample is shown in figure 5.1 a This indicates the sample has high crystalline quality within the textured grains since several orders are observed and higher orders, especially the (00,24) peak has clearly separated $K\alpha_1$ and $K\alpha_2$ peaks. In addition, the (1,0,10), and (1,0,20) peaks were observed to be higher than what is expected from a powder sample. This suggests presence of some crystallites in the sample having this orientation. Several other minor peaks are observed, which arise from small fraction of crystallites having random orientation. Least squares refinement of all the peaks was performed to obtain the lattice constants and associated errors. Table 5.1 has a list of the observed peaks, along with the indices, the computed peaks of the least squares refined structure and differences. The mean squared variation of 18 peaks was 0.0412 degrees, which indicates a well refined lattice structure. The refined lattice parameters obtained were, a=5.1948±0.0045 Å, and c=29.9735±0.0001 Å. Using the Scherrer analysis, average size of the (00,l) oriented grains was calculated to be 60 nm. The average size of the (1,0,10)/(1,0,20) was 120 nm.

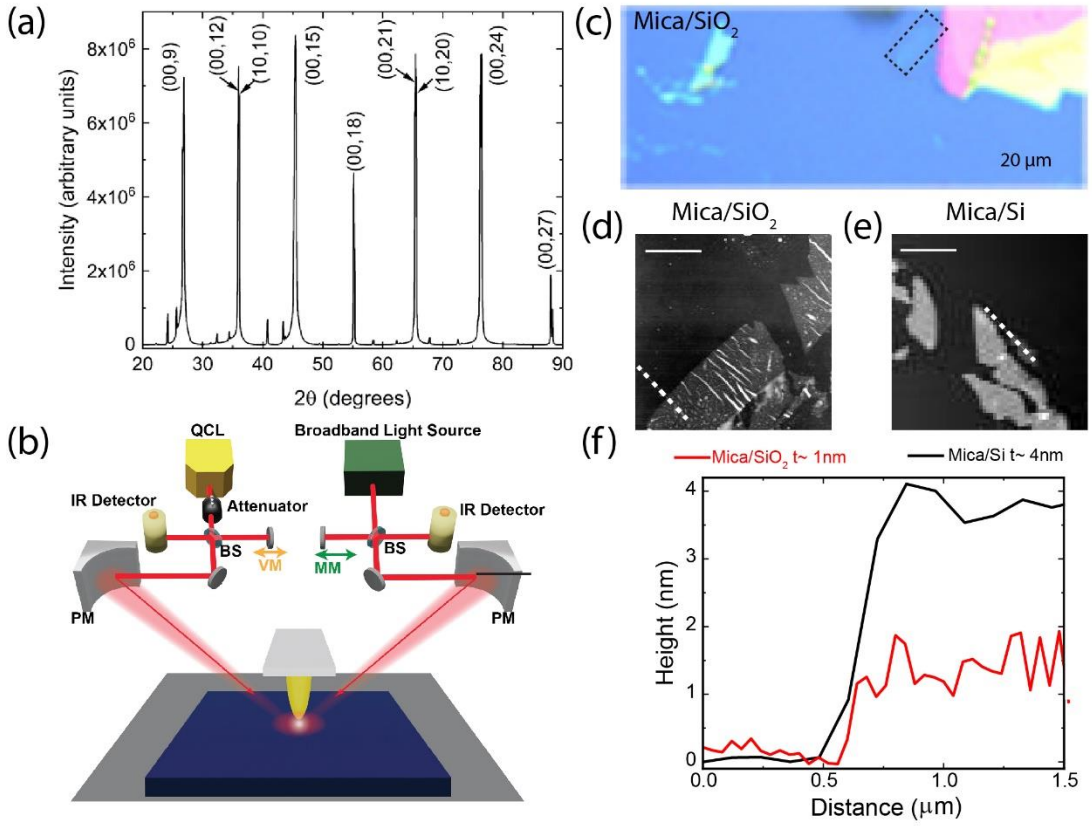

Figure 5.1 Optical micrograph and AFM topography images of exfoliated muscovite mica flakes. (a) XRD pattern of the mica sample showing 7 orders of the (00l) orientation, indicating a highly c-axis oriented sample. Other small peaks are observed from the presence of small fraction of randomly oriented grains within the sample. (b) Schematics of the nano-FTIR setup. (c) Optical image of exfoliated mica on SiO_2, Topography and of 4 nm thick mica on Si (d) and 1 nm thick mica on SiO_2 (e) and corresponding height line profiles (f). Scale bar in c &d is 1µm

Table 5.1. Peaks observed in the XRD pattern, which were indexed, and the calculated peaks of the least squares refined lattice structure. The mean squared deviation was very low of 0.0412 degrees.

h	k	l	$2\theta_{observed}$ (degrees)	$2\theta_{calculated}$ (degrees)	Difference
1	0	6	26.654	26.6648	-0.0108
0	0	9	26.800	26.7678	0.0322
1	1	1	34.686	34.6642	0.0218
0	0	12	35.976	35.9537	0.0223
1	0	10	36.090	36.0039	0.0861
0	0	15	45.390	45.3856	0.0044
2	0	7	45.533	45.5513	-0.0183
2	0	11	52.680	52.7699	-0.0899
0	0	18	55.151	55.1551	-0.0041
2	1	7	58.390	58.3928	-0.0028
1	0	19	62.348	62.3751	-0.0271
2	1	10	62.850	62.8307	0.0193
0	0	21	65.373	65.3818	-0.0088
1	0	20	65.577	65.6641	-0.0871
1	0	22	72.530	72.485	0.045
2	2	2	73.160	73.1422	0.0178
0	0	24	76.270	76.2333	0.0367

0	0	27	87.974	87.9625	0.0115

A combination of s-SNOM and nano-FTIR is used to acquire topography, near-field images and IR nano-spectra on muscovite mica sample prepared by mechanical exfoliation on either Si or SiO_2 substrates. The experimental setup ((Figure 5.1b, neaspec co.) is based on a tapping mode AFM with a cantilevered metal-coated tip that oscillates at a resonance frequency, W~280 kHz and tapping amplitude of ~50 nm. Either a coherent broadband infrared beam in the frequency range 700-2100 cm^{-1} (for nano-FTIR) or a monochromatic IR laser (for s-SNOM) is focused by a parabolic mirror to the tip. For nano-FTIR operation, the backscattered near-field light from the tip-sample junction is detected via mixing with an asymmetric Fourier transform Michelson interferometer. This detection method enables recording of both the amplitude $\mathbf{s}(\omega)$ and phase $\phi(\omega)$ spectra of the backscattered light. To extract background free local near-fields, the detector signal is demodulated at a higher harmonic $n\Omega$ of the tip mechanical resonance frequency Ω. Normalized amplitude (s_n(sample)/s_n(reference)) and phase (j_n(sample)-j_n(reference)) IR near-field spectra are acquired by first taking reference spectrum on a reference area (silicon is used in these experiments), followed by taking spectra at desired positions of the sample. Figure 5.1 c show a representative optical micrograph of mica flakes exfoliated onto a SiO_2 substrate, the rectangular box in black broken lines subtends a monolayer flake. Figure 5.1b &c show AFM topography images of mica flakes on SiO_2 and Si respectively. Red and black lines in figure 5.1f are corresponding line profiles taken on dashed lines on Si substrate (black line) and SiO_2 substrate (red). While we could exfoliate a monolayer (height ~1nm) flake on SiO_2

substrate[134], the thinnest flake we could exfoliate on Si had a height of ~4nm.

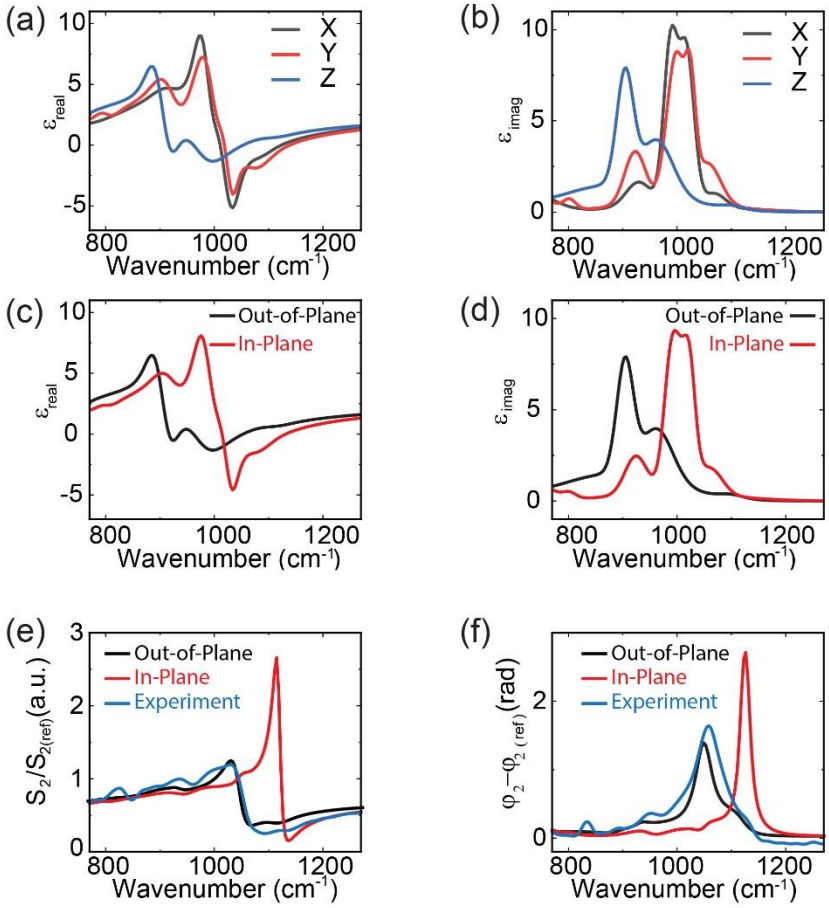

Figure 5.2 Ellipsometry and nano-FTIR spectra of muscovite mica. Mid infrared dielectric function extracted from far-field ellipsometry measurements of muscovite mica. (a) Real and (b) imaginary part of the permittivity of Mica for X and Y axes.Real (c) and imaginary (d) part of the permittivity of the in-plane (red curves) and out-of-plane (black) components as a function of excitation frequency are provided. Extended finite dipole model calculation of near-field amplitude S_2 (e), and phase φ_2 (f) spectra performed by using the in-plane (red curves) and out-of-plane (black curves) permittivity. Nano-FTIR experimental spectrum taken on 40 nm mica flake on Si substrate is shown in blue in (e) and (f) for comparison.

The dielectric function of muscovite mica at mid-IR frequencies is necessary to understand its spectroscopic response, yet has not been reported previously. Thus we performed ellipsometry measurements in the mid-IR frequency range, using an IR-VASE ellipsometer (J. A. Woollam Co., Lincoln NE). The substrate was mounted on a precision rotation stage, and a data set was acquired after the substrate was rotated to 5 different rotational positions around the sample normal – 0°

(initial position), 45°, 90°, 135° and 180°. Each data set included of data at incident angles of 45°, 60° and 75°. All data sets were acquired at a spectral resolution of 8 cm^{-1}. After the measurement, the data were fit to a biaxial substrate model using standard numerical analysis methods similar to those described by Jellison [144-146] and Herzinger[147]. Figure 5.2 a-d show the real and imaginary parts of the dielectric functions, respectively, extracted from ellipsometry along the in-plane and out-of-plane directions (with respect to the sample plane). To produce the in-plane component of the dielectric function, we averaged the dielectric data for the in-plane X and Y-axis values. This is because the difference between the X and Y-axes dielectric data is insignificant (Figure 5.2a&b) owing to polycrystalline (with z-axis aligned) nature of the sample. The real and imaginary permittivity values plotted in Figure 5.2 c&d for the in-plane (ε_I, red curve) and out-of-plane (ε_z, black curve) components clearly display anisotropy. Notably, $Re(\varepsilon_z) < 0$, $Re(\varepsilon_I) > 0$ in the frequency range 920-1010 cm^{-1} (excluding the range 930-955 cm^{-1}) and $Re(\varepsilon_I) < 0$, $Re(\varepsilon_z) > 0$ in the frequency range 1050-1130 cm^{-1}. This implies that mica is a hyperbolic material (Type I in the range 920-1010 cm^{-1} and Type II in the range 1050-1130 cm^{-1}), this is because the in-plane and out-of-plane components of its dielectric permittivity have opposite signs in these frequency ranges. This behavior adds mica to the list of natural hyperbolic materials in the infrared. [148-150] The imaginary parts of the permittivity curves shown in Figure 5.2 d represent dissipation of optical energy accompanying this anomalous optical hyperbolic behavior. These imaginary parts are relatively small in comparison with highly lossy metallic plasmonic materials, but are a factor of 271 at 800 cm^{-1} (Mica $Im(\varepsilon_z)$/ hBN $Im(\varepsilon_z)$) and a factor of 32 at 1075 cm^{-1} (Mica $Im(\varepsilon_z)$/ hBN $Im(\varepsilon_z)$) times larger compared to hBN, another exfoliable hyperbolic material in the infrared. [151, 152] We note that the real part of permittivity ratio of mica to hBN is much smaller than the

imaginary part ratio (0.38 at 800 cm^{-1} (Mica Re(ε_z)/ hBN Re(ε_z)) and a factor of 0.04 at 1075 cm^{-1} (Mica Re(ε_z)/ hBN Re(ε_z)) which implies an overdamped system. These experimentally acquired real and imaginary dielectric functions will be used to elucidate near-field spectra and hyperbolic response of mica, the role of thickness and substrate.

When the out-of-plane dielectric function is used in the extended finite dipole model, the calculated spectra fit experimental nano-FTIR spectra very well. This evident in Figure 5.2 e and f where the nano-FTIR experimental spectra (blue line) are compared with tip-sample near-field interaction analytical model calculations using the in-plane (red line) and out-of-plane (black line) dielectric data from Figure 5.2 c & d. The normalized near-field nano-FTIR amplitude (figure 5.2 e) and phase (figure 5.2 f) spectra, were acquired by taking broadband spectra on a 40 nm mica flake and normalized them to a spectra taken at a reference point on the Si substrate surface. [28, 45] The calculations were performed by modeling the tip-sample near-field interaction based on a multilayer finite dipole model[47] in which the tip is approximated as an ellipsoid of length of 600 nm and 30 nm apex radius. The tip is illuminated by the infrared beam at an angle of 30^0 relative to the sample plane and the scattered signal is collected by the detector, providing amplitude and phase spectra, $s_n(\omega)$ and $\phi_n(\omega)$[48] via higher-harmonic signal demodulation. The details of the model are presented in the methods section and in Ref. [44-47]. The n^{th} harmonic of the electric field component of the scattered light is written as $E_n = S_n e^{i\varphi_n} \propto (1 + r_p)^2 \alpha_{eff}(\beta) E_{inc}$, where r_p is the far-field Fresnel reflection coefficient of the sample[48], the incident electric field and $\alpha_{eff}(\beta)$ the effective polarizability,[46] which contains the near-field interaction between tip and sample. The quasi-static near-field reflection coefficient, β is a function of the frequency-dependent dielectric function $\varepsilon(\omega)$ of the sample (see Methods for equation for β with multilayer

model). It is clear from figure 5.2 e & f that only when the out-of-plane axis dielectric data are used in the calculation that we reproduce the experimental near-field nano-FTIR amplitude and phase spectra. The experimental spectra shown in blue solid lines, amplitude (figure 5.2 e) and phase (figure 5.2 f), fit reasonably well with the extended finite dipole model calculations that uses the out-of-plane dielectric data as shown in black solid lines. The model calculations performed using the in-plane dielectric function (red solid lines in figure 5.2 e-f) significantly deviate from the experimental spectra. This is because light focused on the metalized tip is mainly enhanced along the tip-axis, perpendicular to the sample surface, and probes the sample largely in the out-of-plane direction, which is then scattered by the tip and detected. The small deviation of the theoretical phase spectra from the experiment (figure 5.2f) may be due to the tip probing both components (in-plane and out-of-plain) in some proportion instead of exclusively the out-of-plane component as assumed in the calculation.

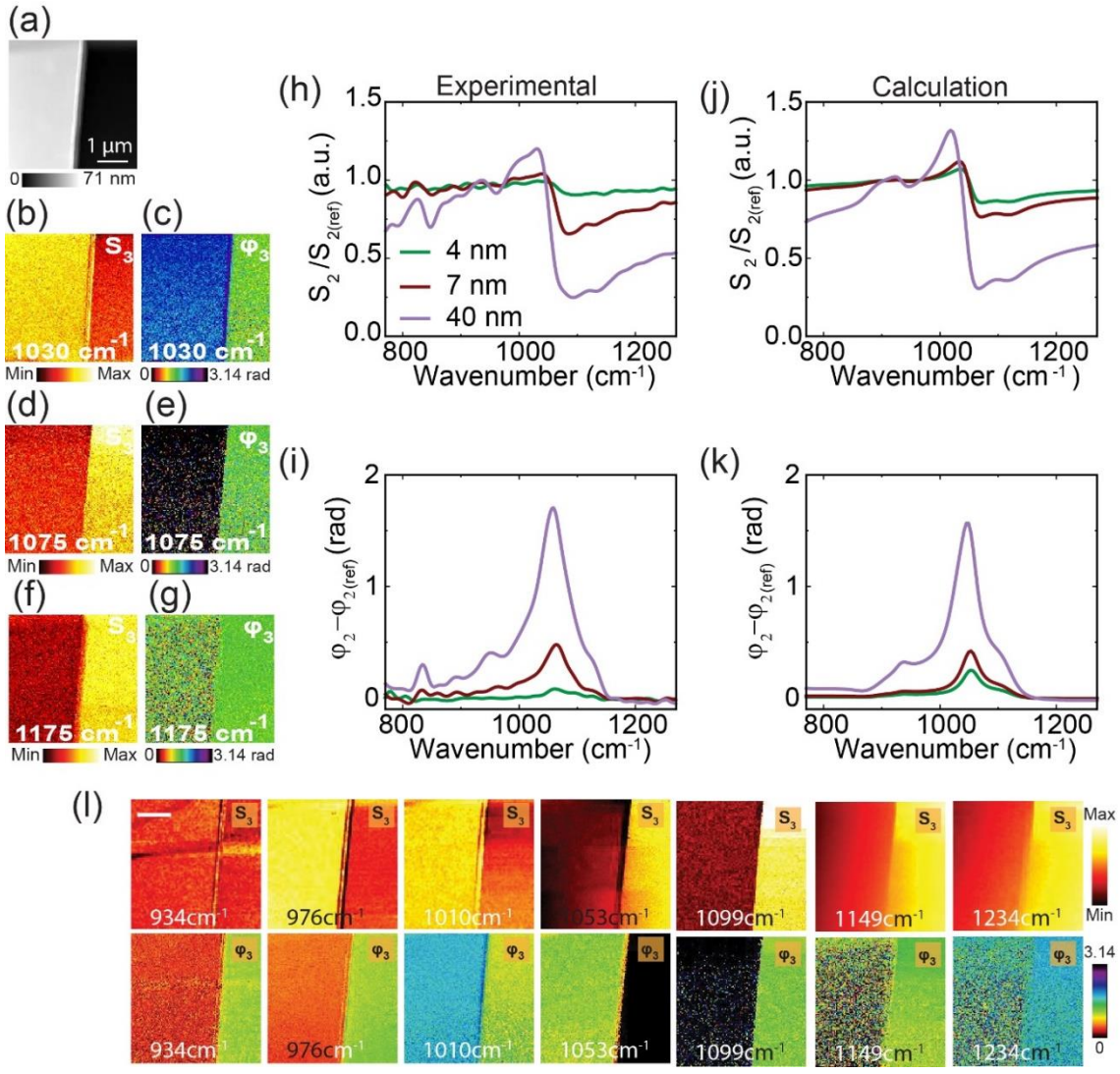

Figure 5.3 s-SNOM images and nano-FTIR of mica on Si substrate. (a-g) Topography, third harmonic near-field amplitude and phase images at three different frequencies of 55 nm Mica flake on Si. Near-field experimental nano-FTIR amplitude S_2 (h), and phase φ_2 (i) spectra at different thickness. Calculated nano-FTIR amplitude S_2 (j), and phase φ_2 (k) spectra, respectively. (l) Third harmonic near-field amplitude (S_3) and phase(φ_3) images of Mica /Si flake shown at various frequencies.

In Figure 5.3a we show representative images of topography and monochromatic s-SNOM amplitude (b, d, & f) and corresponding phase (c, e, & g) images of muscovite mica exfoliated on Si substrate taken at three selected excitation laser frequencies (1030 cm^{-1}, 1075 cm^{-1} and 1175 cm^{-1}). Additional monochromatic images at several other excitation frequencies are shown in Figure 5.3 l. The excitation frequency 1075 cm^{-1} is of particular interest since it is in the hyperbolic

polaritonic range (1050-1130 cm^{-1}) of mica. However, the amplitude/phase images do not display the characteristic interference fringes that are the hallmark of polaritonic propagating modes. We attribute this lack of propagating modes to large losses[58]. The amplitude contrast between mica and Si is inverted at 1030 cm^{-1} due to the large negative Re(ε_1) that enables the normalized amplitude of mica to be larger than unity, whereas wavenumber at 1030 cm^{-1} and larger give mica amplitude contrasts smaller than unity resulting darker profiles than the surrounding Si. To un derstand the full wavelength and thickness dependent IR optical characteristics, we took nano-FTIR spectra on varying thickness flakes of muscovite mica (thickness ~4nm, 7 nm and 40 nm) on a Si substrate. Silicon is a choice substrate for this purpose, since its spectra is featureless in the mid IR spectral region. In figure 5.3 h&i we show the experimental normalized amplitude and phase spectra respectively. Experimentally, these spectra were obtained by normalizing the broadband spectra taken on the mica flake to spectra collected from a reference point on the Si substrate surface.[28, 45] The calculation results shown in figures 5.3 j&k were performed using the extended finite dipole model calculation in which the out-of-plane dielectric function of mica extracted from ellipsometry measurements (as described above) were used to achieve the near-field amplitude and phase spectra of varying thickness muscovite mica exfoliated on Si substrate in the frequency range 750 -1300 cm^{-1}. Both the experimental amplitude and phase spectra show similar appearances for different layer thickness, however the signal level becomes progressively smaller with decreasing thickness due to smaller probed volume. The phase spectra show a prominent broad peak around ~1080 cm^{-1}. The calculations reproduce the essential features of the experimental amplitude and phase spectra in peak positions and displays thickness dependence signal intensity similar to experimental observations. The broad, strong band between 980-1200

cm^{-1} centered around ~1080 cm^{-1} is due to stretching vibrations of Si-O, which is in better agreement with several reported data [153-155]. The shoulder at 831 cm^{-1} is due to the stretching Al-O mode, whereas the band near 920 cm^{-1} is tentatively assigned as a mixed modes arising from Al-OH stretch, Al-O-Al vibration, Si-O-Si and Si-O-Al stretching vibrational modes [153-157].

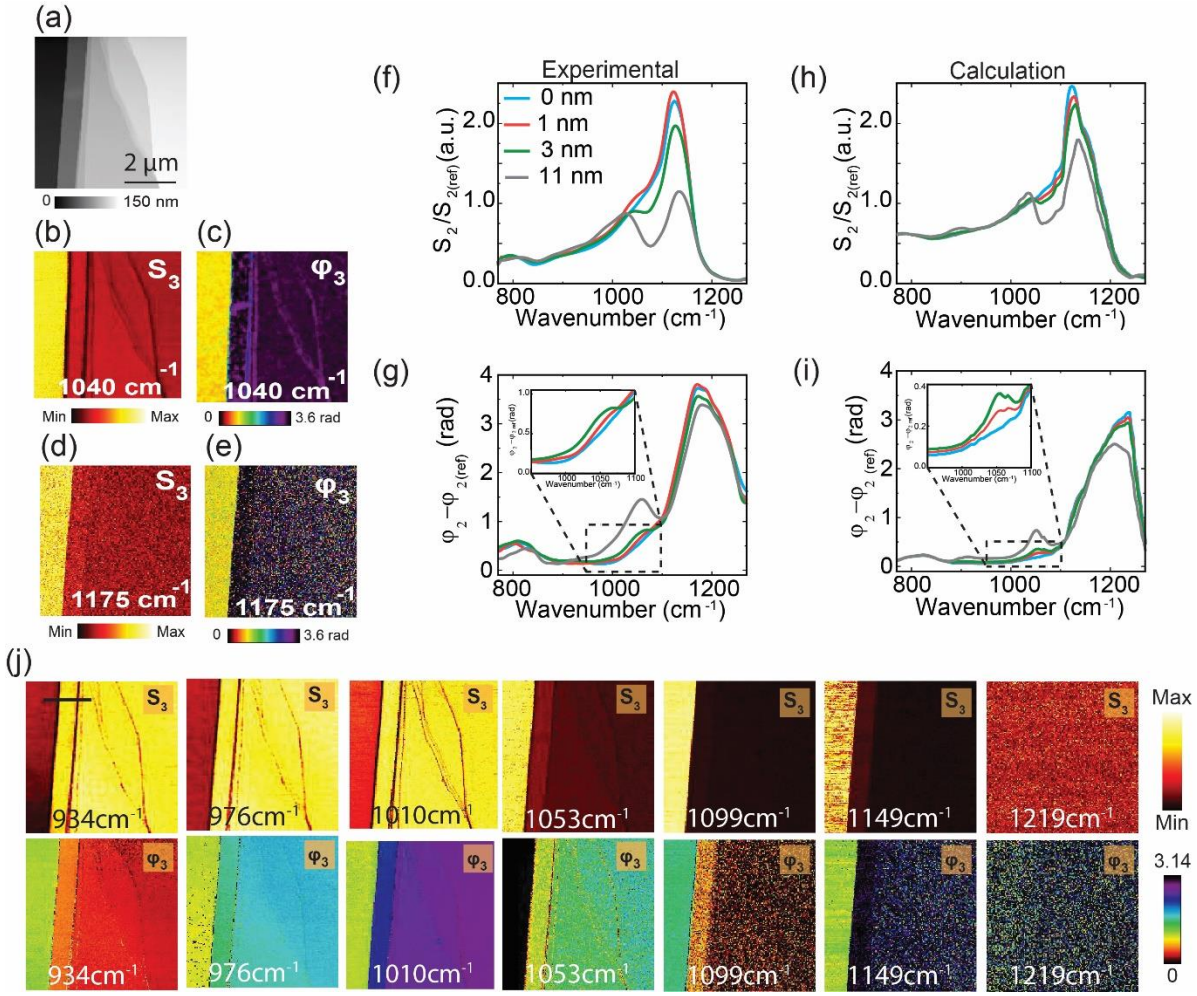

Figure 5.4 s-SNOM images and nano-FTIR of mica on SiO_2 substrate. (a) Topography image of Mica flake. (b-e) Third harmonic near-field amplitude and phase images of the flake in (a) at 2 different frequencies. Near field experimental nano-FTIR amplitude S_2 (f), and phase φ_2 (g) spectra at different thicknesses. Calculated nano-FTIR amplitude S_2 (h), and phase φ_2 (i) spectra, respectively. Insetets in (g) and (i) are zoomed in near field experimental nano-FTIR phase φ_2 and calculated nano-FTIR phase $\varphi_2$respectively (j)Third harmonic near-field amplitude (S_3) and phase(φ_3) images of Mica/SiO2/Si flake shown at various frequencies.

We took infrared nano-FTIR spectra of various thickness heterostructures of muscovite

mica exfoliated on SiO_2. We chose SiO_2 as a supporting substrate because of its strong phonon resonance absorption peak that partially overlaps with mica that may enable phonon polariton enhanced IR spectroscopy. In addition, unlike Si, SiO_2 substrate enables facile exfoliation of thin layers of mica down to a monolayer. To investigate the property of hyperbolic modes in mica exfoliated on SiO_2, we took topography (Figure 5.4a) and near-field amplitude (Figure 5.4.b & d) and corresponding phase (Figure 5.4 c & e) images at two excitation laser frequencies (1040 cm^{-1}, and 1175 cm^{-1}). We did not observe propagating modes, however we observed enhanced polaritonic signature in the near-field images taken at the hyperbolic spectral range (~920-1130 cm^{-1}). For example, as shown in Figure 5.4b, the amplitude and phase images taken at 1040 cm^{-1} show enhanced signal at the topographic steps at different heights whereas such signatures are lost at 1175 cm^{-1}, which is outside the hyperbolic range (see Figure 5.4 j for more monochromatic images at other excitation frequencies). Similar to the discussion following Figure 5.3, the absence of clear propagating modes here is also attributed to weak polaritonic behavior of mica and large losses. In Figure 5.4f and Figure 5.4g we show the experimental amplitude and phase spectra of exfoliated mica down to a monolayer on SiO_2 substrate taken in the IR range (750-1280 cm^{-1}). The heterostructure spectra intensity significantly depends on the thickness of the mica layer. As the thickness of the mica decreases, the signal level for all the spectra features arising from the top mica layer (discussed above) progressively decrease while the known broad peak of SiO_2 centered around ~1180 cm^{-1} in the phase spectra) increases in intensity. We observe spectral signature of a monolayer thickness. This is evident when comparing the blue and red curve in Figure 5.4g, the weak shoulder at 1080 cm^{-1} is a clear indication of absorption coming from ~1 nm thick mica (see inset in figure 5.4 g and i zoomed in plots of the phase spectra for 0, 1 nm and 3 nm for better

comparison). This is because of substrate-enhanced absorption due to the combined polaritonic behavior of both mica and SiO_2 in these IR frequency ranges. Furthermore, for Mica flake as thick as 310 nm we see through it a signature of SiO_2 spectral signature (see Figure 5.5) possibly due to polaritonic behavior of both mica and SiO_2. These experimental trends are reproduced faithfully in intensity changes with thickness and peak positions by the extended finite dipole model calculations (Figure 5.4h & i) performed using the dielectric function of muscovite mica (as described above) and of SiO_2 from literature.[158]

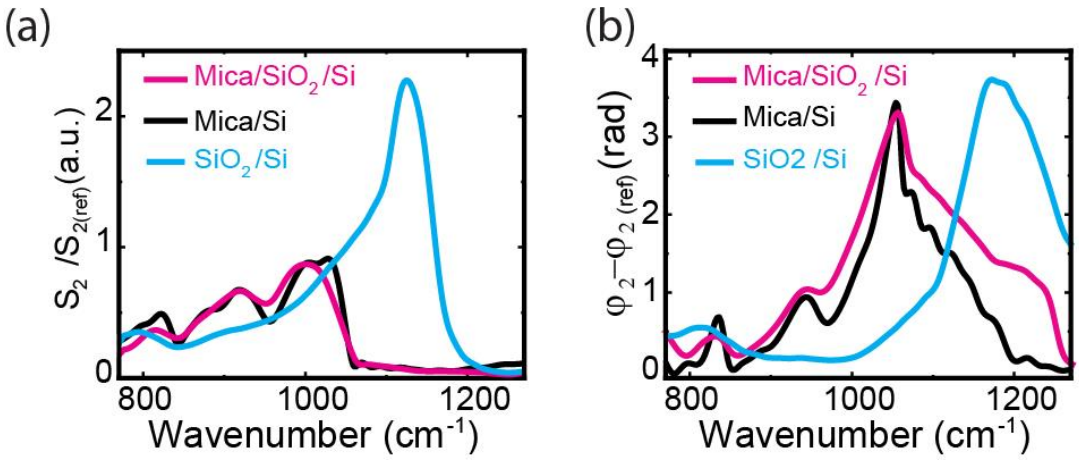

Figure 5.5 Comparison of Near-field experimental spectra of mica on various substrates. Near-field experimental nano-FTIR amplitude S_2 (a), and phase φ_2(b), spectra of Mica/SiO_2/Si (red) and Mica/Si (black) and SiO_2/Si (blue). Thickness of Mica for both substrates is 310 nm.

5.1.4 Conclusion

We investigated the infrared optical properties of muscovite monolayer to multilayer mica by a combination of ellipsometry and s-SNOM/nano-FTIR experimental measurements and analytical calculations based on extended finite dipole method. The dielectric function of muscovite mica in the mid IR frequencies, were extracted from ellipsometry measurements along the in-plane and out-of-plane axis (with respect to the sample plane). These measurements show

that mica is hyperbolic material having the in-plane and out-of-plane components of its dielectric permittivity opposite signs in the IR frequency range 920-1130 cm^{-1} displaying weak Type I and Type II hyperbolic behavior. Near-field nano-imaging experiments did not find interference fringes of propagating modes expected from polaritonic medium, which may be due weak polaritonic behavior of mica and large losses. The extended finite dipole model calculations reproduce the essential features of the experimental amplitude and phase spectra in peak positions and thickness dependence signal intensity when the out-of-plane axis dielectric data is used in the calculations. The prominent broad peak in the phase spectra centered around ~1080 cm^{-1} is assigned to stretching vibrations of Si-O and the shoulder peak at 831 cm^{-1} is due to the stretching Al-O mode, the band near 920 cm^{-1} is tentatively assigned as a mixed modes arising from Al-OH stretch, Al-O-Al, Si-O-Si and Si-O-Al stretching vibrational modes.

5.1.5 Methods

5.1.5.1 Extended finite dipole model for layered systems

The theoretical approach is based on the finite dipole model and its extension to layered system in which amplitude (S_n) and phase (ϕ_n) calculated by scattered emission:

$$E_n = S_n e^{(i\varphi_n)} \propto \left(1 + r_p\right)^2 \alpha_{eff} E_{inc} \tag{5-1}$$

In equations (5-1) for mica flake on SiO_2 on Si r_p is the reflection coefficient for four layers (layer 1 is surrounding medium, layer 2 mica with thickness d_1, layer 3 SiO_2 with thickness d_2 and layer 4 is Si) that can calculated from multilayer Fresnel reflection coefficient for p-polarized light given by: [50, 51]

$$r_p(q,\omega) = \frac{r_{12} + r_a \exp\left(2ik_z(d_1+d_2)\right)}{1 + r_b \exp\left(2ik_z(d_1+d_2)\right)} \tag{5-2}$$

Where r_a and r_b can be calculated as:

$$r_a = r_{12}r_{23}r_{34}\exp(-2ik_z d_1) + r_{23}\exp(-2ik_z d_2) + r_{34} \quad (5\text{-}3)$$

$$r_b = r_{23}r_{34}\exp(-2ik_z d_1) + r_{12}r_{23}\exp(-2ik_z d_2) + r_{12}r_{34} \quad (5\text{-}4)$$

r_{ij} is single interface Fresnel reflection coefficient: [51]

$$r_{ij} = \frac{\varepsilon_j k_{z,i} - \varepsilon_i k_{z,j}}{\varepsilon_j k_{z,i} + \varepsilon_i k_{z,j}} \quad (5\text{-}5)$$

Where $k_{z,i} = \sqrt{\varepsilon_i(\omega/c)^2 - q^2}$. [52] In equation (5-1), α_{eff} is effective polarizability. Equations (6-15) gives us the effective polarizability which described in reference [46] . L is effective length of tip, R_t is tip curvature radius which is 20 nm, C is the height-independent constant with $Q_0 = R_t^2 E_0$ which is the total amount of the polarization charge induced in tip in the absence of sample which is described in reference [47] , H is tip and sample distance.

$$\alpha_{eff} = C\left(1 + \frac{1}{2}\frac{f_0(H)\beta(\varepsilon)}{1 - f(H)\beta(\varepsilon)}\right) \quad (5\text{-}6)$$

$$f_0(H) = \left(g - \frac{2H + W_0 + R_t}{2L}\right)\frac{ln\frac{4L}{4H + 2W_0 + R_t}}{ln\frac{4L}{R_t}} \quad (5\text{-}7)$$

$$f(H) = \left(g - \frac{2H + W_i + R_t}{2L}\right)\frac{ln\frac{4L}{4H + 2R_t}}{ln\frac{4L}{R_t}} \quad (5\text{-}8)$$

$$C = L\frac{Q_0}{|E_0|} \quad (5\text{-}9)$$

$$W_0 \approx 1.31R_t L/(L + 2R_t) \quad (5\text{-}10)$$

$$W_i \approx R_t/2 \quad (5\text{-}11)$$

Where β is quasi-static near-field reflection coefficient given by: [50]

$$\beta = \frac{\beta_{12} + \beta_a \exp(-2q(d_1 + d_2))}{1 + \beta_b \exp(-2q(d_1 + d_2))} \quad (5\text{-}12)$$

Where β_a and β_b can defined as:

$$\beta_a = \beta_{12}\beta_{23}\beta_{34}\exp(2qd_1) + \beta_{23}\exp(2qd_2) + \beta_{34} \quad (5\text{-}13)$$

$$\beta_b = \beta_{23}\beta_{34}\exp(2qd_1) + \beta_{12}\beta_{23}\exp(2qd_2) + \beta_{12}\beta_{34} \quad (5\text{-}14)$$

The electrostatic reflection coefficient β_{ij} is defined by: [50]

$$\beta_{ij} = \frac{\varepsilon_j - \varepsilon_i}{\varepsilon_j + \varepsilon_i} \quad (5\text{-}15)$$

5.2 Violet phosphorus surface chemical degradation in comparison to black phosphorus

This section is reprinted from{ Alireza Fali, Michael Snure, and Yohannes Abate, Accepted by Applied Physics Letter, Vol. 118, Issue 16, Pages 163105, (2021)}. Reprinted here with permission of publisher

5.2.1 Abstract

Bulk growth methods have made it possible to synthesize several allotropes of phosphorus such as black, white, red, and violet phosphorus. However, unlike exfoliated black phosphorus (BP), which has been extensively studied, much of the optoelectronic properties and stability of the other allotropes have yet to be comprehensively investigated. Here, we study the chemical degradation of exfoliated violet phosphorus (VP) in comparison to BP under ambient conditions using nanoscale infrared spectroscopy and imaging. We identify oxidized phosphorus species that result from chemical reaction processes on the surfaces of these phosphorus allotropes. We have found that VP exhibits a noticeably different and slower degradation process when compared to BP establishing it as the more stable of the two allotropes. A better understanding of the stability

of VP could lead to the further fundamental study of its monolayer form for potential future applications.

5.2.2 Introduction

Black phosphorus (BP) has been synthesized for over 100 years, [159] but the interest in BP in contemporary materials research accelerated due to its exfoliable nature, which makes it a member of the van der Waals materials (vdW) family. BP's orthorhombic crystal structure with space group Cmca, is anisotropic in-plane displaying two independent in-plane components of the dielectric tensor that are different from each other. [160] The band gap of BP is tunable, direct, and narrow making it suitable for nanoelectronics and nanophotonics applications. [161] It also displays thickness dependent on/off current ratio in the range of 10^3–10^5 and decent saturation characteristics that makes it a candidate for digital logic applications in thin film electronics as well as flexible electronics. [162] In addition to BP, there are two other layered allotropes of phosphorus, violet, and blue. These allotropes, which are all p-type, have distinct structures and band gaps ranging from narrow BP (0.3 eV) [163] to mid band gap violet phosphorus (VP) (1.7 eV) [164] and blue phosphorus (2 eV). [165]

vdW heterostructures based on BP have presented great opportunities for application in nanoelectronics. [166] For instance, the Schottky barrier height and doping of BP can be controlled by electrostatic gating in graphene/BP heterostructures, and BP/MoS_2 p-n junctions show strong gate-tunable current-rectifying I-V characteristics. [167] With multiple layered allotropes, phosphorus offers the unique opportunity to form 2D heterostructures using this single element. Recently, the work function and band gap of VP were investigated showing an increasing work function from 4.79 to 5.17 eV with decreasing number of layers from bulk, while the band gap

increases from 1.7 to ~2eV.[164] Coupled with the thickness tunable band gap (0.3-1.5eV) [168] and work function (4.56 to 5.17 eV) of BP, this suggests both type I and type II heterostructures may be possible with BP/VP via thickness tuning. Experimentally, heterostructures of BP/VP have been observed during chemical vapor transport (CVT) synthesis [169] and by annealing BP flakes in tertiarybutylphosphine (TBP).

Oxidation and degradation of BP films remain a considerable challenge affecting charge impurities in the surface and substrate environment resulting in scattering centers that can significantly reduce the carrier mobility. Researchers have been endeavoring to accelerate the use of BP by overcoming the formidable challenge of preserving thin BP from oxidation. [162] In addition to ongoing efforts to find ways to stabilize BP, the search for other more stable phosphorus allotropes as well as phosphorous based heterostructures are underway. A recent example is the successful exfoliation of violet phosphorene from bulk VP crystals grown by CVT [164, 170] Although BP has been largely reported as the most stable phosphorus allotrope, Zhang et al. [164] recently reported VP to be thermally stable to 512 °C compared to 460°C for BP. However, much of VP's ambient stability in comparison to BP remains unknown.

5.2.3 Results

In this work, we investigate the surface chemical degradation of exfoliated VP flakes and compare its surface oxidation with BP samples under ambient conditions over time. We performed nanoscale infrared spectroscopy (nano-FTIR) in the frequency range 800-1500 cm^{-1} by mapping the local ambient spectral changes at nanometer spatial resolution. The nano-FTIR spectra taken on VP and BP flakes show broad spectra arising from several overlapping vibrational modes from phosphoric species produced due to degradation. The topography and surface degradation

evolution of VP flakes are different from surface and height changes observed on BP flakes. VP shows more stability than BP as revealed by the surface topographic and dielectric changes on the surface over time. In BP, the degradation begins at random locations as bubbles then evolves abruptly over a large area via the connection of local bubbles towards saturation following a sigmoid growth curve. The degradation effects we observe in VP through topography and nano-FTIR spectra are noticeably different from BP, which highlight differences in the degradation process of these two phosphorus allotropes. Additionally, we identify the formation of VP on BPs flakes during annealing under TBP demonstrating the possibility of forming VP/BP heterostructures. The 2D phosphorous semiconductor allotrope family spans a wide range of optoelectronic properties; their combination would allow the unique opportunity to build a single-element vdW heterostructure.

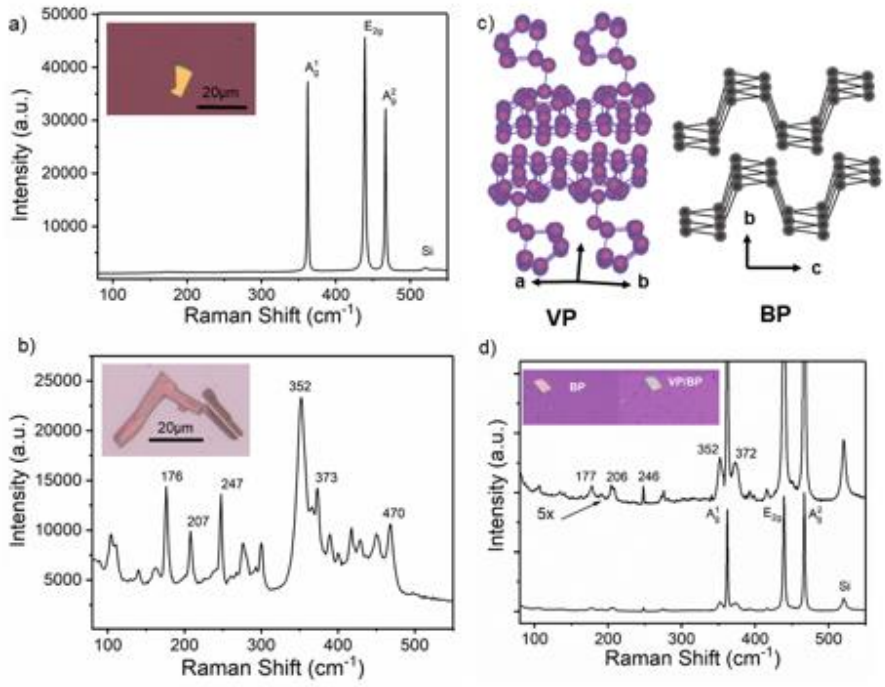

Figure 5.6 Raman characterization of BP, VP, and, heterostructure. a) Raman spectrum of a ~ 65 nm thick BP flake on SiO_2/Si substrate. Inset shows optical image of BP flake. b) Raman spectrum of a ~430 nm thick VP flake on

SiO_2/Si. Inset shows optical image of as-grown VP flakes. c) Schematic comparing the structures of VP and BP. d) Raman spectra of VP/BP heterostructure. Top curve is magnified by 5x to show VP portion of the spectrum. Inset shows optical image of transferred BP flake and the same flake after formation of VP/BP.

For this study we used bulk VP and BP fabricated by Michael Snure at AFRL.Flakes of BP and VP were transferred from bulk sources onto SiO_2/Si for characterization. Bulk BP produced by CVT was purchased from 2D Semiconductors and bulk VP was produced in-house by chemical vapor deposition (CVD). For VP synthesis, a quartz crucible was loaded into the CVD chamber filled with 0.1g SnI_4 and 0.1g Sn metal and covered with a sapphire wafer, evacuated, and filled with N_2:H_2 (95%:5%) to a pressure of 700 Torr. Then, the reactor was heated to 600 °C, and the phosphorus source TBP was flowed at a flow rate of 40 sccm with 160 sccm of N_2:H_2 for 30min. The reactor was then cooled to 400 °C under flowing TBP and N_2:H_2. After reaching 400 °C, TBP was turned off and the reactor cooled to room temperature. Small flakes of VP that formed on the edges of the crucible and sapphire wafer were transferred to SiO_2/Si for characterization using a polydimethylsiloxane (PDMS) stamp. For VP/BP samples, BP flakes were exfoliated on to a SiO_2/Si substrate, loaded into the CVD chamber, evacuated, and filled with N_2:H_2 to a pressure of 700 Torr. The reactor was then heated to 450 °C under flowing N_2:H_2. After reaching temperature, TBP was introduced at a flow rate of 40 sccm for 10min and then cooled to 400 °C before turning off TBP and cooling to room temperature.

Raman Spectra comparing exfoliated BP and VP flakes captured using a Renishaw inVia system using a 488 nm excitation source under a backscattering geometry are shown in Figure. 5.6. BP spectrum clearly show the three distinct A_g^1, E_{2g} and A_g^2 Raman modes at 365, 425 and 450 cm^{-1} (figure. 5.6a). In contrast, the VP spectrum (figure. 5.6b) reveals numerous peaks in the range of 100 to 300 and 350 to < 500 cm^{-1} consistent with recent reports on bulk VP synthesis. [164, 169, 170] Compared with the orthorhombic structure of BP, VP's monoclinic structure is

quite complex consisting of layers of perpendicular phosphorus tube structures covalently linked with space group P2/n (13) [164] (Figure. 5.6c). The VP Raman spectrum can be broken down into three regions based on bond distortions: high due to stretching and bending (350 to <500 cm^{-1}) modes, mid due to angle distortions (175 to 300 cm^{-1}), and low frequency due to rotational deformations (<175 cm^{-1}). [171] The distinct crystal and band structures of BP and VP offer the possibility to form unique single element van der Waals heterostructures by combining narrow band BP (0.3 eV) with mid band VP (1.7eV). [164] Figure. 5.6d shows Raman spectra and optical images of a ~ 42nm BP flake on SiO_2/Si after annealing under TBP at 450 °C. Optical images show the flake remains intact; while Raman shows a spectrum with both BP and VP Raman modes demonstrating the possibility of producing such heterostructures. Similar, heterostructures have also been reported during CVT synthesis. [169, 170]

Topographic and near-field broadband IR optical images and nanoscale infrared spectra were acquired using a commercial nano-FTIR setup (neaspec.com), which is extensively described in previous publications. [28, 29, 45] Briefly, it is based on a tapping mode AFM with a cantilevered metal coated tip that oscillates at the resonance frequency, $\Omega \sim 280\ kHz$ and tapping amplitude of ~50 nm. A coherent broadband infrared beam in the frequency range 700-2100 cm^{-1} is focused by a parabolic mirror to the tip. The backscattered near-field light from the tip-sample junction is detected via mixing with an asymmetric Fourier transform Michelson interferometer enabling detection of the amplitude $s(\omega)$ and phase $\varphi(\omega)$ spectra of the backscattered light. To extract background free local near-fields, the detector signal is demodulated at a higher harmonic $n\Omega$ of the tip mechanical resonance frequency Ω. Normalized amplitude (s_n(sample)/ s_n(reference)) and phase (φ_n (sample) -φ_n(reference)) IR near-field spectra are

acquired by first taking reference spectrum on a reference area (silicon is used in these experiments) followed by taking spectra at desired positions on the sample.

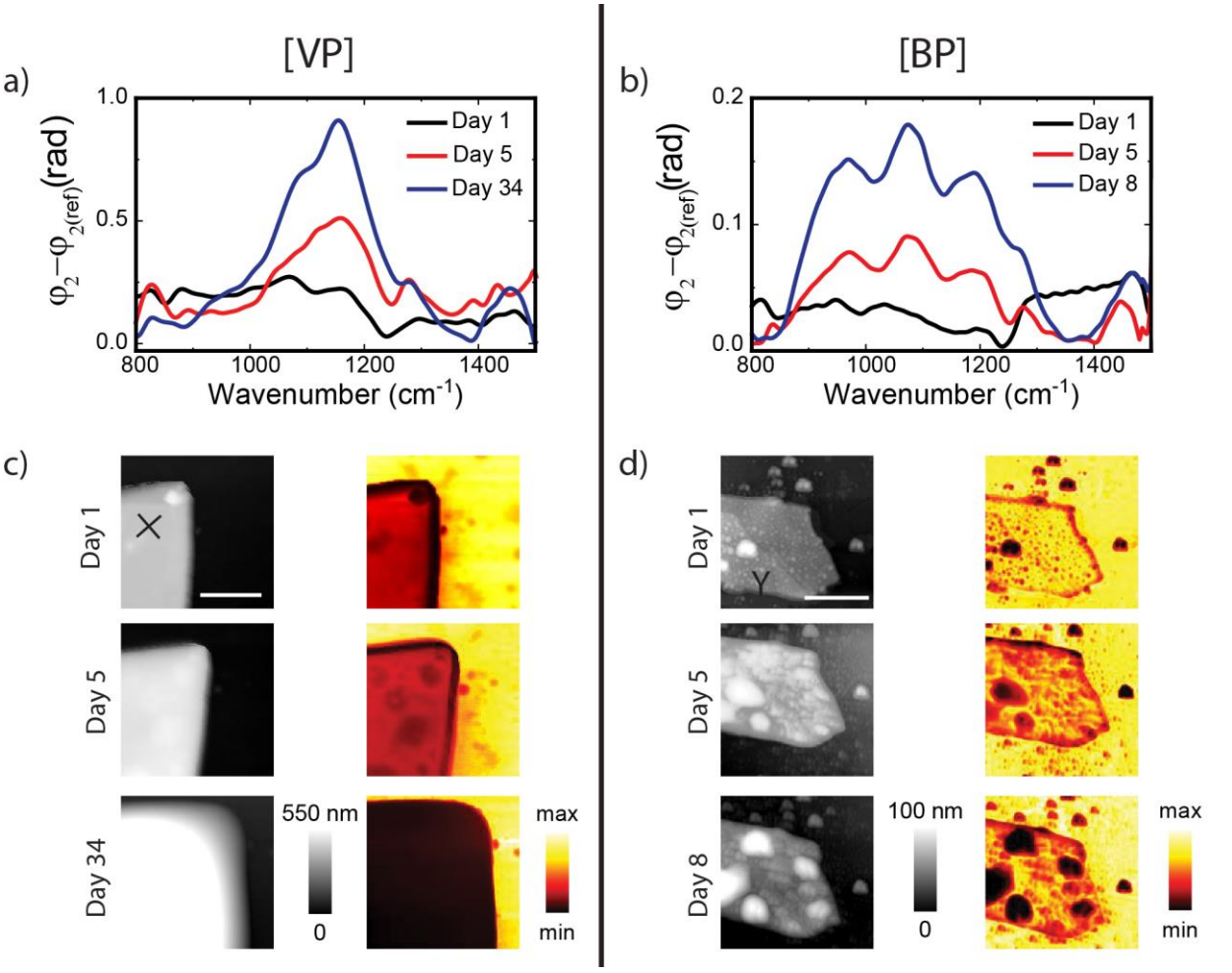

Figure 5.7 Nano-FTIR phase spectra, topography and near-field amplitude images of VP and BP. a) and b) experimental nano-FTIR phase spectra of VP and BP respectively under ambient conditions over time taken at positions marked X and Y in c) and d) topographic images respectively. c) and d) are topographic and 2nd harmonic broadband IR near-field amplitude images of VP and BP respectively taken at different days. Scale bars shown in topographic (Day 1) images in c) and d) represent 2 μm.

We studied the surface chemical modification of phosphorus allotropes (VP and BP) under ambient conditions over time by collecting local spectral changes using nano-FTIR spectroscopy in the frequency range 800-1500 cm^{-1}. The normalized 2nd harmonic phase spectra of an exfoliated 430 nm thick VP sample and a 27 nm thick BP sample taken over several days are shown in figure.

5.7a and figure. 5.7b, respectively. Silicon substrate is used as a reference area to normalize the phase spectra. The phase spectra of VP (taken at the position marked X in figure. 5.7c Day 1) show mainly a broad peak centered around ~1150 cm^{-1} with a shoulder around 1080 cm^{-1} that increase in intensity with time. The phase spectra of BP (taken at the position marked Y in figure.5.7d Day 1) show a more complex spectra with 3 resolved peaks on top of a broad background in the range 850-1300 cm^{-1} that increase in intensity with time (going from Day 1 to Day 8).

The mechanism of BP degradation is complex and has been reviewed extensively. [162] The unstable bonding structure arising from the free electron lone pairs of phosphorus atoms making BP susceptible to degradation at a rate that depends on oxygen and water concentration, light intensity, and energy gap. The degradation of the surface results in several phosphorus oxides (P_xO_y) and phosphoric acid species that exhibit stretch modes in the frequency range spanning 800 cm^{-1} to 1300 cm^{-1}. This is clearly captured in the nano-FTIR spectra taken on VP and BP flakes shown in figure. 5.7. The main peaks in these spectra are broad due to a combination of many overlapping modes arising from several phosphoric species. The spectral intensity in both BP and VP increase over time due to increased formation of surface phosphorus oxide products. Oxygen plays a major role in the degradation mechanism by destroying BP's structure via the formation of P-O-P bonds; as such the dominant vibrational peaks are related to P-O stretch modes. The range 870-950 cm^{-1} has been assigned to P-O stretching vibrations in refs [172], whereas symmetric phosphate (PO_2-) stretching vibrations are centered at 1080 cm^{-1}, [173] and the range 1180-1250 cm^{-1} is assigned as P=O stretch modes. [174] Similar to BP, oxygen is expected to play a major role in the degradation mechanism of VP, and vibrational peak assignments should be similar.

However, the strong presence of P-O stretch modes in BP, which is not observed in VP, suggests reduced oxygen insertion in VP leading to slower degradation. This is also reflected in the thickness and permittivity changes of these flakes as shown in the topographic and near-field amplitude images (figure. 5.8) discussed below.

Topographic and 2nd harmonic broadband IR near-field amplitude images of the VP flake shown in Figure. 5.7c reveal how degradation evolves in an ambient environment over the course of several days. Comparing the topography of day 1 and day 34 shows that it has uniformly increased in thickness to 1135 nm over the measured area. On the other hand, the topographic change for the BP flake shown in Figure. 5.7d is different increasing from 27 nm up to 81 nm in certain areas, which begin with randomly scattered bubbles on the surface because of degradation. Degradation causes thickness increase due to the insertion of Oxygen atoms[175]. The 2nd harmonic broadband IR near-field amplitude image of VP in Figure. 5.7c reveals changes in contrast between day 1 and day 5 with the appearance of dark spots. By day 34 the whole flake appears uniformly dark with respect to the substrate. This is because the near-field infrared photons probe changes in the permittivity of the sample where a dark signal (with respect to the substrate) implies degradation of the VP flake. Comparing this degradation behavior with BP, a similar appearance of dark spots is observed but with a different trend in how the topography and amplitude contrasts change with time. In BP, these changes start as small bubbles and grow bigger. The changes in topography and near-field amplitude signal are analyzed below.

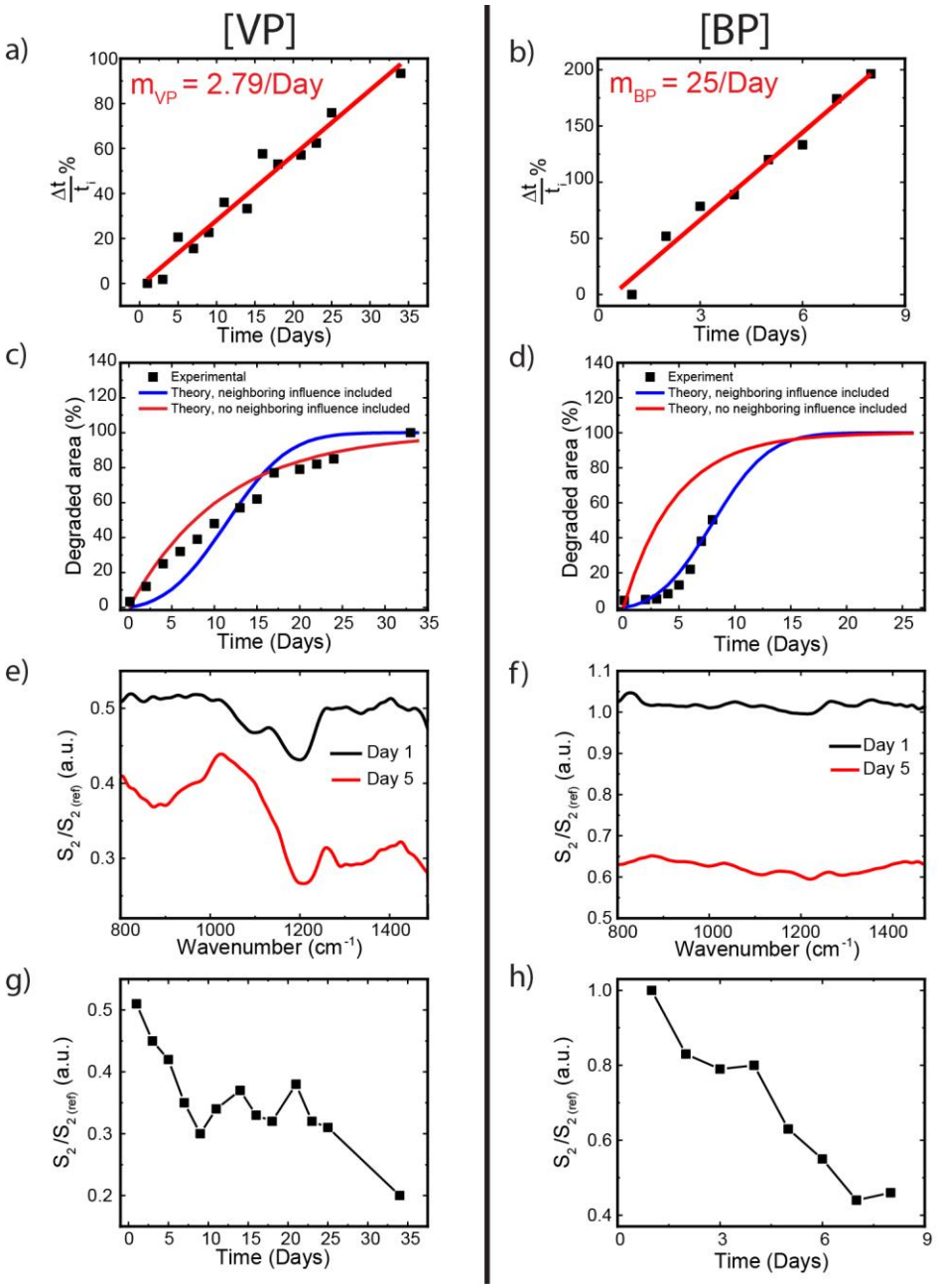

Figure 5.8 Normalize change in topographic height percentage ($\frac{\Delta t}{t_i}$%) over time for (a) VP and (b) BP flake. The solid red lines in (a) and (b) show best fits to experimental data from which slopes (m_{VP} andm_{BP}) were derived. Percent degraded area (squares) extracted from topographic images and theoretical calculations (red and blue lines) for (c) VP and (d) BP flake. Normalized experimental nano-FTIR amplitude spectra at two different days with respect to the Si substrate for (e) VP and (f) BP flakes respectively. Normalized 2nd harmonic near-field amplitude values at 1000 cm^{-1} over time for (g) VP and (h) BP flakes respectively.

Topographic, and IR near-field amplitude spectra analysis shown in figure. 5.8 reveal the degradation of VP and BP surfaces in an ambient environment over the course of several days. The topography of the VP flake changes over time in a way that is noticeably different from surface and height changes observed on BP flakes. First, VP shows more stability than BP as revealed by the topographic and dielectric changes on the surface. Second, VP degradation begins at random locations as bubbles similar to BP. However, in VP, degradation evolution is abrupt and large scale, unlike BP, which evolves via connection of local bubbles towards saturation following a sigmoid growth curve (see Ref[176, 177] also for BP degradation study). In both VP and BP surfaces, topographically higher nano-islands appear darker than the substrate in the amplitude images. Such a negative contrast in the broadband IR near-field amplitude images is due to the small dielectric constant of the degraded islands compared to the undegraded areas, which are identified as phosphorus oxide species in the phase spectra shown in figure. 5.7.

We extracted topographic geometric changes (thickness and area) and the corresponding near-field amplitude spectra over time in VP and BP flakes and compare them with an analytical model. In figure. 5.8a&b we show plots of the normalized change in topographic height percentage ($\frac{\Delta t}{t_i}\%$) over time for VP flake at point X (in figure. 5.7c) and BP flake at point Y (in figure. 5.7d) respectively. We note that spots X and Y are chosen as exemplary/arbitrary points. Here, t_i is the initial thickness of the flake at the start of the experiment (day 1) and Δt is the topographic thickness change ($t_n - t_i$, where t_n is the height on the day measured). From linear fits (red line) to experimental data in figure. 5.8a, 8b, the slope of the normalized change in topographic height percentage in BP ($m_{BP} = 2.79/day$) is a factor of ~9 larger than that of slope of VP ($m_{VP} = 25/day$). The slope comparison shows that the change in flake heights increase linearly for both

VP and BP samples with time as they degrade; however, BP shows a large topographic height change over the same time period when compared to VP exposed to the same ambient conditions. In addition to the dramatic increase in height during VP and BP chemical degradation, the surface area of the degraded bubbles in both flakes increase laterally albeit at different rates. We show plots of the measured fraction of the degraded areas as a function of time in figure. 5.8c&d for VP and BP flakes respectively. Each data point on the plots (dark squares) in figure. 5.8c&d represent the sum of the measured area of each degraded bubble divided by the total area of the sample. The degraded surface area was measured using the change in the height of a given location on a sample by setting a height threshold value for each scan. The experimental plot shown in figure. 5.8c reveals that for the VP flake the degraded area percentage increases steeply with time in the beginning then curves slowly towards saturation and is completely saturated at day 34, at which time we stopped measuring further height increments in the sample. Like with BP, the degradation of VP begins soon after exfoliation as nano-sized particles appear randomly on the surface; however, the proceeding growth dynamics of the nanoparticles are different from what is observed in BP as shown in figure. 5.8d (also see Ref[[176]]). In BP, the degraded area percentage change follows the sigmoid (S-shaped) growth curves where the area percentage of the degraded regions initially increase slowly then grow in an exponential fashion as particles start to coalesce covering the entire surface by day 15.[176, 177] The degraded area percentage differences between VP and BP may be explained by different degradation processes as indicated in the phase spectra shown in figure. 5.7. To qualitatively understand these differences and the degradation process of VP, we use a variant of the forest-fire model to fit our experimental data. The model is described in detail in Ref[[176]]; briefly, the sample surface is divided in N × N square elements, where each square

can be either in an undegraded or degraded state. We calculate the degradation probability after a small time interval Δt using $P_n = 1 - e^{-\Delta t.\eta^{(n)}}$ where $\eta^{(n)}$ is degradation probability per unit time of a surface element that has n degraded neighbors ($0 \leq n \leq 8$). Each degraded neighbor increases $\eta^{(n)}$ by a fixed amount $\Delta\eta$, that is, $\eta^{(n)} = \eta^{(0)} + n\Delta\eta$, where $\eta^{(0)}$ is the degradation probability per unit time. We note that this model gives a good fit to the VP experimental data only if we neglect the influence of neighbors on the degradation probabilities by setting $\Delta\eta$=0, as shown by the red curve in figure. 5.8c. If, on the other hand, the influence of degraded neighbors is included, the model does not predict the experimentally observed results (figure. 5.8c blue curve). The opposite scenario is true for BP where the model predicts the correct experimental behavior only if the influence of neighbors on the degradation probabilities is included as shown in figure. 5.8d (also see Ref[[176]]). The model thus suggests, unlike BP, the influence of degraded surface elements on non-degraded ones does not contribute to the degradation process of VP.

The time dependent IR near-field amplitude spectra provides information on real time degradation changes of the real part of the local complex dielectric properties of the sample. Second harmonic normalized nano-FTIR amplitude spectra of VP are shown in figure. 5.8e taken at the point X in figure. 5.7c at 2 different days. A similar plot for BP taken at the point Y in figure. 5.7d is shown in figure. 5.8f. The normalized amplitude values decrease significantly over time as the samples degrade, which also complements the increasing topographic height in figure. 5.8a&b. Figure. 5.8g &h show the 2nd harmonic normalized nano-FTIR amplitude spectra values extracted at 1000 cm^{-1} from amplitude spectra for VP and BP respectively over time. The decreasing normalized amplitude signal level, shown over several days in figure. 5.8g&h, are caused by continually decreasing polarizability of the sample during degradation over time, and the effective

real-part of the dielectric functions are continuously decreasing for both VP and BP flakes affecting the tip-sample near-field coupling.[28, 29, 31, 45]

5.2.4 Conclusion

In summary, we have studied ambient degradation of CVD synthesized VP in comparison with BP using Raman and nano-FTIR spectroscopy in the frequency range 800-1500 cm^{-1}. VP Raman spectra is characterized by several peaks in the frequency range 100 to 300 and 350 to 500 cm^{-1} including stretching and bending modes, angle distortions, and rotational distortions. The nano-FTIR phase spectra of VP and BP show broad peaks on top of a broad background resulting from a combination of many overlapping phosphorus oxides and phosphoric acids species modes in the range of 850-1300 cm^{-1}, which increase in intensity with time due to degradation of the surface. Differences in the degradation spectra as well as thickness and permittivity changes between VP and BP indicate reduced oxygen insertion in VP, resulting in slower degradation compared to BP. VP is a new vdW materials with promising electronic and photonic applications, and fundamental understanding of its properties and degradation process in comparison with other phosphorus allotropes will likely enable the realization of its full technological potential.

5.3 Photo-degradation protection in 2D in-plane heterostructures revealed by hyperspectral nanoimaging: the role of nano-interface 2D alloys

This section is reprinted from {Alireza Fali, Tianyi Zhang, Jason Patrick Terry, Ethan Kahn, Kazunori Fujisawa, Bernd Kabius, Sandhaya Koirala, Yassamin Ghafouri, Da Zhou, Wenshen Song, Li Yang, Mauricio Terrones, and Yohannes Abate, Accepted by ACS Nano Vol. 15 Issue 2 Pages 2447-2457, (2021) Copyright {2021} American Chemical Society}.Reprinted here with permission of publisher

5.3.1 Abstract

Single-layer heterosructures heterostructures exhibit striking quasiparticle properties and many-body interaction effects that hold promise for a range of applications. However, their properties can be altered by intrinsic and extrinsic defects, thus diminishing their applicability. Therefore, it is of paramount importance to identify defects and understand 2D materials' degradation over time using advanced multimodal imaging techniques. Here we implemented a liquid-phase precursor approach to synthesize 2D in-plane MoS_2-WS_2 heterostructures exhibiting nanoscale alloyed interfaces and map exotic interface effects during photo-degradation using a novel combination of hyperspectral tip-enhanced photoluminescence, Raman and near-field nanoscopy. Surprisingly, 2D alloyed regions exhibit remarkable thermal and photo-degradation stability providing protection against oxidation. Coupled with surface and interface strain, 2D alloy regions create stable localized potential wells that concentrate excitonic species via a charge carrier funneling effect. These results demonstrate 2D alloys can withstand extreme degradation effects over time and could enable stable 2D devices engineering.

5.3.2 Introduction

The creation of in-plane and out-of-plane van der Waals (vdW) heterostructures from atomically thin monolayers has opened unprecedented possibilities to artificially design excitonic materials with strong many-body effects that exhibit exciting new physics and novel applications.[178, 179] Building vdW heterostructures is like assembling an atomic Lego® set where each two-dimensional (2D) crystal Lego block can be vertically stacked, rotated or laterally stitched together to produce structures with designed excitonic effects. [179, 180] Both top-down and bottom-up strategies have been used to assemble complex excitonic vdW heterostructures with

new properties not found in the bare monolayers. [180-182]

In-plane heterostructures with *lateral* interfaces, distinct from vertical heterostructures, can be created via covalent bonds of different domains as a single, continuous sheet that can then be extended into vdW stacks of more complex heterostructures. These heterojunctions could result in fascinating physical phenomena for constructing unique devices based on high-mobility field-effect transistors and planar monolayer p–n junctions. [183] In these lateral interfaces, new types of interactions such as intralayer coupling, lateral strain, interface defects and 2D alloys can have significant effects on the oxidation process and spatial distribution of exciton emission. The heterojunction boundary between dissimilar lateral domains presents a novel platform to explore interface physics in one dimension such as spin and valley transport and exciton diffusion across the interface, many-body interaction effects in 1D quantum confined quasiparticles trapped between atomically thin barriers. [184] In vertically stacked heterostructures, photo-induced oxidation and environmental effects on exciton species are inherently confined to a single layer or interlayer of the heterostructure. Due to the advantages these heterointerfaces offer, new approaches to monitor and understand their stability and degradation over time are needed, and multimodal advanced imaging and spectroscopy techniques with ultrahigh resolution could be implemented. These techniques are advantageous due to their sensitivity and ability to initiate and probe light-driven nanoscale optical and electronic processes in 2D systems. Consequently, high sensitivity photoluminescence (PL) /Raman spectroscopy and imaging techniques have been applied to study a wide range of exciton related phenomena in 2D materials and their heterostructures.[185-193] However, it is still important to perform a comprehensive understanding of the surface and interface chemistry of 2D heterointerfaces, as well as their

mechanical, electronic and optical effects that give rise to the complex excitonic phenomena and monitor their evolution in time with high spatial resolution.

In this work MoS_2-WS_2 heterostructures was prepared by Dr. Terrones's research group at PSU. In this work, using in-plane MoS_2-WS_2 heterostructures (with Mo-rich in inner regions, W-rich in outer regions, and a ~100 nm 2D alloyed interface. See details in figure 5.9) as a model system, we observed interface-protected exciton stability, localization and inhomogeneities during photodegradation by implementing a combination of hyperspectral tip-enhanced photoluminescence and Raman nanoimaging in concert with scattering type scanning near-field microscopy. Monosulfur vacancies abundant along the edge regions offer thermodynamically favorable sites for oxygen reactivity, favoring the photo-induced oxidation of the outer WS_2 monolayer (ML) while oxidation progression to the inner MoS_2 ML is inhibited by the presence of the 2D alloy interface. [194] Interestingly, this alloy interface corner regions, being thermodynamically stable [195] , exhibit higher stability against photooxidation and facilitate the generation of localized potential wells that accumulate excitonic species via charge carrier funneling effect with minimized Auger recombination losses. The spectral weight of trion and biexciton, when compared to the neutral exciton intensity, decreases with photo-degradation, and biexciton emission quenches much faster than trion emission due to changes in Coulomb screening caused by the oxidation process. High-resolution scanning transmission electron microscopy (HRSTEM) characterizations revealed that WS_2-MoS_2 alloy regions are stable during and after exposure at high temperatures. These results provide novel insights into the role of the 2D alloys at lateral interfaces and evolution of neutral and charged excitons critical for optical, electrical and thermal device engineering based on 2D materials and their heterostructures.

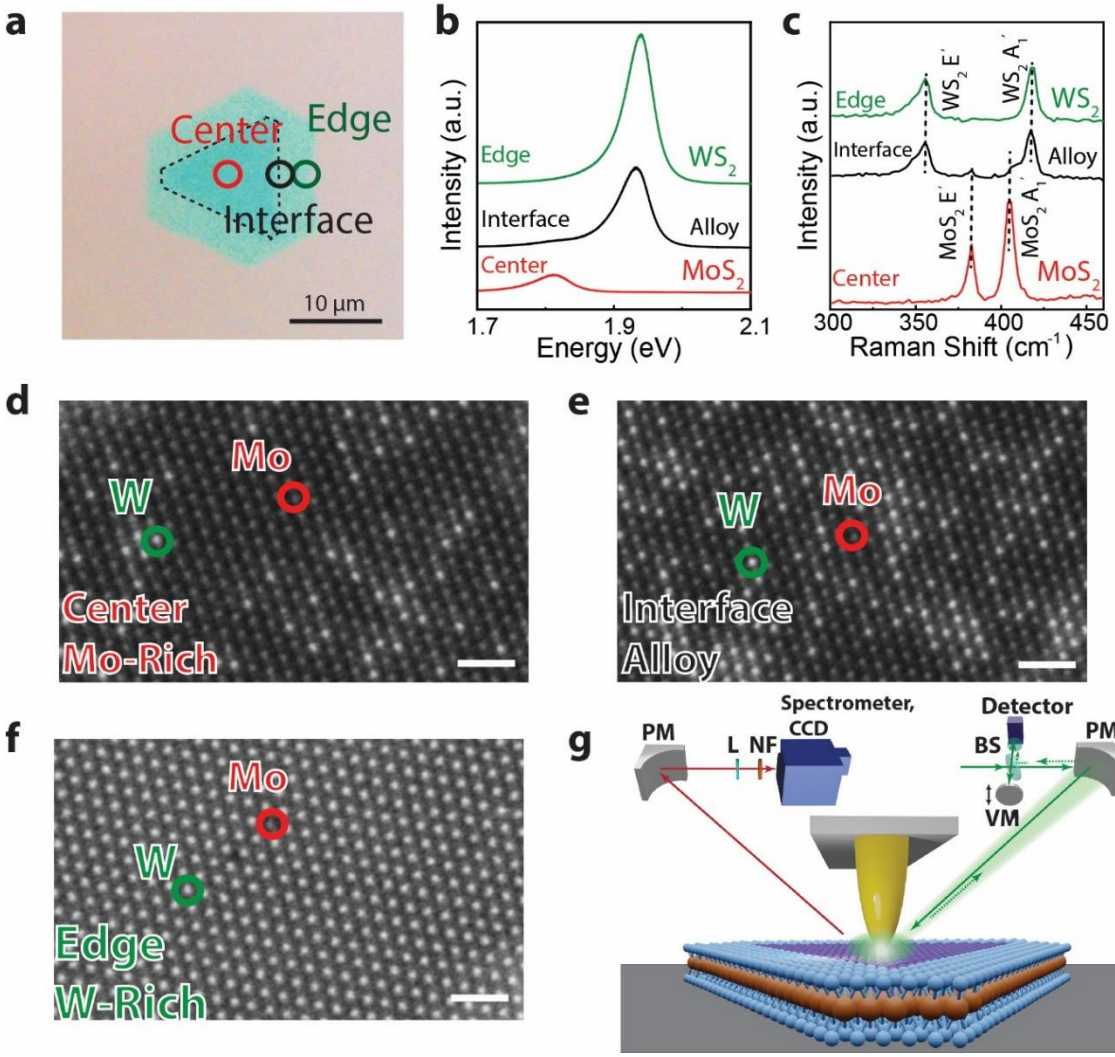

Figure 5.9 Monolayer MoS_2-WS_2 lateral heterostructures. (a) An optical image of as-grown in-plane MoS_2-WS_2 heterostructures on SiO_2/Si substrate. Center, interface and edge regions of the flake are marked with red, black and green circles, respectively. The interface region is highlighted in white broken lines. (b) Photoluminescence (PL) spectra of the center, interface and edge regions of the MoS_2-WS_2 lateral heterostructures. (c) Raman spectra of the center, interface and edge regions of the MoS_2-WS_2 lateral heterostructures. (d-f) Typical AC-HRSTEM images acquired from the center, interface, and edge areas of the MoS_2-WS_2 lateral heterostructures. Atoms with brighter and darker contrast are W (green circle) and Mo (red circle), respectively. The STEM-high-angle annular dark-field (HAADF) characterization confirms the center region is Mo-rich, the edge region is W-rich, and the interface displays an intermixing of Mo and W, forming an alloyed $Mo_xW_{1-x}S_2$ composition transition region. Scale bar is 1 nm. (g) Schematics of integrated s-SNOM/TEPL/TERS experimental setup (PM = parabolic mirror, NF = neutral density filter, BS = beam splitter, VM = vibrating mirror).

5.3.3 Characterization of structural and optical properties of MoS_2-WS_2

The samples used for this work are in-plane MoS_2-WS_2 heterostructures grown on SiO_2/Si by spin-coating of liquid-phase precursors and subsequent high-temperature sulfurization under ambient pressure (see Methods for the detailed process). [191] Optical microscopy (figure 5.9a) shows the monolayer exhibiting a truncated triangular shape. The optical image reveals that the center and edge regions exhibit distinct optical contrasts, separated by an interface region highlighted by the white dashed line, which indicates different chemical compositions within center and edge regions of the monolayer. Far-field Raman and PL spectroscopies were used to characterize structural and optical properties of the MoS_2-WS_2 heterostructures, respectively. PL spectra (figure 5.9b) in the hetero-monolayer reveal PL emission at ~1.81 eV and ~ 1.94 eV from center and edge, close to the optical band gap of MoS_2 and WS_2 monolayers, respectively. [196] Raman spectroscopy (figure 5.9c) reveals spectroscopic features of MoS_2 E' and A_1' modes at the center, and WS_2 E' and A_1' modes at the edge while the interface region displays a combination of MoS_2-like and WS_2-like Raman modes. Aberration corrected high-resolution scanning transmission electron microscopy (*AC-HRSTEM*) images in figure 5.9d-f provide atomic-resolution images of the MoS_2-WS_2 heterostructures; Mo (indicated by red circles) and W atoms (indicated by green circles) can be clearly resolved by the atomic number contrast in the high-angle annular dark-field (HAADF) imaging mode. AC-HRSTEM confirms that the center and edge regions are Mo-rich and W-rich, respectively, and also reveals some W alloying in the central Mo-rich region (figure 5.9d&f). It should be noted that the STEM image at the interface between Mo-rich and W-rich regions unambiguously shows the intermixing of Mo and W atoms, forming a region of alloyed $Mo_xW_{1-x}S_2$ (figure 5.9e). The width of the alloyed interface is on the order of

~100 nm with alloy compositions continuously changing from Mo-rich (center-side) to W-rich (edge-side), in agreement with our recent observations on the MoS_2-WS_2 heterostructures grown using identical conditions.[197]

The schematics of the multi-modal imaging setup are shown in figure 5.9g. The integrated near-field, hyperspectral TEPL and TERS nano-imaging technique we introduce here is a combination of a commercial s-SNOM (neaspec co.) with a grating spectrometer, coupled to a silicon charge-coupled device (iDUS, Andor). This configuration allows detecting either the elastic backscattered field, as typically of s-SNOM, or inelastic forward scattered signals. The tip-enhanced inelastic forward scattered signals (TEPL or TERS) are dispersed in a spectrometer, after passing through a notch filter to remove elastically scattered field, and detected with a CCD (see chapter 2 for details).

5.3.4 Tip-Enhanced hyperspectral PL nanoimaging

We demonstrate tip-enhanced hyperspectral PL nanoimaging of ML in-plane heterostructure and map the temporal and spatial degradation and exciton evolution over an extended time (> 100 days). figure 5.10 shows 3D hyperspectral data cube taken at 1, 5, 20, 85 and 103 days since the start of experiment acquired by measuring an array of 85 by 85 pixels TEPL normalized spectra of the ML heterostructure (shown in figure 5.9a). The x and y axes of the 3D data cube shown figure 5.10a, indicate the plane of the sample surface while the z-axis correspond to the photon-energy axis (1.77 eV to 2 eV). The acquisition time for each spectrum was 1 second, thus yielding a total acquisition time of 2 hours per image in figure 5.10a. Monochromatic TEPL images are then extracted by cutting the cube at selected energies, 1.81 eV and 1.94 eV, close to PL resonance emission of neutral excitons of ML WS_2 (figure 5.10b) and MoS_2 (figure 5.10c),

respectively. These hyperspectral time-series images reveal dissimilar spatio-spectral inhomogeneities between the outer WS_2 and inner MoS_2 MLs, providing rich information on the evolution of exciton emissions and degradation of the heterostructure. In figure 5.10a and b we observe striking spatially inhomogeneous degradation of the outer WS_2 ML neutral exciton emission which evolves over time and completely disappears after several days. This contrasts the evolution of the inner MoS_2 ML that shows a homogeneous quasi-stable exciton emission (figure 5.10c). The TEPL image of MoS_2 on day 1 also shows signal on WS_2 region due the broad and strong WS_2 spectrum, when the WS_2 peak is subtracted emission only from MoS_2 ML is observed (see figure 5.10d).

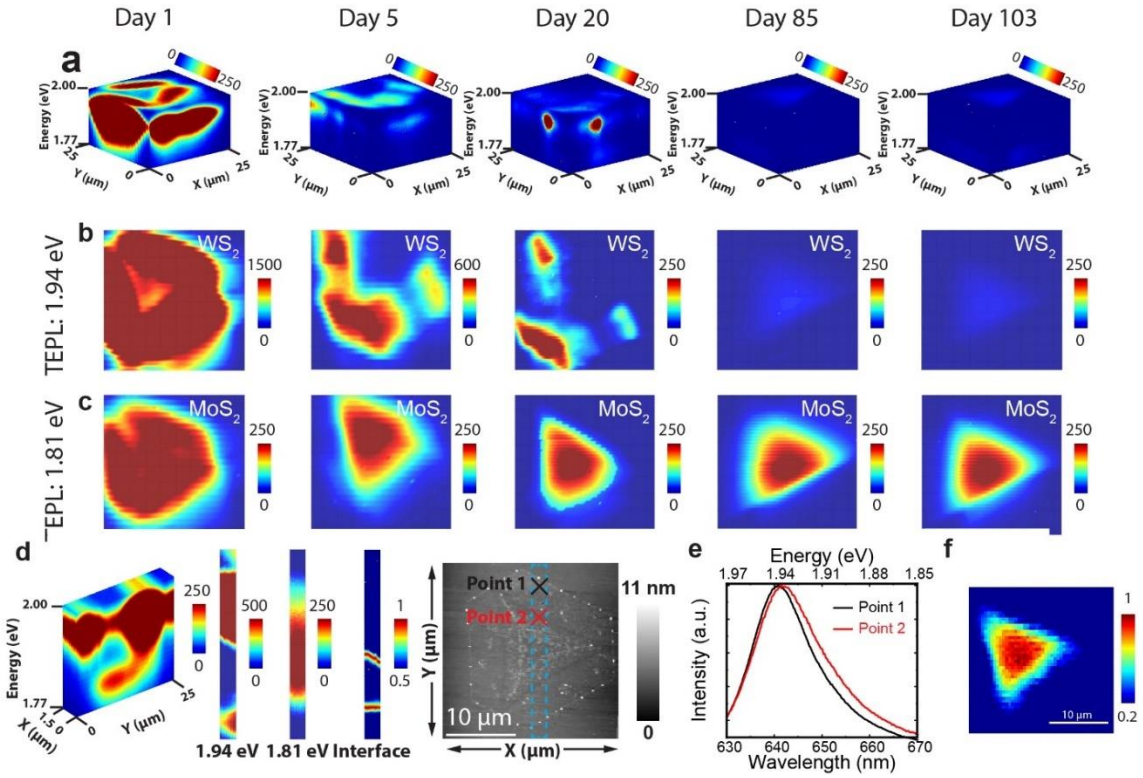

Figure 5.10 Hyperspectral TEPL nanoimaging showing time evolution of exciton emission in heterostructure monolayer MoS_2/WS_2. (a) TEPL hyperspectral 3D data cube taken as a function of time (days 1-103). (b) cross-section cut of TEPL map taken at 1.94 eV and (c) 1.81 eV corresponding to the exciton peaks expected for WS_2 and MoS_2 respectively. (d) High-resolution TEPL hyperspectral 3D data cube of flake taken in blue dashed area shown in topography and cross-section cut of high resolution TEPL map taken at 1.94 eV, 1.81 eV, and 1.93eV corresponding

to the exciton peaks expected for WS_2 and MoS_2 and interface respectively. Note that the interface's intensity has been normalized and is displayed with a lower limit of 0.5 (e) PL point Spectra taken at WS_2 (point 1) and interface (point 2). (f) TEPL image of MoS_2 when the WS_2 peak is subtracted. cross-section cut of TEPL map taken at 1.81 eV when WS_2 peak is subtracted.

The TEPL images in figure 5.10 clearly show that quenching of excitonic emission preferentially begins from the outer WS_2 ML and propagates towards the inner MoS_2 ML. This may be due to the presence of higher S vacancy concentrations along the edges in CVD grown samples, which lead to accelerated degradation. Our recent atomic-resolution imaging revealed that the areal density of monosulfur vacancies in WS_2 is much larger near the edges (~0.92 nm^{-2}) than in the interior (~0.33 nm^{-2}). [194] The large presence of S vacancies along edges presents a thermodynamically favorable energy landscape for oxygen substitutions, greatly accelerating the photo-induced oxidation of the outer WS_2 ML (figure 5.10b). Surprisingly, the inner MoS_2 ML has shown more resilience to oxidation, exhibiting only ~8% quenching of PL emission on day 103 (compared to Day 1 in figure 5.10b), while the PL of outer WS_2 completely disappears during the same period and the same laser exposure. This is interesting because the inner MoS_2 region is also expected to have a large number of S vacancies, but the oxidation, unlike WS_2, is uniform and minimal. [198] Li et al. have also reported a laser-induced oxidation process in TMDC crystals that starts from the edges leaving central area intact, an effect attributed to highly defective edges. [199] We note in our work that there is a 2D alloy interface that plays a critical role in making the material it encloses more stable, prohibiting oxidation propagation from the edge inward to MoS_2 (see figure 5.10 d discussion below). In figure 5.10d, we show high-resolution TEPL hyperspectral 3D data cube of a small section of the heterostructure sample (blue dashed area indicated in Topography figure 5.10d) and identify the interface region between MoS_2 and WS_2 MLs (figure 5.10d). The alloy interface is characterized by a broad and slightly red shifted spectrum compared

to WS_2 owing to its alloy nature (figure 5.10 e). By subtracting the WS_2 and MoS_2 resonance PL emissions from the interface emission we can extract the nano-interface 2D PL image that exists at the physical boundary of MoS_2 and WS_2 (figure 5.10d). Furthermore, in figure 5.9e, AC-HRSTEM image at the nanoscale (~100 nm) alloyed interface shows an intermixing of MoS_2 and WS_2 (local concentrations of ~35% W and ~65% Mo). The formation of $Mo_xW_{1-x}S_2$ alloys is energetically favored and thus thermodynamically stable [195], which may result in higher stability against photooxidation, thus indicating a potential route to degradation prevention by lateral 2D encapsulation. We have carried out a direct comparison of degradation between identically prepared pristine MoS_2 and WS_2 monolayers by performing hyperspectral nanoimaging and by exposing the flakes to identical laser light irradiation for the same amount of time (see figure 5.11 and accompanying text for the experimental details and data analysis). These control experiments show that both of these pristine flakes degrade similarly in the same periods of time, so that the degradation behavior of the MoS_2/WS_2 heterostructures, is not due to large stability differences between pristine MoS_2 and WS_2.

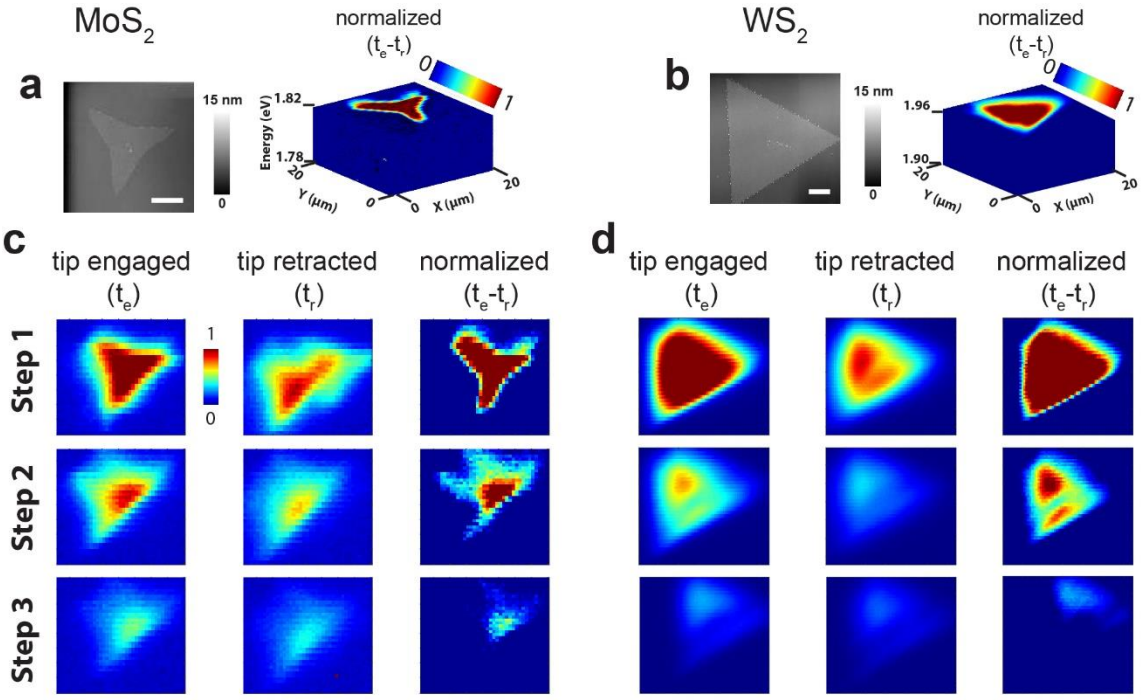

Figure 5.11 Hyperspectral TEPL nanoimaging comparing degradation of CVD grown pristine MoS_2 and pristine WS_2 MLs exposed to identical degradation conditions**.** Topography and TEPL hyperspectral 3D data cubes taken on the sample surface normalized spectra (t_e -t_r) for MoS_2 (a) and WS_2 (b). Normalized cross-section cut of TEPL maps of MoS_2 taken at 1.81 eV (c) and WS_2 taken at 1.94 eV (d) at three identical degradation steps over the same time. scale bar is 5μm

The samples were CVD-grown pristine WS_2 and MoS_2 MLs (synthesized under identical experimental conditions as the heterostructure samples used in the manuscript, see figure 5.11 a &b for topography). We took four hyperspectral 3D data cubes (2 data cubes for each sample, one with tip engaged and one with tip retracted), at 500 nm/pixel (i.e. 20x20 μm using 40x40 pixels for MoS_2 and at 32x32 μm using 64x64pixels for WS_2) at identical experimental conditions. In order to obtain the normalized TEPL hyperspectral 3D data cube, first the tip is retracted from the sample flake to record a reference spectrum (t_r image shown in figure 5.11). Subsequently, a spectrum is taken on the sample surface while the tip is engaged (t_e image shown in figure 5.11). A normalized spectrum (t_e-t_r image shown in figure 5.11) is recorded by subtracting the reference spectra from the spectra taken on the sample. From the normalized 3D hyperspectral image, we

took a cross-section cut of TEPL map close to the bandgap of WS_2 or MoS_2. figure 5.11 show the degradation comparison of pristine MoS_2 (figure 5.11 c) and pristine WS_2 (figure 5.11 d) monolayers identically exposed to extended periods of laser light in order to accelerate degradation. For identical degradation conditions both pristine MoS_2 and WS_2 flakes degrade identically and similar periods of time (in three steps over a period of a week). Figure 5.11 e show a sample of how normalized TEPL images shown in panel figure 5.11 c & d have been achieved by subtracting the reference image from the image taken on the sample at the same energy cross-section. Although there are slight differences in degradation between flakes, overall the degradation in both monolayers, exposed to similar laser exposure, occur from the edge towards the center in a similar amount of time.

5.3.5 Optical and near-field imaging of selective photo-degradation

The observed distinctly different ambient degradation behavior within different regions of the ML heterostructure is selectively photo-induced. This is clearly evident in figure 5.12 a,b, where light emission of identical flakes that are either exposed to tip-focused laser radiation or ones that are not exposed to laser radiation are compared. In the optical image in figure 5.12 a, the laser-irradiated flake is distinguished and marked with a yellow dashed circle, and exhibits a different optical contrast compared with other unexposed flakes. In figure 5.12b the corresponding diffraction limited PL image acquired using a band-pass filter centered at 630 nm, close to the neutral exciton emission of monolayer WS_2, clearly shows that the irradiated flake's PL emission from the edge region is completely quenched while other flakes show no signs of oxidation during the span of the experiment. Ambient photooxidation of TMDC has been extensively investigated

by several groups [199-204] and evidently such selective photooxidation indicate a possible means to use tip nano-focused light for local exciton engineering.

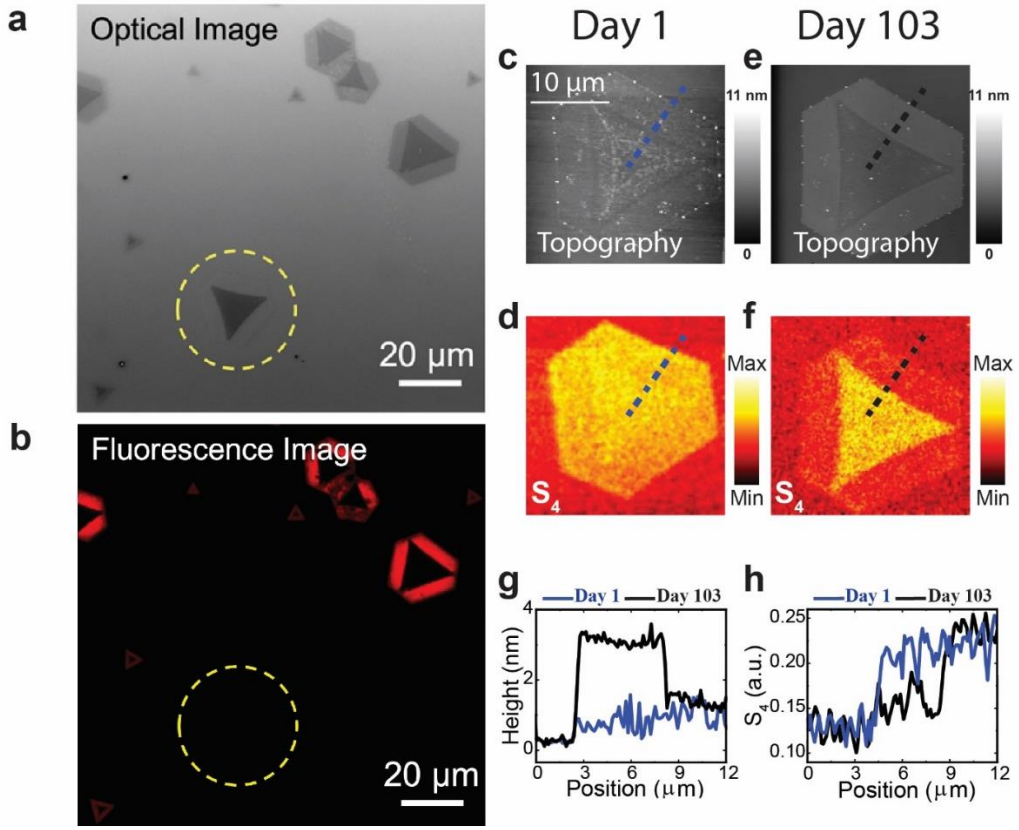

Figure 5.12 Selective photo-degradation of in-plane heterostructure monolayer MoS_2/WS_2. (a) Optical image of MoS_2-WS_2 lateral heterostructures acquired on day 103. The laser-irradiated flake is distinguished and marked with a yellow dashed circle, which exhibit a very different optical contrast compared with other unexposed flakes. (b) The corresponding fluorescence image acquired using a band-pass filter centered at 630 nm (also acquired on the same day). The irradiated flake, fluorescence emission from edge region is completely quenched. Topography and 4th harmonics near-field images and line profiles of the MoS_2-WS_2 monolayer heterostructure taken at day 1 (c-d) and day 103 (e-f). (g-h) topography and fourth harmonic near-field amplitude change of MoS_2-WS_2 monolayer heterostructure between day 1 and day 103, line profiless in g and h show drawings from top right to bottom left in images c-f

The photooxidation process also induces significant and inhomogeneous topographic and permittivity changes in the ML heterostructure. The topography scan at the start of experiment shows a thickness within ~ 1 nm (figure 5.12c), indicating the monolayer nature of the heterostructures. After photooxidation the topography of the edge WS_2 ML increased to 3 nm whereas the inner MoS_2 heterostructure increased to ~1.2 nm (figure 5.12e), as shown in the line

profile in figure 5.12g. Over a factor of two thickness increase of WS_2 ML compared to inner MoS_2 ML indicates a stronger photo-induced aging of the WS_2 ML region. [176, 200] Such topographic height increase has been reported previously and is attributed to laser-induced formation of few nanometer tungsten oxide, as confirmed by Raman measurements performed in the ambient conditions. [199] Other studies have attributed topographic changes in photo-oxidized WS_2, likely due to the H_2O moisture intercalation effect [205], or the alteration of chemical composition in this region. [200]. In our work, the mechanism of degradation is due to the in-plane heterostructure nature of the ML and the significant role the interface (2D alloy) plays. The alloy interface, located between the outer WS_2 and the inner MoS_2 regions, protects MoS_2 from faster degradation resulting in the outer WS_2 ML disproportionate topographic increase.

Simultaneously with topographic images, we acquired near-field s-SNOM amplitude images at the fourth harmonic (A_4) of the tip oscillation frequency. Near-field amplitude images taken at day 1 before photooxidation (figure 5.12d) and on day 103 images after photooxidation (figure 5.12f) show striking contrasts. On day 1, the center MoS_2 ML show slightly brighter contrast compared to the edge WS_2 ML owing to the larger permittivity of MoS_2 at 532 nm excitation wavelength compared to WS_2 (figure 5.12d, h). [206] On day 103, the center MoS_2 ML shows significantly brighter contrast compared to the edge WS_2 ML (figure 5.12f, h). This is because photooxidation significantly lowers the dielectric constant of WS_2 while the inner MoS_2 ML remains stable since it is protected by the alloy interface. We analyzed the s-SNOM contrast further by performing calculations using the well-established finite dipole model.[44, 47] On day 1 the experimental 4^{th} harmonic amplitude ratio of the ML to SiO_2 substrate are, $A_4(MoS_2)/A_4(SiO_2)$~1.77 and $A_4(WS_2)/A_4(SiO_2)$~1.65. The amplitude contrast calculations using

the finite dipole model employing literature data [206] for the dielectric values of MoS_2 ($\varepsilon = 20 + 11i$) and WS_2 ($\varepsilon = 18 + 7i$) and $\varepsilon = 2.15$ for SiO_2 gives $A_4(MoS_2)/A_4(SiO_2)$~1.76 and $A_4(MoS_2)/A_4(SiO_2)$~1.68 in good agreement with experiment. On day 103, after photooxidation has occurred, the experimental 4^{th} harmonic amplitude ratio are $A_4(MoS_2)/A_4(SiO_2)$~1.70 and $A_4(WS_2)/A_4(SiO_2)$~1.27. To match this experimental amplitude ratio, in the calculation we adjusted the dielectric constant for WS_2 to $\varepsilon = 6.3+2.5i$, a large decrease from day 1 values used. Thus, the change in the amplitude contrast in WS_2 can be explained by its large decrease in the dielectric values due to photooxidation whereas the amplitude contrast for MoS_2 remain relatively the same and so is its dielectric values. The near-field amplitude contrast changes indicate that the outer WS_2 monolayer has significantly undergone photo-induced oxidation when compared to the inner MoS_2 ML. These observed large differences in both optical constants and topographic protrusions between the two MLs as revealed by s-SNOM, despite similar laser exposure and ambient conditions, highlight the significant role of the interface.

5.3.6 Tip-enhanced Raman hyperspectral nanoimaging

To correlate TEPL images (figure 5.10) that show site selective enhanced intensities with structural changes that occur during photooxidation, we performed tip-enhanced Raman (TERS) hyperspectral imaging and acquired spatial and spectral information at every pixel on the same scan area and time sequence as in figure 5.10. In figure 5.13 we show the 3D TERS hyperspectral data cube and monochromatic TERS images taken at 3 selected dates, day 20, 85 and 103, acquired by measuring a TERS spectra array of 60 by 60 pixels. Data acquisition and spectrum normalization were performed similarly to TEPL data cube (see Methods). The gap in the 3D data cube in figure 5.13 a is deliberately made to show both the characteristic Raman modes A'_1 (very

top slice) and E' (top of the cube) of MoS_2. For all the selected days shown, we observe intensity changes over time and spatial variations of the E' Raman mode on the outer WS_2 and both the E' and A'_1 modes on the inner MoS_2 that are in a striking similarity with the TEPL images shown in figure 5.10. These similarities indicate that areas containing higher concentration of WS_2 or MoS_2 inferred from TERS images also show higher PL intensities. [207] Despite the same laser exposure, while all typical Raman peaks of WS_2 disappear after day 85 (figure 5.13), the intensity of A'_1 and E' modes of MoS_2 still show robust stability, indicating the influence of the interface (as discussed above) resulting in distinct degradation evolution of WS_2 and MoS_2 in-plane heterostructures. We have also extracted from the TERS hyperspectral 3D data (Figure 5.13a) Raman image at 329 cm^{-1} (figure 5.13 c) which is characteristics of monoclinic (O-W-O stretching modes), indicating local oxidation (we also observed weak Raman signal corresponding to oxidation at around 707 and 803 cm^{-1}).

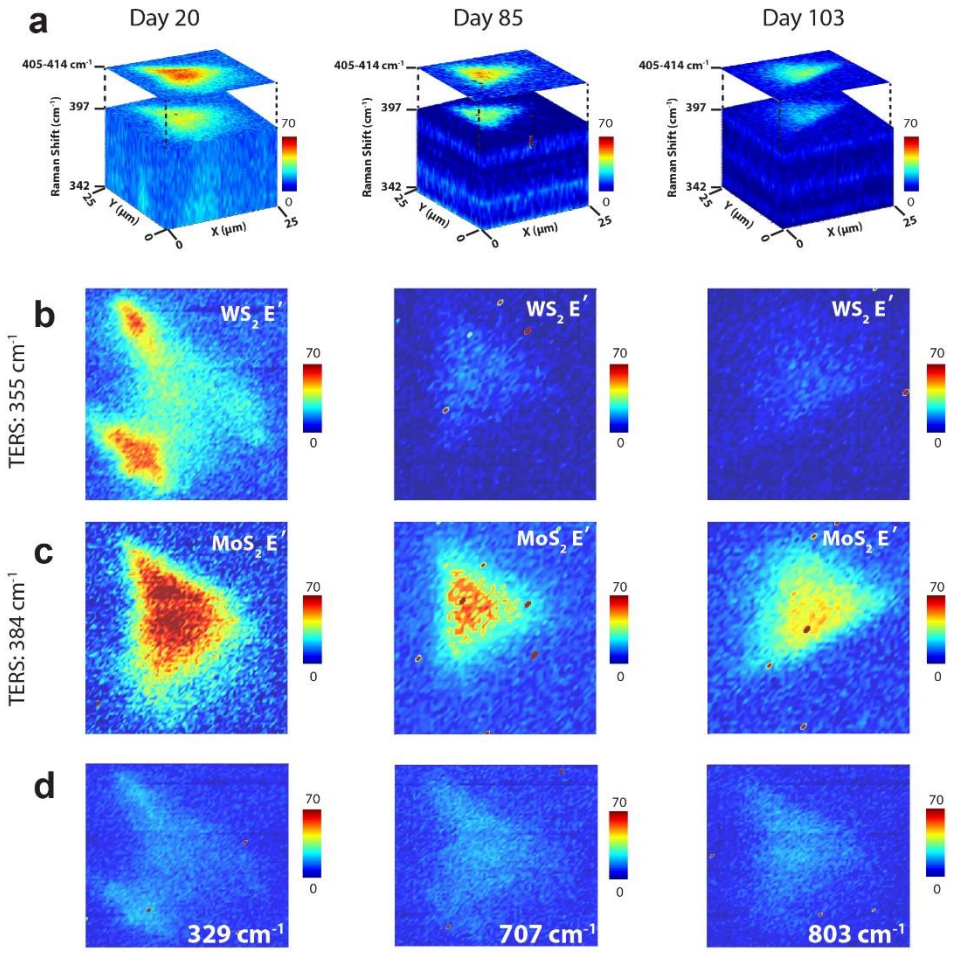

Figure 5.13 Spatial evolution of Raman shift as a function of time in photooxidized heterostructure monolayer MoS_2/WS_2. (a) Hyperspectral TERS 3D data cube shown at selected days. (b) cross-section cut of TERS map taken at 355 cm^{-1} (c) and 384 cm^{-1} corresponding to the Raman shifts expected for WS_2 and MoS_2 respectively on days 20, 85 and 103. (d) Tip Enhanced Raman shift extracted at O-W-O stretching mode. showing cross section of TERS image taken at 329, 707, and 803 cm^{-1} respectively.

5.3.7 Excitonic species PL spectral shifts and local strain effects

Regarding the photodegradation evolution of the 2D heterointerface, figure 5.14a-b show PL point spectra of WS_2 ML taken at points 1&2 (shown in insets in figure 5.14a&b) on different days. The WS_2 PL peak at Point 1 dramatically blue shifts by as much as ~ 10 nm after day 5 (red curve) compared to the peak position at day 1 (brown curve). After day 85, the edge peak at Point

1 completely disappears. A similar trend of blue shift, as well as disappearance of the edge WS_2 peak, is also observed at Point 2 (weighted average peak position shifts as a function of time are also shown in figure 5.14 f). One of the mechanisms that these shifts of exciton energies can be attributed to is the degradation-induced change of strain conditions in samples. Previous first-principles many-body perturbation theory (MBPT) studies have shown that the exciton energy is sensitive to strain conditions in monolayer TMDs. [208] Thus, we fit the observed shifts of PL peaks of the inner and outer parts in figure 5.14 to those calculated exciton energies of strained monolayer MoS_2 and WS_2, respectively. [208] figure 5.14c&d present the fitted strain-distribution maps from the neutral exciton emission on of both Day 1 and Day 20 of the heterostructure sample, respectively. In figure 5.14c, significant strain is observed because of lattice mismatch and a built-in strain in CVD-grown TMDs arising from thermal expansion coefficient mismatch between TMD and substrate. This is the reason why transfer of samples to another substrate has shown to release this built-in strain. [209] There are large positive strains (dark red) around the outer WS_2 area and very small strain (white) around the inner MoS_2 area. For example, the strain is +0.12% at the outer point while that is nearly zero at the inner point, as shown in figure 5.14c. This inhomogeneous strain may be because the outer WS_2 structure has a free boundary, making it easier to be strained by the lattice mismatch than the inner part with a connecting alloyed interface and a nearly "fixed" boundary condition. After photooxidation, the outer strain is significantly released. As shown in figure 5.14d the strain at the outer point is reduced to be around 0.02 % on Day 20, which is well within the simulation error bars. This strain release may be from degrading processes. The degradation is more significant in the WS_2 part because of its exposed, vulnerable

edges and large structure distortions. Whereas the change in strain is absent and so is oxidation in the MoS_2 part due to protection by the alloyed interface.

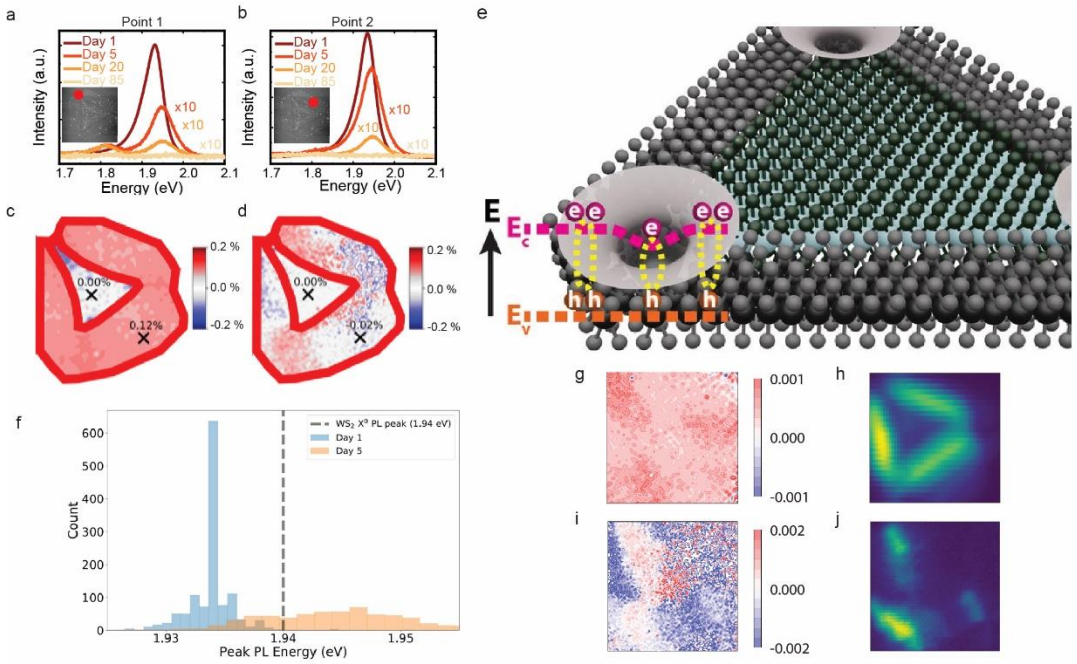

Figure 5.14 Spectral shift and local strain changes in WS_2/MoS_2 monolayer in-plane heterostructure. (a-b) Spectral shift with photooxidation at points 1 and 2 shown in black dots in (c) as a function of time on the WS_2/MoS_2 ML heterostructure. (c) and (d) Spatial strain distribution by fitting energy of local PL emission peaks to ab initio MBPT results corresponding to heterostructure TEPL images on day 1 and day 20, respectively. (e) Schematic plot of the accumulating effect of excitons by strain around a corner of samples.(f) Distribution of energies with peak PL emission for Days 1 and 5. (g) Strain relative to 1.94 eV on Day 1. (h) PL emission at 1.94 eV on Day 1. (i) Strain relative to 1.94 eV on Day 20. (j) PL emission at 1.94 eV on Day 20

We observe from AC-HRSTEM images, alloy interfaces at WS_2 crystal corner regions that are close to sharp corners of the inner monolayer MoS_2 crystal (figure 5.9e). These alloyed corners and interfaces lead to novel effects. First the corner regions show enhanced stability when compared to the side regions of WS_2, as shown in TEPL images on days 5 and 20. These results indicate that the photooxidation of the outer monolayer WS_2 crystals is site selective, and avoids regions close to sharp corners of the inner monolayer MoS_2 crystals. A similar enhanced stability at corner regions are also shown in the TERS image (figure 5.13b), where the intensity of E' mode of ML WS_2 shows preferential higher intensity at corner regions on day 20. A higher intermixing

of MoS_2 and WS_2 into alloys at corner regions is energetically favored and thus thermodynamically stable.

Furthermore, corner regions with enhanced alloy concentration also lead to more local strain due to the atomic size mismatches (atomic radius or bond length). It has been shown that coupling of Mo/W with defects can induce lattice distortions that increase strain. [210] We note that, as shown in figure 5.14a&b, point 1 starts at lower energy on day 1, since the corner regions are at higher strain when compared to side regions in WS_2 before photooxidation (figure 5.14g-j). As the sample degrades, WS_2 outer strain is significantly released, but the corner regions remain with higher strain than the rest. This results in concentrating excitons or charge carriers, as revealed in PL inhomogeneous spatial distribution observed in our experiments. Engineering the band structure of two-dimensional materials by external strain has been demonstrated; [211-215] the origin and modulation of strain in our case however is intrinsic and dynamic due to the role of the alloy interface and the degradation process. The high-strain corner regions act as potential wells that create exciton reservoirs due to electron and exciton funneling effects (see figure 5.14e) [216, 217], allowing localized selective stability of these corner regions, as observed in figure 5.10 hyperspectral TEPL images.

In order to fit and analyze the TEPL spectra of the heterostructure at a corner point (1) and a side point (2) shown in figure 5.14. All three excitonic species X^0, X^-, and XX can be tracked all the way to cryogenic to room temperature at both of these selected points during the photooxidation process, as shown in the deconvoluted spectral fitting in figure 5.15. The relative PL spectral weights of the species shown in table 5-2 reveal a remarkable concentration of trions and biexcitons at day 1 at the corner potential well region (1) compared to the side region (2) on

WS_2. As the sample degrades however, the trion and biexciton concentration decreases, neutral excitons dominate the emission and the spectral weight of trions to neutral excitons (X^-/X^0) decreases, followed by quenching of all excitonic emission as the sample completely oxidizes. This agrees with trends observed by Tongay et al. and others [218, 219] , and suggests an increased defect density. It is worth noting that X^-/X^0 decreased from 1.8 on day 1 to 0.51 on day 5, whereas XX/X^0 decreased much faster from 0.98 to 0.07 in the same time period (table 5-2). Because the distance between the two excitons that make up a biexciton is large (3-4 nm), Coulomb screening can easily be modified by oxidation, so that the spectral weight ratio XX/X^0 can serve as a sensitive gauge of the photooxidation. [220]

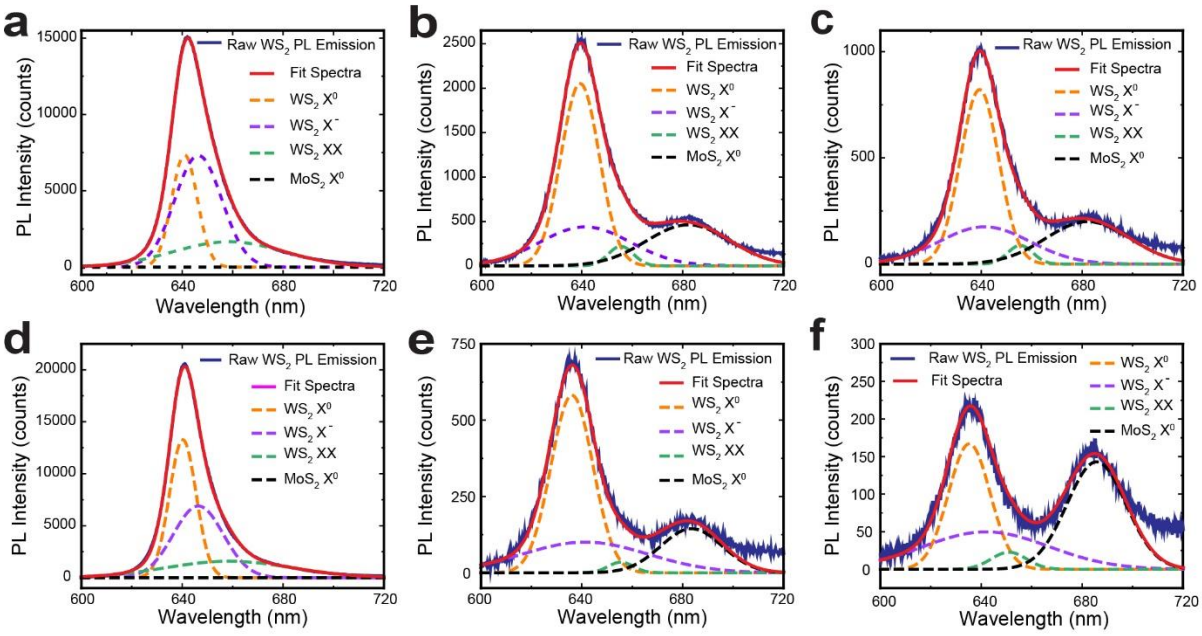

Figure 5.15 All 3 excitonic species (X^0, X^-, and XX) can be tracked to room temperature at both selected points (WS_2 edge and intersection) during the photo-oxidation process. (a) Deconvolved, fit, and raw spectra on Day 1 at Point 1 (intersection). (b) Spectra on Day 5 at Point 1 (c) Spectra on Day 20 at Point 1. (d) Spectra on Day 1 at Point 2 (WS_2 edge). (e) Spectra on Day 5 at Point 2. (f) Spectra on Day 20 at Point 2

Table 5-2. PL intensities and intensity ratios of the various species reveal remarkably higher concentrations of trions and biexcitons on Day 1 at the corner potential well region (Point 1) compared to the WS_2 edge region (Point 2) in addition to significantly higher persistence over time of these species at Point 1.

PL Intensities and Intensity Ratios at Point 1 (Intersection)

	Day 1	Day 5	Day 20
X^0	94052	39075	15636
X^{-1}	170890	19774	7913
XX	92228	2757	1103
MoS_2	0	19298	8360
X^{-1} / X^0	1.8	0.51	0.5
XX / X^0	0.98	0.07	0.07

PL Intensities and Intensity Ratios at Point 2 (Edge)

	Day 1	Day 5	Day 20
X^0	176428	12119	3462
X^{-1}	171292	6301	3121
XX	99230	437	400
MoS_2	0	4415	4197
X^{-1}/X^0	0.97	0.52	0.9
XX/X^0	0.56	0.04	0.12

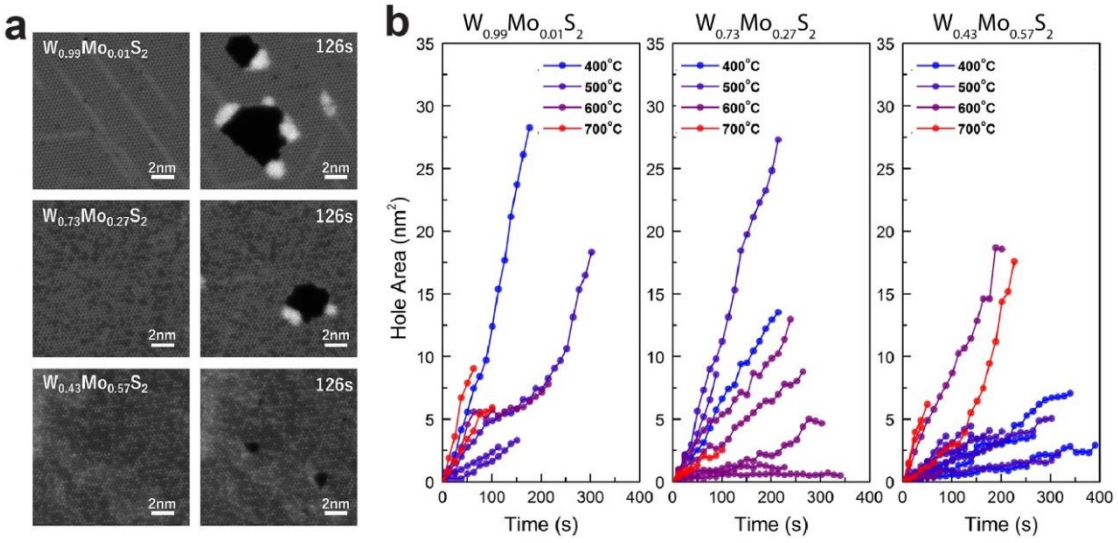

Figure 5.16 In Situ HRSTEM stability analysis of $Mo_xW_{1-x}S_2$ alloys at elevated temperature. (a) HRSTEM images of $Mo_xW_{1-x}S_2$ before and after 126s of continuous scanning at 400 ºC. (b) Time-dependent hole area evolution plot at different test temperatures. The sample with the highest alloying degree ($W_{0.43}Mo_{0.57}S_2$) exhibits the highest thermal stability.

5.3.8 Temperature dependent *In Situ* HRSTEM stability analysis of $Mo_xW_{1-x}S_2$ alloys

The effect of the lateral interface we described above was investigated by limiting the excitation laser power to ~ 400 μW in order to avoid laser-burned holes or similar physical damage to the heterostructure.[199] We further extended our investigation and studied the stability of the $Mo_xW_{1-x}S_2$ alloy at elevated temperature by performing repeated HRSTEM scans at different temperatures and alloy compositions. Under this condition, as the continuous electron beam raster scans the surface, a defect could be initiated as a sulfur vacancy due to the combined effect of electronic excitation and knock-on damage, and then the accumulation of electron beam-generated defects leads to the formation of large holes [221] . Three regions with different alloying composition were scanned by the electron beam at 400 ^oC, and the STEM images shown in figure 5.16a reveal $Mo_xW_{1-x}S_2$ alloys just before defect formation and after 126 s. Regardless of the local alloying composition, large holes are generated after several scans. However, for the W-rich region with low intermixing degree ($W_{0.99}Mo_{0.01}S_2$), holes expanded faster than the other two cases with higher intermixing degree. This observation also indicates the higher thermal stability of the 2D alloy. The *in situ* stability test was also carried out at varied temperatures and temporal changes of the hole area is plotted figure 5.16b. Although some holes expand faster, holes in regions with higher alloying degree expands slower, especially at relatively low temperatures (400-500 ^oC). These results indicate the enormous potential of 2D alloy interfaces and alloyed edges for degradation protection of 2D materials.

5.3.9 Conclusion

Nanoscale alloyed interfaces present a unique platform to stabilize 2D materials over an extended time. We implement integrated TEPL, TERS and s-SNOM techniques based on tapping

mode AFM and perform high-resolution hyperspectral imaging of MoS_2-WS_2 in-plane ML heterostructures exhibiting nanoscale alloy interfaces. The ambient oxidation process, accelerated by the probe laser, begins from the outer ML and is mainly induced by the S vacancies in WS_2. The evolution of the degradation is however hampered by the alloy nano-interface region from propagating towards the inner MoS_2 ML of the sample. Eventually, the outer ML completely oxidizes, changing from WS_2 into W-based oxides while the inner MoS_2 exhibits extended stability due to protection by the interface. *In-situ* HRSTEM imaging showed that alloying leads to high stability of 2D materials even at elevated temperatures. The oxidation process causes significant non-uniform changes in the topography and permittivity of the heterostructure. These processes not only cause quenching of neutral and charged exciton emissions, but also induce complex interactions among them that are manifested in neutral exciton, trion and biexciton energy shifts. Notably, the 2D alloy interface coupled with intrinsic strain cause spatial inhomogeneity of the oxidation and emission of the various excitonic species, providing localized potential wells at corner interfaces for various charge carriers and enabling localized emission with enhanced stability. We envision our studies offer a deeper understanding of 2D alloys as a rich platform to engineer stable optoelectronic devices based on 2D heterostructures with enhanced performance.

5.3.10 Materials and methods:

5.3.10.1 The growth of in-plane MoS_2-WS_2 heterostructures

To synthesize in-plane MoS_2-WS_2 heterostructures, powders of ammonium metatungstate hydrate ($(NH_4)_6H_2W_{12}O_{40}$, 50 mg), ammonium heptamolybdate ($(NH_4)_6Mo_7O_{24}$, 5 mg) and sodium cholate hydrate ($C_{24}H_{39}NaO_5 \cdot xH_2O$, 200 mg) were dissolved in 10 mL of deionized water. The solution was then spin-coated onto a clean SiO_2/Si wafer, followed by a single-step high-temperature

heating treatment in the chemical vapor deposition (CVD) furnace in the presence of sulfur vapor. During the heating process, the furnace was first ramped to 700 °C and held for 10 min, and subsequently ramped to 800 °C and held for another 10 min. An argon flow of 100 sccm was used as the carrier gas during synthesis.

5.3.10.2 AC-HRSTEM

As-grown MoS_2-WS_2 heterostructures and $Mo_xW_{1-x}S_2$ alloys was transferred either onto Quantifoil gold grid or *in situ* heating chip (E-AHBC) for Aduro holder (Protochips), using conventional PMMA-based wet chemical transfer (for Quantifoil grid) and PMMA-based deterministic transfer (for *in situ* heating chip). [222] For imaging, FEI Titan^3 G2 S/TEM 60-300 operated at 80 kV and high angle annular dark field (HAADF) detector was used. Lower voltage was used at high resolution to decrease irradiation damage. To enhance visibility and reduce noise in STEM images, all acquired high-resolution images were processed by Gaussian Blur filter (radius = 0.03 nm) using ImageJ software.

5.3.10.3 Integrated s-SNOM/TEPL/TERS nanoscope.

In the multimodal nanoscope experimental setup (neaspec co.) the sample is excited by a collimated Continues Wave (CW) green laser (532 nm wavelength). A parabolic mirror with an NA of 0.4 focuses the excitation laser to a commercial PtIr-coated cantilevered Si tips with a vertical oscillation frequency of 240 kHz and amplitude of ~20 nm. Standard near-field retraction curve and near-field nanoimaging is performed by detecting the backscattered near-field via a combination of phase interferometric detection and demodulation of the detector signal at the fourth harmonic (4Ω) of the tip oscillation frequency. The s-SNOM amplitude approach curves

(figure 5.17a) are acquired by measuring the demodulated detector signals as a function of the tip–sample distance at higher harmonic of the tip tapping frequency. This signal is maximum at small tip–sample distances and decreases rapidly as the tip is pulled away from the sample due to effective signal demodulation, which guarantees precise alignment of the excitation laser to the tip. Near-field approach curves (figure 5.17a) were recorded routinely before either TEPL/TERS spectra or near-field images are taken.

For TERS/TEPL measurements, the MoS2–WS2 lateral heterostructure sample is excited by the laser and the forward scattered emission is collected by the parabolic mirror of the s-SNOM and dispersed using a 328 mm focal length Andor spectrometer and imaged with liquid nitrogen cooled silicon EMCCD camera (Andor iXon). The tip–sample distance dependence of the TEPL/TERS signal of the ML heterostructure MoS2–WS2 is always checked before any measurement (Figure 5.17b). To obtain normalized TEPL spectra, the tip is retracted from the sample flake to record a reference spectrum. Then, a spectrum is taken on the sample surface while the tip is engaged. A normalized spectrum is achieved by subtracting the reference spectra from the spectra taken on the sample (see figure 5.18).

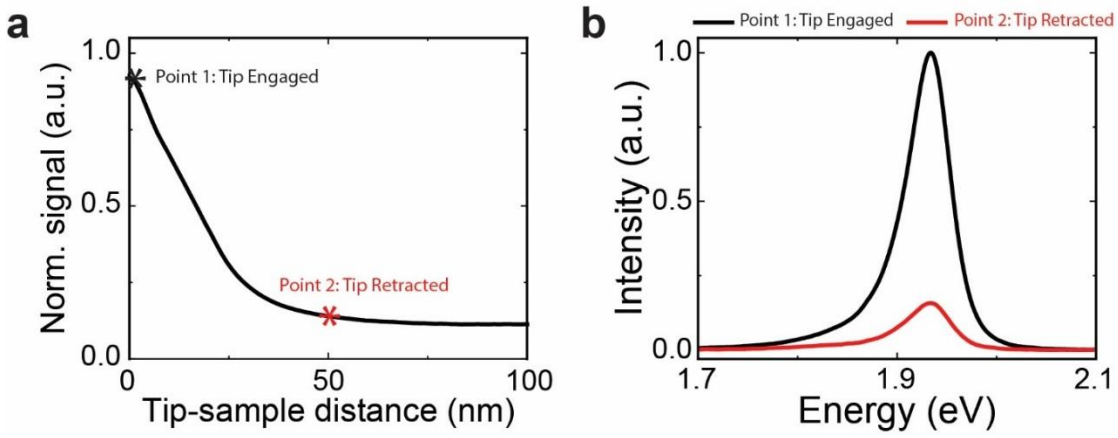

Figure 5.17 Near-field signal and TEPL intensity dependence to tip-sample distance. (a) 4th harmonic near-field amplitude approach curve and (b) WS_2 TEPL intensity with tip engaged and retracted.

For hyperspectral TEPL/TERS nanoimaging, the normalized spectra at each pixel (x, y) of a 2D area of the sample surface was recorded. As shown in figure 5.9, spectra have taken in the presence and absence of the tip. The high-resolution image is only achieved when these two images are subtracted. The capability to provide spatial and spectral information simultaneously with spatial resolution limited only by the apex radius of the probe tip (typically ~20 nm) marks the extraordinary advantage of TEPL/TERS hyperspectral nanoimaging. We note that, in figure 5.10, in order to obtain a large-scale image of the whole flake, we used a large pixel size which led to large blurred features. An additional advantage of this hybrid s-SNOM and TEPL/TERS nano-imaging setup is the ability to easily and routinely align the excitation beam guided by near-field approach curves.

The samples were CVD-grown pristine WS_2 and MoS_2 MLs (synthesized under identical experimental conditions as the heterostructure samples used in the manuscript, see figure 5.11 a&b for topography). We took four hyperspectral 3D data cubes (2 data cubes for each sample, one with tip engaged and one with tip retracted), at 500 nm/pixel (i.e. 20x20 μm using 40x40 pixels for MoS_2 and at 32x32 μm using 64x64pixels for WS_2) at identical experimental conditions. In

order to obtain the normalized TEPL hyperspectral 3D data cube, first the tip is retracted from the sample flake to record a reference spectrum (t_r image shown in figure 5.11). Subsequently, a spectrum is taken on the sample surface while the tip is engaged (t_e image shown in figure 5.11). A normalized spectrum (t_e-t_r image shown in figure 5.11) is recorded by subtracting the reference spectra from the spectra taken on the sample. From the normalized 3D hyperspectral image, we took a cross-section cut of TEPL map close to the bandgap of WS_2 or MoS_2. figure 5.11 show the degradation comparison of pristine MoS_2 (figure 5.11 c) and pristine WS_2 (figure 5.11 d) monolayers identically exposed to extended periods of laser light in order to accelerate degradation. For identical degradation conditions both pristine MoS_2 and WS_2 flakes degrade identically and similar periods of time (in three steps over a period of a week). figure 5.11 c&d show a sample of how normalized TEPL images have been achieved by subtracting the reference image from the image taken on the sample at the same energy cross-section. Although there are slight differences in degradation between flakes, overall the degradation in both monolayers, exposed to similar laser exposure, occur from the edge towards the center in a similar amount of time.

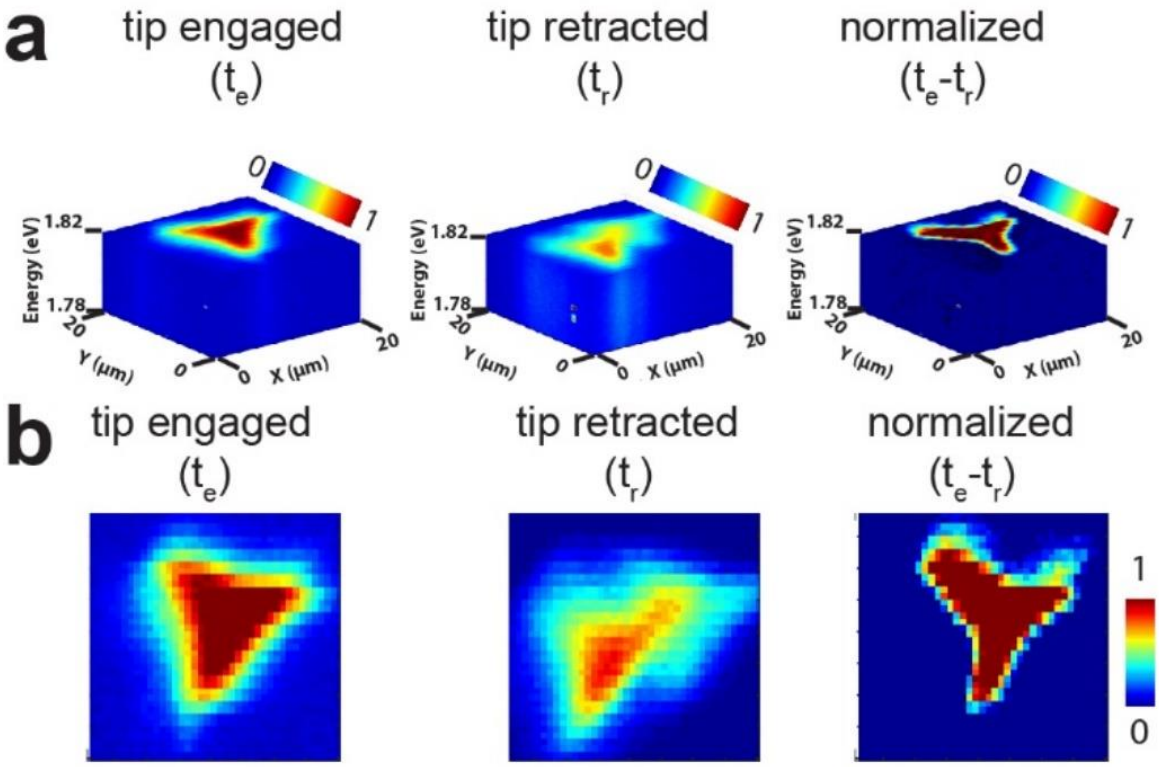

Figure 5.18 Hyperspectral TEPL data showing extraction of normalized TEPL spectra in monolayer MoS_2. (a) TEPL hyperspectral 3D data cubes and (b) cross-section cut of TEPL maps taken at 1.81 eV taken on the sample surface while the tip is engaged (t_e), tip is retracted (t_r), and normalized spectra (t_e -t_r). (b).

CHAPTER 6
6.Summary and Outlook

In this dissertation, we utilized nano-imaging and nono-spectroscopy methods to study several layered materials and fundamental aspects of phonon polaritons propagation.

The permittivity of the layered muscovite mica has been studied by ellipsometry and nano-FTIR. It has been shown that mica is a hyperbolic material with weak polaritonic behavior. Also, it has been shown that results from the extended finite model agree with experiments only when the out-of-plane dielectric function is taken into account.

Spectroscopy and nanoimaging of Black Phosphorous (BP) and Violet Phosphorous (VP) show that both materials degrade when exposed to air. The nano-FTIR results confirm degradation with the combination of many overlapping phosphorus oxides and phosphoric acids species modes in the range of 850–1300 cm^{-1}. However, VP degrades slower than BP due to reduced oxygen insertion.

It has also been shown that the nanoscale alloyed interface between MOCVD-grown monolayer MoS_2 and WS_2 can serve as a protecting layer to stabilize the inner material and protect it from degradation. Also, it has been shown that focused beam laser can accelerate degradation of MoS_2 and WS_2.

We show that polariton wavelength strongly depends on the dielectric function of the substrate. Polaritons can propagate within the hBN from the domain boundaries between the metallic and dielectric domains of the VO_2 (substrate).

7. REFERENCES

1. Abbe, E., *Beiträge zur Theorie des Mikroskops und der mikroskopischen Wahrnehmung.* Archiv für mikroskopische Anatomie, 1873. **9**(1): p. 413-468.
2. Weisenburger, S. and V. Sandoghdar, *Light microscopy: an ongoing contemporary revolution.* Contemporary Physics, 2015. **56**(2): p. 123-143.
3. Airy, G.B., *On the diffraction of an object-glass with circular aperture.* Transactions of the Cambridge Philosophical Society, 1835. **5**: p. 283.
4. Binnig, G. and H. Rohrer, *Scanning tunneling microscopy---from birth to adolescence.* Reviews of Modern Physics, 1987. **59**(3): p. 615-625.
5. Binnig, G., C.F. Quate, and C. Gerber, *Atomic Force Microscope.* Physical Review Letters, 1986. **56**(9): p. 930-933.
6. Synge, E.H., *XXXVIII. A suggested method for extending microscopic resolution into the ultra-microscopic region.* The London, Edinburgh, and Dublin Philosophical Magazine and Journal of Science, 1928. **6**(35): p. 356-362.
7. Ash, E.A. and G. Nicholls, *Super-resolution Aperture Scanning Microscope.* Nature, 1972. **237**(5357): p. 510-512.
8. Lewis, A., et al., *Development of a 500 Å spatial resolution light microscope: I. light is efficiently transmitted through λ/16 diameter apertures.* Ultramicroscopy, 1984. **13**(3): p. 227-231.
9. Hui, R., *Chapter 2 - Optical fibers*, in *Introduction to Fiber-Optic Communications*, R. Hui, Editor. 2020, Academic Press. p. 19-76.
10. Vobornik, D. and S. Vobornik, *Scanning near-field optical microscopy.* Bosnian journal of basic medical sciences, 2008. **8**(1): p. 63-71.
11. Denk, W. and D.W. Pohl, *Near-field optics: Microscopy with nanometer-size fields.* Journal of Vacuum Science & Technology B: Microelectronics and Nanometer Structures Processing, Measurement, and Phenomena, 1991. **9**(2): p. 510-513.
12. Specht, M., et al., *Scanning plasmon near-field microscope.* Physical Review Letters, 1992. **68**(4): p. 476-479.
13. Inouye, Y. and S. Kawata, *Near-field scanning optical microscope with a metallic probe tip.* Optics Letters, 1994. **19**(3): p. 159-161.
14. Zenhausern, F., M.P. O'Boyle, and H.K. Wickramasinghe, *Apertureless near-field optical microscope.* Applied Physics Letters, 1994. **65**(13): p. 1623-1625.
15. Zenhausern, F., Y. Martin, and H.K. Wickramasinghe, *Scanning Interferometric Apertureless Microscopy: Optical Imaging at 10 Angstrom Resolution.* Science, 1995. **269**(5227): p. 1083-1085.
16. Hillenbrand, R. and F. Keilmann, *Material-specific mapping of metal/semiconductor/dielectric nanosystems at 10 nm resolution by backscattering near-field optical microscopy.* Applied Physics Letters, 2002. **80**(1): p. 25-27.
17. Abate, Y., et al., *Nanoscopy of Phase Separation in InxGa1–xN Alloys.* ACS Applied Materials & Interfaces, 2016. **8**(35): p. 23160-23166.

18. Abate, Y., et al., *Nanoscopy reveals surface-metallic black phosphorus.* Light Sci Appl., 2016. **5**: p. e16162.
19. Abate, Y., et al., *TOWARDS UNDERSTANDING AND CONTROL OF NANOSCALE PHASE SEGREGATION IN INDIUM-GALLIUM-NITRIDE ALLOYS*, in *III-Nitride Materials, Devices and Nano-Structures*. p. 183-207.
20. Hillenbrand, R., T. Taubner, and F. Keilmann, *Phonon-enhanced light–matter interaction at the nanometre scale.* Nature, 2002. **418**(6894): p. 159-162.
21. Taminiau, T.H., et al., *λ/4 Resonance of an Optical Monopole Antenna Probed by Single Molecule Fluorescence.* Nano Letters, 2007. **7**(1): p. 28-33.
22. Hillenbrand, R. and F. Keilmann, *Complex Optical Constants on a Subwavelength Scale.* Physical Review Letters, 2000. **85**(14): p. 3029-3032.
23. Keilmann, F. and R. Hillenbrand, *Near-field microscopy by elastic light scattering from a tip.* Philosophical Transactions of the Royal Society of London, Series A, 2004. **362**: p. 787-805.
24. Hillenbrand, R., M. Stark, and R. Guckenberger, *Higher-harmonics generation in tapping-mode atomic-force microscopy: Insights into the tip–sample interaction.* Applied Physics Letters, 2000. **76**(23): p. 3478-3480.
25. HillenbRand, R., B. Knoll, and F. Keilmann, *Pure optical contrast in scattering-type scanning near-field microscopy.* Journal of Microscopy, 2001. **202**(1): p. 77-83.
26. Richards, D., et al., *Near-field microscopy by elastic light scattering from a tip.* Philosophical Transactions of the Royal Society of London. Series A: Mathematical, Physical and Engineering Sciences, 2004. **362**(1817): p. 787-805.
27. Ocelic, N., A. Huber, and R. Hillenbrand, *Pseudoheterodyne detection for background-free near-field spectroscopy.* Applied Physics Letters, 2006. **89**(10): p. 101124.
28. Stiegler, J.M., et al., *Nanoscale Infrared Absorption Spectroscopy of Individual Nanoparticles Enabled by Scattering-Type Near-Field Microscopy.* ACS Nano, 2011. **5**(8): p. 6494-6499.
29. Fali, A., et al., *Nanoscale Spectroscopy of Dielectric Properties of Mica.* ACS Photonics, 2021. **8**(1): p. 175-181.
30. Fali, A., M. Snure, and Y. Abate, *Violet phosphorus surface chemical degradation in comparison to black phosphorus.* Applied Physics Letters, 2021. **118**(16): p. 163105.
31. Gamage, S., et al., *Probing structural changes in single enveloped virus particles using nano-infrared spectroscopic imaging.* PloS one, 2018. **13**(6): p. e0199112-e0199112.
32. Raman, C.V. and K.S. Krishnan, *A New Type of Secondary Radiation.* Nature, 1928. **121**(3048): p. 501-502.
33. Kusch, P., et al., *Combined Tip-Enhanced Raman Spectroscopy and Scattering-Type Scanning Near-Field Optical Microscopy.* The Journal of Physical Chemistry C, 2018. **122**(28): p. 16274-16280.
34. Lee, H., et al., *Tip-enhanced photoluminescence nano-spectroscopy and nano-imaging.* Nanophotonics, 2020. **9**(10): p. 3089-3110.
35. Thomas, S., et al., *Probing of Optical Near-Fields by Electron Rescattering on the 1 nm Scale.* Nano Letters, 2013. **13**(10): p. 4790-4794.
36. Koo, Y., et al., *Tip-Induced Nano-Engineering of Strain, Bandgap, and Exciton Funneling in 2D Semiconductors.* Advanced Materials, 2021. **33**(17): p. 2008234.

37. Yeo, B.-S., et al., *Tip-enhanced Raman Spectroscopy – Its status, challenges and future directions.* Chemical Physics Letters, 2009. **472**(1): p. 1-13.
38. Yang, Z., J. Aizpurua, and H. Xu, *Electromagnetic field enhancement in TERS configurations.* Journal of Raman Spectroscopy, 2009. **40**(10): p. 1343-1348.
39. Park, K.-D., et al., *Radiative control of dark excitons at room temperature by nano-optical antenna-tip Purcell effect.* Nature Nanotechnology, 2018. **13**(1): p. 59-64.
40. Alajlan, A.M., et al., *Gap-mode enhancement on MoS2 probed by functionalized tip-enhanced Raman spectroscopy.* Applied Physics Letters, 2016. **109**(13): p. 133106.
41. Schmid, T., et al., *Nanoscale Chemical Imaging Using Tip-Enhanced Raman Spectroscopy: A Critical Review.* Angewandte Chemie International Edition, 2013. **52**(23): p. 5940-5954.
42. Fali, A., et al., *Photodegradation Protection in 2D In-Plane Heterostructures Revealed by Hyperspectral Nanoimaging: The Role of Nanointerface 2D Alloys.* ACS Nano, 2021. **15**(2): p. 2447-2457.
43. Knoll, B. and F. Keilmann, *Enhanced dielectric contrast in scattering-type scanning near-field optical microscopy.* Optics Communications, 2000. **182**(4): p. 321-328.
44. Aghamiri, N.A., et al., *Hyperspectral time-domain terahertz nano-imaging.* Optics Express, 2019. **27**(17): p. 24231-24242.
45. Huth, F., et al., *Nano-FTIR Absorption Spectroscopy of Molecular Fingerprints at 20 nm Spatial Resolution.* Nano Letters, 2012. **12**(8): p. 3973-3978.
46. Govyadinov, A.A., et al., *Quantitative Measurement of Local Infrared Absorption and Dielectric Function with Tip-Enhanced Near-Field Microscopy.* The Journal of Physical Chemistry Letters, 2013. **4**(9): p. 1526-1531.
47. Cvitkovic, A., N. Ocelic, and R. Hillenbrand, *Analytical model for quantitative prediction of material contrasts in scattering-type near-field optical microscopy.* Optics Express, 2007. **15**(14): p. 8550-8565.
48. Zhang, L.M., et al., *Near-field spectroscopy of silicon dioxide thin films.* Physical Review B, 2012. **85**(7): p. 075419.
49. Mester, L., et al., *Subsurface chemical nanoidentification by nano-FTIR spectroscopy.* Nature Communications, 2020. **11**(1): p. 3359.
50. Hauer, B., A.P. Engelhardt, and T. Taubner, *Quasi-analytical model for scattering infrared near-field microscopy on layered systems.* Optics Express, 2012. **20**(12): p. 13173-13188.
51. Mastel, S., et al., *Nanoscale-resolved chemical identification of thin organic films using infrared near-field spectroscopy and standard Fourier transform infrared references.* Applied Physics Letters, 2015. **106**(2): p. 023113.
52. McLeod, A.S., et al., *Model for quantitative tip-enhanced spectroscopy and the extraction of nanoscale-resolved optical constants.* Physical Review B, 2014. **90**(8): p. 085136.
53. Dai, S., et al., *Subdiffractional focusing and guiding of polaritonic rays in a natural hyperbolic material.* Nature Communications, 2015. **6**(1): p. 6963.
54. Shekhar, P., J. Atkinson, and Z. Jacob, *Hyperbolic metamaterials: fundamentals and applications.* Nano Convergence, 2014. **1**(1): p. 14.
55. Poddubny, A., et al., *Hyperbolic metamaterials.* Nature Photonics, 2013. **7**(12): p. 948-957.

56. Yoxall, E., et al., *Direct observation of ultraslow hyperbolic polariton propagation with negative phase velocity.* Nature Photonics, 2015. **9**(10): p. 674-678.
57. Dai, S., et al., *Tunable Phonon Polaritons in Atomically Thin van der Waals Crystals of Boron Nitride.* Science, 2014. **343**(6175): p. 1125-1129.
58. Fali, A., et al., *Refractive Index-Based Control of Hyperbolic Phonon-Polariton Propagation.* Nano Letters, 2019. **19**(11): p. 7725-7734.
59. Folland, T.G., et al., *Reconfigurable infrared hyperbolic metasurfaces using phase change materials.* Nat. Commun., 2018. **9**: p. 4371.
60. Yu, N. and F. Capasso, *Flat optics with designer metasurfaces.* Nature Materials, 2014. **13**: p. 139-150.
61. Staude, I. and J. Schilling, *Metamaterial-inspired silicon nanophotonics.* Nature Photonics, 2017. **11**(5): p. 274-284.
62. Kildishev, A.V., A. Boltasseva, and V.M. Shalaev, *Planar photonics with metasurfaces.* Science (Washington), 2013. **339**(12): p. 1232009.
63. Meinzer, N., W.L. Barnes, and I.R. Hooper, *Plasmonic meta-atoms and metasurfaces.* Nature Photonics, 2014. **8**(12): p. 889-898.
64. Khurgin Jacob, B., *Relative merits of phononics vs. plasmonics: the energy balance approach.* Nanophotonics, 2018. **7**(1): p. 305.
65. Wuttig, M., H. Bhaskaran, and T. Taubner, *Phase-change materials for non-volatile photonic applications.* Nature Photonics, 2017. **11**(8): p. 465-476.
66. Yang, Z. and S. Ramanathan, *Breakthroughs in Photonics 2014: Phase Change Materials for Photonics.* IEEE Photonics Journal, 2015. **7**(3): p. 1-5.
67. Abate, Y., et al., *Control of plasmonic nanoantennas by reversible metal-insulator transition.* Scientific Reports, 2015. **5**: p. 8.
68. Liu, M., A.J. Sternbach, and D.N. Basov, *Nanoscale electrodynamics of strongly correlated quantum materials.* Reports on Progress in Physics, 2017. **80**(1): p. 27.
69. McGahan, C., et al., *Geometric constraints on phase coexistence in vanadium dioxide single crystals.* Nanotechnology, 2017. **28**(8): p. 085701-085701.
70. Qazilbash, M.M., et al., *Mott Transition in VO-$_2$ Revealed by Infrared Spectroscopy and Nano-Imaging.* Science, 2007. **318**(5857): p. 1750.
71. Li, P., et al., *Reversible optical switching of highly confined phonon–polaritons with an ultrathin phase-change material.* Nature Materials, 2016. **15**: p. 870-875.
72. Yin, X.H., et al., *Beam switching and bifocal zoom lensing using active plasmonic metasurfaces.* Light-Science & Applications, 2017. **6**: p. 7.
73. Karvounis, A., et al., *All-dielectric phase-change reconfigurable metasurface.* Applied Physics Letters, 2016. **109**(5): p. 051103.
74. Guo, P.J., et al., *Conformal Coating of a Phase Change Material on Ordered Plasmonic Nanorod Arrays for Broadband All-Optical Switching.* Acs Nano, 2017. **11**(1): p. 693-701.
75. Kats, M.A., et al., *Ultra-thin perfect absorber employing a tunable phase change material.* Applied Physics Letters, 2012. **101**(22): p. 221101.
76. Giles, A.J., et al., *Ultralow-loss polaritons in isotopically pure boron nitride.* Nature Materials, 2018. **17**(2): p. 134-139.
77. Vuong, T., et al., *Isotope engineering of van der Waals interactions in hexagonal boron nitride.* Nature materials, 2018. **17**(2): p. 152.

78. Poddubny, A., et al., *Hyperbolic metamaterials.* Nature Photonics, 2013. **7**: p. 948-957.
79. Dai, S., et al., *Tunable phonon polaritons in atomically thin van der Waals crystals of boron nitride.* Science (Washington), 2014. **343**(6175): p. 1125-1129.
80. Caldwell, J.D., et al., *Sub-diffractional, Volume-confined Polaritons in the Natural Hyperbolic Material Hexagonal Boron Nitride.* Nature Communications, 2014. **5**: p. 5221.
81. Duan, J., et al., *Launching phonon polaritons by natural boron nitride wrinkles with modifiable dispersion by dielectric environments.* Advanced Materials, 2017. **29**(38): p. 1702494.
82. Vakil, A. and N. Engheta, *Transformation Optics Using Graphene.* Science (Washington), 2011. **332**: p. 1291-1294.
83. Yang, X., et al., *Experimental realization of three-dimensional indefinite cavities at the nanoscale with anomalous scaling laws.* Nature Photonics, 2012. **6**: p. 450-453.
84. Dai, S., et al., *Manipulation and Steering of Hyperbolic Surface Polaritons in Hexagonal Boron Nitride.* Advanced Materials, 2018: p. 1706358-1706358.
85. Li, P., et al., *Infrared hyperbolic metasurface based on nanostructured van der Waals materials.* Science, 2018. **359**(6378): p. 892-896.
86. Zebo, Z., et al., *Highly Confined and Tunable Hyperbolic Phonon Polaritons in Van Der Waals Semiconducting Transition Metal Oxides.* Advanced Materials, 2018. **30**(13): p. 1705318.
87. Fei, Z., et al., *Gate-tuning of graphene plasmons revealed by infrared nano-imaging.* Nature 2012. **487**: p. 82-85.
88. Chen, J., et al., *Optical nano-imaging of gate-tunable graphene plasmons.* Nature, 2012. **487**: p. 77-81.
89. Dai, S., et al., *Efficiency of Launching Highly Confined Polaritons by Infrared Light Incident on a Hyperbolic Material.* Nano Letters, 2017. **17**(9): p. 5285-5290.
90. Dai, S., et al., *Subdiffractional focusing and guiding of polaritonic rays in a natural hyperbolic material.* Nature Communications, 2015. **6**: p. 6963.
91. Li, P., et al., *Hyperbolic Phonon-Polaritons in Boron Nitride for near-field optical imaging and focusing.* Nature Communications, 2015. **6**: p. 7507.
92. Alonso-González, P., et al., *Controlling graphene plasmons with resonant metal antennas and spatial conductivity patterns.* Science, 2014. **344**(6190): p. 1369-1373.
93. Yu, N., et al., *Light Propagation with Phase Discontinuities: Generalized Laws of Reflection and Refraction.* Science, 2011. **334**(6054): p. 333.
94. Brown, L.V., et al., *Nanoscale Mapping and Spectroscopy of Nonradiative Hyperbolic Modes in Hexagonal Boron Nitride Nanostructures.* Nano Letters, 2018. **18**(3): p. 1628-1636.
95. Chen, Z., et al., *Self-Assembled, Nanostructured, Tunable Metamaterials via Spinodal Decomposition.* ACS Nano, 2016. **10**(11): p. 10237-10244.
96. Takahashi, T., H. Itoh, and A. Takeuchi, *Chemical vapor deposition of hexagonal boron nitride thick film on iron.* Journal of Crystal Growth, 1979. **47**(2): p. 245-250.
97. Autore, M., et al., *Boron nitride nanoresonators for phonon-enhanced molecular vibrational spectroscopy at the strong coupling limit.* Light: Science &Amp; Applications, 2018. **7**: p. 17172.

98. Kats, M.A., *Optics at interfaces: ultra-thin color coatings, perfect absorbers, and metasurfaces,* in *Engineering and Applied Sciences*. 2014, Harvard University.
99. Kremers, S., *Optical properties of phase change materials for novel optical and electrical storage applications*, in *Physics*. 2009, RWTH Aachen.
100. Folland, T.G., et al., *Probing Polaritons in the Mid- to Far-Infrared.* Journal of Applied Physics, 2019. **125**: p. 191102.
101. Giles, A.J., et al., *Ultralow-loss polaritons in isotopically pure boron nitride.* Nat. Mater., 2018. **17**: p. 134-139.
102. Ambrosio, A., et al., *Selective excitation and imaging of ultraslow phonon polaritons in thin hexagonal boron nitride crystals.* Light: Science & Applications, 2018. **7**: p. 27.
103. Dai, S., et al., *Phase-Change Hyperbolic Heterostructures for Nanopolaritonics: A Case Study of hBN/VO_2.* Advanced Materials, 2019. **31**(18): p. 1900251.
104. Dai, S., et al., *Hyperbolic Phonon Polaritons in Suspended Hexagonal Boron Nitride.* Nano Letters, 2019. **19**: p. 1009.
105. Kim, K.S., et al., *The Effect of Adjacent Materials on the Propagation of Phonon Polaritons in Hexagonal Boron Nitride.* J. Phys. Chem. Lett., 2017. **8**(13): p. 2902-2908.
106. Ciano, C., et al., *Observation of phonon-polaritons in thin flakes of hexagonal boron nitride on gold.* Applied Physics Letters, 2018. **112**: p. 153101.
107. Caldwell, J.D., et al., *Photonics with hexagonal boron nitride.* Nat. Rev. Mater., 2019. **4**(8): p. 552-567.
108. Yang, H.U., et al., *Optical dielectric function of silver.* Phys. Rev. B: Condens. Matter Mater. Phys., 2015. **91**(23): p. 235137.
109. Caldwell, J.D., et al., *Low-Loss, Infrared and Terahertz Nanophotonics with Surface Phonon Polaritons.* Nanophotonics, 2015. **4**: p. 44-68.
110. Wan, C., et al., *On the Optical Properties of Thin-Film Vanadium Dioxide from the Visible to the Far Infrared.* Annalen der Physik, 2019. **531**(10): p. 1900188.
111. Winsemius, P., et al., *Temperature dependence of the optical properties of Au, Ag and Cu.* . J. Phys. F: Met. Phys., 1976. **6**(8): p. 1583-1606.
112. Johnson, P.B. and R.W. Christy, *Optical Constants of the Noble Metals.* Phys. Rev. B: Condens. Matter Mater. Phys., 1972. **6**(12): p. 4370-4379.
113. Abelès, F., *Optical Properties and Electronic Structure of Metals and Alloys: Proceedings of the International Colloquim*. **1966**: Amsterdam, North-Holland Pub. Co.; New York, Wiley, Interscience Publishers Division
114. Kischkat, J., et al., *Mid-infrared optical properties of thin films of aluminum oxide, titanium dioxide, silicon dioxide, aluminum nitride and silicon nitride.* Applied Optics, 2012. **51**(28): p. 6789.
115. Snyder, A.W. and J.D. Love, *Goos-Hanchen Shift.* Applied Optics, 1976. **15**(1): p. 236-238.
116. Lee, S., et al., *Anomalously low electronic thermal conductivity in metallic vanadium dioxide.* Science, 2017. **355**(6323): p. 371-374.
117. Poddubny, A., et al., *Hyperbolic metamaterials.* Nat. Photonics, 2013. **7**: p. 948-957.
118. Folland, T.G. and J.D. Caldwell, *Precise Control of Infrared Polarization Using Crystal Vibrations.* Nature, 2018. **562**(7728): p. 499-501.

119. Chaudhary, K., et al., *Polariton nanophotonics using phase-change materials.* Nat. Commun., 2019. **10**(1): p. 4487.
120. Caldwell, J.D., et al., *Sub-diffractional volume-confined polaritons in the natural hyperbolic material hexagonal boron nitride.* Nat. Commun., 2014. **5**: p. 5221.
121. Autore, M., et al., *Boron nitride nanoresonators for phonon-enhanced molecular vibrational spectroscopy at the strong coupling limit.* Light: Science & Applications, 2018. **7**: p. 17172.
122. Neuner, B., et al., *Midinfrared Index Sensing of pL-Scale Analytes Based on Surface Phonon Polaritons in Silicon Carbide.* J. Phys. Chem. C., 2010. **114**(16): p. 7489-7491.
123. Osawa, M., *Surface-enhanced infrared absorption*, in *Near-Field Optics and Surface Plasmon Polaritons*. **2001**, Springer Berlin p. 163-187.
124. Berte, R., et al., *Sub-nanometer thin oxide film sensing with localized surface phonon polaritons.* ACS Photonics, 2017. **5**(7): p. 2807-2815.
125. Giles, A.J., et al., *Ultra-low-loss Polaritons in Isotopically Pure boron nitride.* Nature Materials, 2018. **17**: p. 134-139.
126. Hoffman, T.B., et al., *Optimization of Ni-Cr Flux Growth for Hexagonal Boron Nitride Single Crystals* Journal of Crystal Growth, 2014. **393**: p. 114-118.
127. McGahan, C., et al., *Geometric constraints on phase coexistence in vandium dioxide single crystals* Nanotechnology, 2017. **28**: p. 085701.
128. Geim, A.K. and K.S. Novoselov, *The rise of graphene.* Nature Materials, 2007. **6**(3): p. 183-191.
129. Xu, M., et al., *Graphene-Like Two-Dimensional Materials.* Chemical Reviews, 2013. **113**(5): p. 3766-3798.
130. Jariwala, D., et al., *Emerging Device Applications for Semiconducting Two-Dimensional Transition Metal Dichalcogenides.* ACS Nano, 2014. **8**(2): p. 1102-1120.
131. Rickwood, P.C., *The largest crystals.* American Mineralogist, 1981. **66**(9-10): p. 885-907.
132. de Poel, W., et al., *Muscovite mica: Flatter than a pancake.* Surface Science, 2014. **619**: p. 19-24.
133. Jia, F. and S. Song, *Preparation of monolayer muscovite through exfoliation of natural muscovite.* RSC Advances, 2015. **5**(65): p. 52882-52887.
134. Castellanos-Gomez, A., et al., *Atomically Thin Mica Flakes and Their Application as Ultrathin Insulating Substrates for Graphene.* Small, 2011. **7**(17): p. 2491-2497.
135. Osman, M.A., W.R. Caseri, and U.W. Suter, *H+/Li+and H+/K+Exchange on Delaminated Muscovite Mica.* Journal of Colloid and Interface Science, 1998. **198**(1): p. 157-163.
136. de Poel, W., et al., *Metal ion-exchange on the muscovite mica surface.* Surface Science, 2017. **665**: p. 56-61.
137. Akutagawa, T., et al., *Formation of oriented molecular nanowires on mica surface.* Proceedings of the National Academy of Sciences, 2002. **99**(8): p. 5028-5033.
138. Kankate, L., et al., *From clusters to fibers: Parameters for discontinuous para-hexaphenylene thin film growth.* The Journal of Chemical Physics, 2008. **128**(8): p. 084709.
139. de Poel, W., et al., *Dibenzo Crown Ether Layer Formation on Muscovite Mica.* Langmuir, 2014. **30**(42): p. 12570-12577.

140. Pintea, S., et al., *Solid–Liquid Interface Structure of Muscovite Mica in CsCl and RbBr Solutions.* Langmuir, 2016. **32**(49): p. 12955-12965.
141. Simbrunner, C., et al., *Color Tuning of Nanofibers by Periodic Organic–Organic Hetero-Epitaxy.* ACS Nano, 2012. **6**(6): p. 4629-4638.
142. Crow, M.L., *Characterization of mica crystals as reflectors for an ultracold neutron doppler converter.* Physica B: Condensed Matter, 1997. **241-243**: p. 110-112.
143. Li, L., et al., *Epitaxy-Assisted Creation of PCBM Nanocrystals and Its Application in Constructing Optimized Morphology for Bulk-Heterojunction Polymer Solar Cells.* The Journal of Physical Chemistry B, 2008. **112**(49): p. 15651-15658.
144. Jellison, G.E., *Data analysis for spectroscopic ellipsometry.* Thin Solid Films, 1993. **234**(1): p. 416-422.
145. Tompkins, H.G. and E.A. Irene, *Handbook of Ellipsometry*. Handbook of Ellipsometry. 2005. 3-540.
146. Jellison, G.E., *Data Analysis for Spectroscopic Ellipsometry*, in *Handbook of Ellipsometry*, H.G. Tompkins and E.A. Irene, Editors. 2005, William Andrew Publishing: Norwich, NY. p. 237-296.
147. Herzinger, C.M., et al., *InP optical constants between 0.75 and 5.0 eV determined by variable-angle spectroscopic ellipsometry.* Journal of Applied Physics, 1995. **77**(4): p. 1715-1724.
148. Caldwell, J.D., et al., *Sub-diffractional volume-confined polaritons in the natural hyperbolic material hexagonal boron nitride.* Nature Communications, 2014. **5**: p. 5221.
149. Ma, W., et al., *In-plane anisotropic and ultra-low-loss polaritons in a natural van der Waals crystal.* Nature, 2018. **562**(7728): p. 557-562.
150. Narimanov, E.E. and A.V. Kildishev, *Naturally hyperbolic.* Nature Photonics, 2015. **9**(4): p. 214-216.
151. Caldwell Joshua, D., et al., *Low-loss, infrared and terahertz nanophotonics using surface phonon polaritons*, in *Nanophotonics*. 2015. p. 44.
152. Basov, D.N., M.M. Fogler, and F.J. García de Abajo, *Polaritons in van der Waals materials.* Science, 2016. **354**(6309).
153. Zhang, M., et al., *Thermal behavior of vibrational phonons and hydroxyls of muscovite in dehydroxylation: In situ high-temperature infrared spectroscopic investigations.* American Mineralogist, 2010. **95**(10): p. 1444-1457.
154. Beran, A., *Crystal Chemistry and Metamorphic Petrology*, in *Infrared spectroscopy of micas. In Micas*, A. Mottana, et al., Editors. 2002, De Gruyter. p. 351-369.
155. Smrčok, L.u., et al., *Combined inelastic neutron scattering and solid-state density functional theory study of dynamics of hydrogen atoms in muscovite 2M$_1$.* 2011. **96**(2-3): p. 301-307.
156. Singha, M. and L. Singh, *Vibrational spectroscopic study of muscovite and biotite layered phyllosilicates.* Indian Journal of Pure & Applied Physics, 2016: p. 116-122.
157. Redhammer, G.n.J., et al., *Spectroscopic and structural properties of synthetic micas on the annite-siderophyllite binary: Synthesis, crystal structure refinement, Mössbauer, and infrared spectroscopy.* American Mineralogist, 2000. **85**(3-4): p. 449-465.

158. Kischkat, J., et al., *Mid-infrared optical properties of thin films of aluminum oxide, titanium dioxide, silicon dioxide, aluminum nitride, and silicon nitride.* Applied Optics, 2012. **51**(28): p. 6789-6798.
159. Bridgman, P.W., *FURTHER NOTE ON BLACK PHOSPHORUS.* Journal of the American Chemical Society, 1916. **38**(3): p. 609-612.
160. Schuster, R., et al., *Anisotropic Particle-Hole Excitations in Black Phosphorus.* Physical Review Letters, 2015. **115**(2): p. 026404.
161. Liu, H., et al., *Semiconducting black phosphorus: synthesis, transport properties and electronic applications.* Chemical Society Reviews, 2015. **44**(9): p. 2732-2743.
162. Abate, Y., et al., *Recent Progress on Stability and Passivation of Black Phosphorus.* Advanced Materials, 2018. **30**(29): p. 1704749.
163. Li, L., et al., *Black phosphorus field-effect transistors.* Nature Nanotechnology, 2014. **9**(5): p. 372-377.
164. Zhang, L., et al., *Structure and Properties of Violet Phosphorus and Its Phosphorene Exfoliation.* Angewandte Chemie International Edition, 2020. **59**(3): p. 1074-1080.
165. Gu, C., et al., *Growth of Quasi-Free-Standing Single-Layer Blue Phosphorus on Tellurium Monolayer Functionalized Au(111).* ACS Nano, 2017. **11**(5): p. 4943-4949.
166. Zhou, Y., et al., *Recent advances in black phosphorus-based photonics, electronics, sensors and energy devices.* Materials Horizons, 2017. **4**(6): p. 997-1019.
167. Padilha, J.E., A. Fazzio, and A.J.R. da Silva, *van der Waals Heterostructure of Phosphorene and Graphene: Tuning the Schottky Barrier and Doping by Electrostatic Gating.* Physical Review Letters, 2015. **114**(6): p. 066803.
168. Liu, H., et al., *Phosphorene: An Unexplored 2D Semiconductor with a High Hole Mobility.* ACS Nano, 2014. **8**(4): p. 4033-4041.
169. Zhang, Z., et al., *Hittorf's phosphorus: the missing link during transformation of red phosphorus to black phosphorus.* CrystEngComm, 2017. **19**(6): p. 905-909.
170. Zhang, L., et al., *High Yield Synthesis of Violet Phosphorus Crystals.* Chemistry of Materials, 2020. **32**(17): p. 7363-7369.
171. Fasol, G., et al., *Lattice dynamics of Hittorf's phosphorus and identification of structural groups and defects in amorphous red phosphorus.* Solid State Communications, 1984. **52**(3): p. 307-310.
172. CORBRJDGE, D.E.C., *INFRA-RED ANALYSIS OF PHOSPHORUS COMPOUNDS.* Journal of Applied Chemistry, 1965: p. 456-465.
173. Lechs, M. and G. Zundel, *Polarizable acid-acid and acid-water hydrogen bonds with M,PO,, H,PO,, H3PQ4, and HH,AsO,l.* Canadian Journal of Chemistry, 1979. **57**: p. 487-493.
174. Wood, J.D., et al., *Effective Passivation of Exfoliated Black Phosphorus Transistors against Ambient Degradation.* Nano Letters, 2014. **14**(12): p. 6964-6970.
175. Wu, S., et al., *Super-Slippery Degraded Black Phosphorus/Silicon Dioxide Interface.* ACS Applied Materials & Interfaces, 2020. **12**(6): p. 7717-7726.
176. Gamage, S., et al., *Nanoscopy of black phosphorus degradation.* Advanced Materials Interfaces, 2016. **3**(12): p. 1600121.
177. Gamage, S., et al., *Reliable passivation of black phosphorus by thin hybrid coating.* Nanotechnology, 2017. **28**(26): p. 265201.

178. Geim, A.K. and I.V. Grigorieva, *Van der Waals heterostructures.* Nature, 2013. **499**(7459): p. 419-425.
179. Novoselov, K.S., et al., *2D materials and van der Waals heterostructures.* Science, 2016. **353**(6298): p. aac9439.
180. Frisenda, R., et al., *Recent progress in the assembly of nanodevices and van der Waals heterostructures by deterministic placement of 2D materials.* Chemical Society Reviews, 2018. **47**(1): p. 53-68.
181. Cao, Y., et al., *Unconventional superconductivity in magic-angle graphene superlattices.* Nature, 2018. **556**(7699): p. 43-50.
182. Withers, F., et al., *Light-emitting diodes by band-structure engineering in van der Waals heterostructures.* Nature Materials, 2015. **14**(3): p. 301-306.
183. Li, M.-Y., et al., *Epitaxial growth of a monolayer WSe_2-MoS_2 lateral p-n junction with an atomically sharp interface.* Science, 2015. **349**(6247): p. 524-528.
184. Huang, C., et al., *Lateral heterojunctions within monolayer $MoSe_2$–WSe_2 semiconductors.* Nature Materials, 2014. **13**(12): p. 1096-1101.
185. Okuno, Y., et al., *Probing the nanoscale light emission properties of a CVD-grown MoS_2 monolayer by tip-enhanced photoluminescence.* Nanoscale, 2018. **10**(29): p. 14055-14059.
186. Bao, W., et al., *Visualizing nanoscale excitonic relaxation properties of disordered edges and grain boundaries in monolayer molybdenum disulfide.* Nature Communications, 2015. **6**(1): p. 7993.
187. Lee, Y., et al., *Characterization of the structural defects in CVD-grown monolayered MoS_2 using near-field photoluminescence imaging.* Nanoscale, 2015. **7**(28): p. 11909-11914.
188. Park, K.-D., et al., *Hybrid tip-enhanced nanospectroscopy and nanoimaging of monolayer WSe_2 with local strain control.* Nano Letters, 2016. **16**(4): p. 2621-2627.
189. Sahoo, P.K., et al., *Probing nano-heterogeneity and aging effects in lateral 2D heterostructures using tip-enhanced photoluminescence.* Optical Materials Express, 2019. **9**(4): p. 1620-1631.
190. Lee, Y., et al., *Near-field spectral mapping of individual exciton complexes of monolayer WS_2 correlated with local defects and charge population.* Nanoscale, 2017. **9**(6): p. 2272-2278.
191. Kim, M.S., et al., *Biexciton Emission from edges and grain boundaries of triangular WS_2 monolayers.* ACS Nano, 2016. **10**(2): p. 2399-2405.
192. Su, W., et al., *Nanoscale mapping of excitonic processes in single-layer MoS_2 using tip-enhanced photoluminescence microscopy.* Nanoscale, 2016. **8**(20): p. 10564-10569.
193. Birmingham, B., et al., *Spatially-Resolved Photoluminescence of Monolayer MoS_2 under Controlled Environment for Ambient Optoelectronic Applications.* ACS Applied Nano Materials, 2018. **1**(11): p. 6226-6235.
194. Carozo, V., et al., *Optical identification of sulfur vacancies: Bound excitons at the edges of monolayer tungsten disulfide.* Science Advances, 2017. **3**(4): p. e1602813.
195. Komsa, H.-P. and A.V. Krasheninnikov, *Two-dimensional transition metal dichalcogenide alloys: stability and electronic properties.* The Journal of Physical Chemistry Letters, 2012. **3**(23): p. 3652-3656.
196. Gong, Y., et al., *Tellurium-assisted low-temperature synthesis of MoS_2 and WS_2 monolayers.* ACS Nano, 2015. **9**(12): p. 11658-11666.

197. Zhang, T., et al., *Universal In situ substitutional doping of transition metal dichalcogenides by liquid-phase precursor-assisted synthesis.* ACS Nano, 2020. **14**(4): p. 4326-4335.
198. Hong, J., et al., *Exploring atomic defects in molybdenum disulphide monolayers.* Nature Communications, 2015. **6**(1): p. 6293.
199. Li, H., et al., *Mechanical exfoliation and characterization of single- and few-layer nanosheets of WSe_2, TaS_2, and $TaSe_2$.* Small, 2013. **9**(11): p. 1974-1981.
200. Kotsakidis, J.C., et al., *Oxidation of monolayer WS_2 in ambient Is a photoinduced process.* Nano Letters, 2019. **19**(8): p. 5205-5215.
201. Ly, T.H., et al., *Observing grain boundaries in CVD-grown monolayer transition metal dichalcogenides.* ACS Nano, 2014. **8**(11): p. 11401-11408.
202. Shioya, H., et al., *Selective oxidation of the surface layer of bilayer WSe_2 by laser heating.* Japanese Journal of Applied Physics, 2019. **58**(12): p. 120903.
203. Tan, C., et al., *Laser-assisted oxidation of multi-layer tungsten diselenide nanosheets.* Applied Physics Letters, 2016. **108**(8): p. 083112.
204. Oh, H.M., et al., *Photochemical reaction in monolayer MoS2 via correlated photoluminescence, raman spectroscopy, and atomic force microscopy.* ACS Nano, 2016. **10**(5): p. 5230-5236.
205. Atkin, P., et al., *Laser exposure induced alteration of WS_2 monolayers in the presence of ambient moisture.* 2D Materials, 2017. **5**(1): p. 015013.
206. Li, Y., et al., *Measurement of the optical dielectric function of monolayer transition-metal dichalcogenides: MoS_2, $MoSe_2$, WS_2, and WSe_2.* Physical Review B, 2014. **90**(20): p. 205422.
207. Bogaert, K., et al., *Diffusion-mediated synthesis of MoS_2/WS_2 lateral heterostructures.* Nano Letters, 2016. **16**(8): p. 5129-5134.
208. Song, W., R. Fei, and L. Yang, *Off-plane polarization ordering in metal chalcogen diphosphates from bulk to monolayer.* Physical Review B, 2017. **96**(23): p. 235420.
209. Liu, Z., et al., *Strain and structure heterogeneity in MoS_2 atomic layers grown by chemical vapour deposition.* Nature Communications, 2014. **5**(1): p. 5246.
210. Azizi, A., et al., *Defect coupling and sub-angstrom structural distortions in $W_{1-x}Mo_xS_2$ monolayers.* Nano Letters, 2017. **17**(5): p. 2802-2808.
211. Conley, H.J., et al., *Bandgap engineering of strained monolayer and bilayer MoS_2.* Nano Letters, 2013. **13**(8): p. 3626-3630.
212. Castellanos-Gomez, A., et al., *Local strain engineering in atomically thin MoS_2.* Nano Letters, 2013. **13**(11): p. 5361-5366.
213. Roldán, R., et al., *Strain engineering in semiconducting two-dimensional crystals.* Journal of Physics: Condensed Matter, 2015. **27**(31): p. 313201.
214. Quereda, J., et al., *Strong modulation of optical properties in black phosphorus through strain-engineered rippling.* Nano Letters, 2016. **16**(5): p. 2931-2937.
215. Shi, H., et al., *Quasiparticle band structures and optical properties of strained monolayer MoS_2 and WS_2.* Physical Review B, 2013. **87**(15): p. 155304.
216. Feng, J., et al., *Strain-engineered artificial atom as a broad-spectrum solar energy funnel.* Nature Photonics, 2012. **6**(12): p. 866-872.
217. Harats, M.G., et al., *Dynamics and efficient conversion of excitons to trions in non-uniformly strained monolayer WS_2.* Nature Photonics, 2020. **14**(5): p. 324-329.

218. Tongay, S., et al., *Defects activated photoluminescence in two-dimensional semiconductors: interplay between bound, charged and free excitons.* Scientific Reports, 2013. **3**(1): p. 2657.
219. Chow, P.K., et al., *Defect-induced photoluminescence in monolayer semiconducting transition metal dichalcogenides.* ACS Nano, 2015. **9**(2): p. 1520-1527.
220. You, Y., et al., *Observation of biexcitons in monolayer WSe_2.* Nature Physics, 2015. **11**(6): p. 477-481.
221. Kretschmer, S., et al., *Formation of defects in two-dimensional MoS_2 in the transmission electron microscope at electron energies below the Knock-on threshold: the role of electronic excitations.* Nano Letters, 2020. **20**(4): p. 2865-2870.
222. Thiruraman, J.P., et al., *Angstrom-size defect creation and ionic transport through pores in single-layer MoS_2.* Nano Letters, 2018. **18**(3): p. 1651-1659.